RL-TR-92-30
Final Technical Report
May 1992

NONUNIFORMITY EFFECTS IN A HYBRID PLATINUM SILICIDE IMAGING DEVICE

University of Arizona

Eustace L. Dereniak, David L. Perry

APPROVED FOR PUBLIC RELEASE; DISTRIBUTION UNLIMITED.

Rome Laboratory
Air Force Systems Command
Griffiss Air Force Base, NY 13441-5700

This report has been reviewed by the Rome Laboratory Public Affairs Office (PA) and is releasable to the National Technical Information Service (NTIS). At NTIS it will be releasable to the general public, including foreign nations.

RL-TR-92-30 has been reviewed and is approved for publication.

APPROVED: 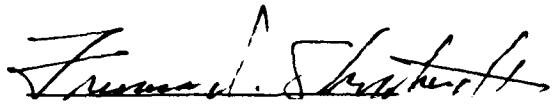

FREEMAN D. SHEPHERD, ST
Senior Scientist, Infrared Sensors & Arrays

FOR THE COMMANDER: 

HAROLD ROTH
Director, Solid State Sciences
Electromagnetics & Reliability Directorate

If your address has changed or if you wish to be removed from the Rome Laboratory mailing list, or if the addressee is no longer employed by your organization, please notify RL(ERED) Hanscom AFB MA 01731-5000. This will assist us in maintaining a current mailing list.

Do not return copies of this report unless contractual obligations or notices on a specific document require that it be returned.

REPORT DOCUMENTATION PAGE

Form Approved
OMB No. 0704-0188

1. AGENCY USE ONLY (Leave Blank)	2. REPORT DATE	3. REPORT TYPE AND DATES COVERED
	May 1992	Final Feb 88 to Jul 91

4. TITLE AND SUBTITLE

NONUNIFORMITY EFFECTS IN A HYBRID PLATINUM SILICIDE IMAGING DEVICE

5. FUNDING NUMBERS

C - F19628-88-K-0009
PE - 61102F
PR - 2305
TA - J1
WU - 54

6. AUTHOR(S)

Eustace L. Dereniak, David L. Perry

7. PERFORMING ORGANIZATION NAME(S) AND ADDRESS(ES)

University of Arizona
Optical Sciences Center
Tucson AZ 85721

8. PERFORMING ORGANIZATION REPORT NUMBER

N/A

9. SPONSORING/MONITORING AGENCY NAME(S) AND ADDRESS(ES)

Rome Laboratory (ERED)
Hanscom AFB MA 01731-5000

10. SPONSORING/MONITORING AGENCY REPORT NUMBER

RL-TR-92-30

11. SUPPLEMENTARY NOTES

Rome Laboratory Project Engineer: Jonathan M. Mooney/ERED/(617)377-2352

12a. DISTRIBUTION/AVAILABILITY STATEMENT

Approved for public release; distribution unlimited.

12b. DISTRIBUTION CODE

13. ABSTRACT (Maximum 200 words)

The objective of this project was twofold. The first objective was to characterize the Hughes Aircraft Company CRC-365 platinum silicide imaging device in a staring infrared sensor system. The CRC-365 is a hybrid 256 x 256 IR focal plane array that operates in the 3-5 micrometer thermal infrared band. A complete sensor and computer interface were built for these tests, using plans provided by the Rome Laboratory at Hanscom AFB MA. Testing of the device revealed largely satisfactory performance, with notable exceptions in the areas of temporal response, temporal noise, and electrical crosstalk.
The second objective of this research was to advance the understanding of how detector nonuniformity effects reduce the performance of sensors of this type. Notable accomplishments in this area included a complete linear analysis of corrected thermal imaging in platinum silicide sensors, a nonlinear analysis of the CRC-365s expected performance, analysis of its actual performance when operated with nonuniformity correction, and the development of a new figure of merit. It was demonstrated that the CRC-365 is capable of maintaining background-noise-limited performance over at least a 40°K target temperature range, when operated with two-point nonuniformity correction.

14. SUBJECT TERMS	15. NUMBER OF PAGES
Infrared Focal Plane Array, Spatial Noise, Nonuniformity, 2D*	232
	16. PRICE CODE

17. SECURITY CLASSIFICATION OF REPORT	18. SECURITY CLASSIFICATION OF THIS PAGE	19. SECURITY CLASSIFICATION OF ABSTRACT	20. LIMITATION OF ABSTRACT
UNCLASSIFIED	UNCLASSIFIED	UNCLASSIFIED	UL

TABLE OF CONTENTS

Page

Page

LIST OF ILLUSTRATIONS

LIST OF TABLES

Table | Page

PREFACE

This final report describes research that was performed at the University of Arizona's Optical Sciences Center under Air Force Contract No. F19628-88-K-0009. This research was conducted between the dates February 5, 1988 through July 31, 1991. Technical guidance was provided by Dr. Freeman D. Shepherd and Dr. Jonathan M. Mooney, both of the Rome Laboratory at Hanscom Air Force Base, Massachusetts. The principal investigator at the University of Arizona was Dr. Eustace L. Dereniak.

The report consists of a doctoral dissertation written by the student investigator on the project, David L. Perry. It contains all relevant findings made during the course of the project.

This research required the construction of a complete infrared sensor and data acquisition system. The setup was constructed with extensive plans provided by Dr. William S. Ewing, also of the Rome Laboratory, and is shown in the photograph below.

This report was submitted to the Rome Laboratory during September 1991.

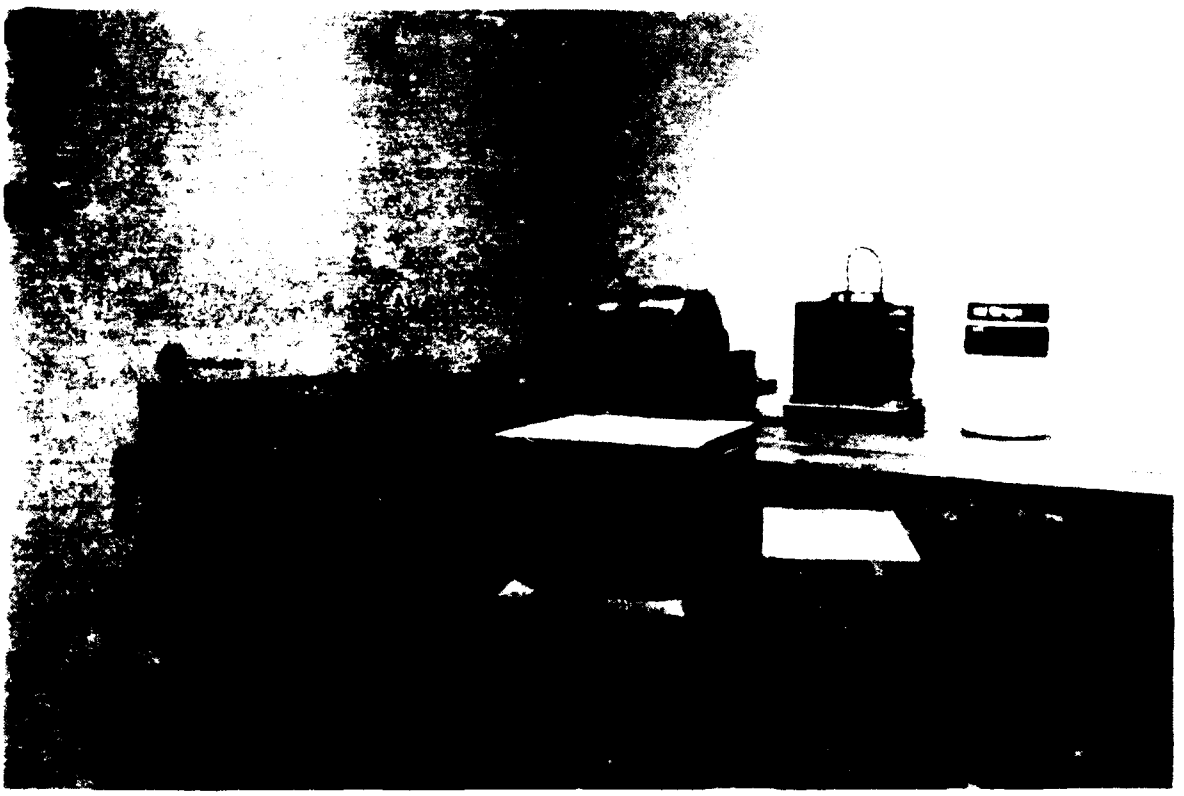

CHAPTER 1

INTRODUCTION

Among the many advances made in optical detection during the last two decades, perhaps none has been more noteworthy than the invention of the focal plane array. These detectors allow optical system designers to directly sense an optical image. The term focal plane array is used to distinguish these devices from earlier scanning detection systems. Rather than scanning an optical scene with a single detector, the focal plane array contains a large number of detectors, arranged in a regular geometric pattern. By placing an in-focus image on the array, the user may obtain an electronic representation of the image. These remarkable devices have allowed system designers to eliminate many of the undesirable properties of scanning detection systems.

Initially, focal plane arrays were developed for operation in the visible region of the electromagnetic spectrum. Devices of this type are now nearing perfection. Their development has been aided by the fact that the detectors and readout electronics can be fabricated in a monolithic silicon structure.

With the experience gained in the visible region, focal plane designers are now working to extend wavelength coverage into the UV and IR portions of the spectrum. In the infrared, progress has been slowed by the need to use specialized materials for the detectors. In many cases, these materials are not compatible with standard silicon fabrication techniques. This has forced designers to develop hybridized structures. In this approach, the detector array and readout electronics are fabricated and tested separately. Following testing, special techniques are used to attach the two pieces. One notable exception to this is the IRCCD, which makes use of integrated Schottky photodiodes.

In both the monolithic and the hybridized formats, IR devices have been plagued by a number of practical problems. One particularly troublesome aspect of these devices is response nonuniformity. To obtain a good representation of an image focussed on a focal plane array, it is essential that all the detectors in the array behave identically. If response nonuniformity is present, each detector and its associated electronics produce slightly different outputs when exposed to uniform illumination. These nonuniformity effects are important because they are indistinguishable from details present in the optical scene.

When viewing the output produced by a focal plane array with response nonuniformity, one sees an embedded pattern of lines or smudges obscuring the desired image. Figure 1.1 illustrates this effect. The image of a four-bar test source, set to a differential temperature of 3°C, is almost lost in the embedded pattern noise. The test source is not visible when set to a differential temperature below about 1°C.

The objective of this investigation was to explore the impact of nonuniformity on thermal imaging. This research was performed under USAF Contract No. F19628-88-K-0009. Attention was generally restricted to a platinum silicide hybrid focal plane array built to operate in the 3-5 μm middle-wave infrared (MWIR) band. The device, called the Hughes Aircraft CRC-365, was provided by the Rome Laboratory at Hanscom Air Force Base, Mass., along with the necessary funds to build a complete infrared camera and test system. The CRC-365 features an array of 256 x 256 platinum silicide detectors, arranged on 30-μm centers. The camera system revealed many interesting properties of the CRC-365, and allowed laboratory testing of various nonuniformity theories.

Chapter 2 develops a complete linear theory for nonuniformity in platinum silicide focal plane arrays, applicable to either IRCCD or hybridized devices. Following this general discussion, higher-order effects specific to the CRC-365 are investigated. This chapter forms the basis for interpreting the results observed in laboratory testing.

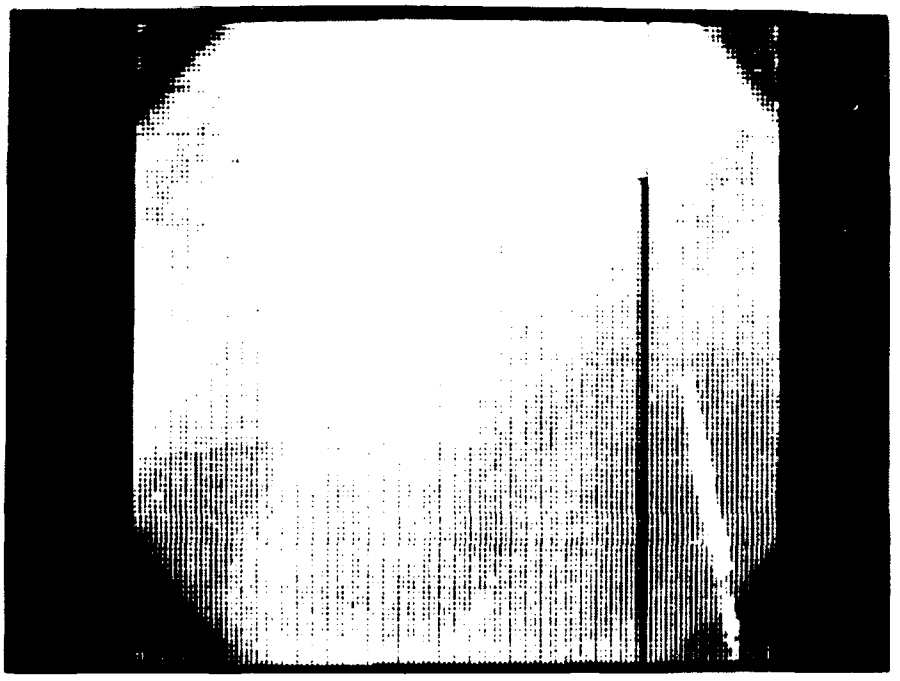

Figure 1.1 Infrared camera output with response nonuniformity and differential bar temperature of 3°C

Chapter 3 presents the results of actual laboratory testing. The camera system was used to perform a number of standardized detector tests. In addition to these tests, extensive tests of device nonuniformity were conducted. Optimal operating conditions for the CRC-365 were established.

Chapter 4 analyzes the results of nonuniformity testing. Upper bounds are established for the relative amounts of different types of nonuniformity present in the tested device. The CRC-365 is found to suffer from a number of nonuniformity problems, but performs quite well overall.

In Chapter 5, conventional detector figures of merit are discussed. These measures of detector performance do not normally include nonuniformity effects. Several modifications to these conventional figures of merit are suggested, illustrating the drastic reductions in system performance which result when nonuniformity effects are included.

Finally, in Chapter 6 the results of this research are summarized. Several specific recommendations are made and expected future developments are discussed.

CHAPTER 2

MATHEMATICAL ANALYSIS OF NONUNIFORMITY

Response nonuniformity (hereafter referred to as nonuniformity) in focal plane arrays may be analyzed using a theory developed by Mooney (Mooney, 1989a). Mooney's analysis is quite general, in that no particular type of detector is assumed. In the material to follow, his method will be used to predict the performance of a camera system using a platinum silicide (hereafter referred to as PtSi) focal plane array. This analysis assumes that the detector response is not modified by the signal integration process. Furthermore, it is assumed that the electronic readout mechanism associated with each detector is linear. In this investigation, this approach shall be referred to as the linear theory of nonuniformity. These results are applicable to both IRCCD and hybrid PtSi imaging devices.

The linear theory of nonuniformity presented in this chapter is adequate for all but the most demanding predictions of PtSi device performance. In practice, it is known that the assumptions of the linear theory are not strictly valid. In PtSi detectors, the quantum efficiency is a weak function of detector bias. In present-day imaging devices, this bias voltage decreases as a function of collected photocharge. Additionally, in hybrid devices such as the CRC-365, the voltage transfer function from the detector to the output is nonlinear. These effects make small but measurable contributions to the thermal response. These nonlinear effects are taken into account for the CRC-365 later in this chapter.

Given that present-day PtSi imaging devices require external correction for nonuniformity, two popular methods for correction are discussed. An additive offset correction is the simplest type of nonuniformity correction, and shall be referred to in this investigation as the one-point method. The next most commonly used correction scheme

involves both offset and slope corrections to the output of the imaging device. This shall be referred to as the two-point method. The effectiveness of both strategies is examined in this chapter. It is shown that the nonlinear effects described earlier lessen the effectiveness of these correction methods.

Linear Theory of Nonuniformity

The linear theory of nonuniformity is applicable to all PtSi imaging devices. Before beginning a detailed discussion of nonuniformity, a brief description of these devices will be given.

Periodically, the PtSi photodiodes in the detector array are reset to a known potential. Under the influence of incident radiation, the potential across each photodiode decreases, in proportion to the signal flux falling on it. These detectors operate in a charge integrating mode. Following this period of signal integration, the photodiode is read out. Either photocharge or detector voltage may be sensed.

In the case of the IRCCD, photocharge is measured at the output by means of a charge-to-voltage type of amplifier. Each charge packet accumulated in the detector array is systematically moved to the input of this amplifier by means of charge-coupled shift registers. The magnitude of the output voltage is a measure of the average scene radiance sensed by the particular photodiode being read out. An example of this type of device is the David Sarnoff Laboratories 160 x 244 IRCCD (Kosonocky, 1990).

In the case of hybrid imaging devices, such as the CRC-365, the readout process utilizes an amplifier-per-detector approach. In this case, the voltage across each detector is buffered by its own source-follower amplifier. The output of each such amplifier is sequentially accessed by a switch matrix, or multiplexer. When selected, the output of the addressed amplifier is connected to the outside world by another, low output impedance source follower. As in the case of the IRCCD, it is the magnitude of the output voltage that

is observed by the user. This is referred to by Hughes Aircraft as the direct readout method, or DRO for short. Aguilera (Aguilera, 1987) and Gates (Gates, 1988) describe this type of readout process and the Hughes CRC-304 (predecessor of the CRC-365) and CRC-365 devices in greater detail.

A schematic representation of the CRC-365 is shown in Figure 2.1. Assuming linearity, the voltage across the detector appears at the output node, with only an offset and slope adjustment. A voltage versus time plot for the detector is shown in Figure 2.2.

Figure 2.1 represents only one of the many detectors making up the entire focal plane array. It is the differences between the individual detectors and their associated output paths that are of interest in this analysis. These differences cause unwanted nonuniformity effects. As an example, consider the case in which a particular photodiode has a larger active area than its neighbors. As a consequence, it produces an abnormally high indication of the scene radiance.

The PtSi detector array uses individual photodiodes whose operation is illustrated in Figures 2.3 and 2.4. The figures show how photogenerated holes are emitted into the silicon substrate, leaving a net negative charge on the platinum silicide. This accumulation of charge is responsible for the voltage versus time waveform of Figure 2.2. These photodiodes respond to thermal radiation whose wavelength is roughly in the 1 to 5.5 μm range.

The response is optimized by the addition of an optical cavity, represented in Figure 2.5 by the dielectric and aluminum layers behind the PtSi layer. This type of structure operates on the principle of constructive interference, and is typically built to maximize response at 4.0 μm. These principles are discussed in detail in a text by Macleod (Macleod, 1986).

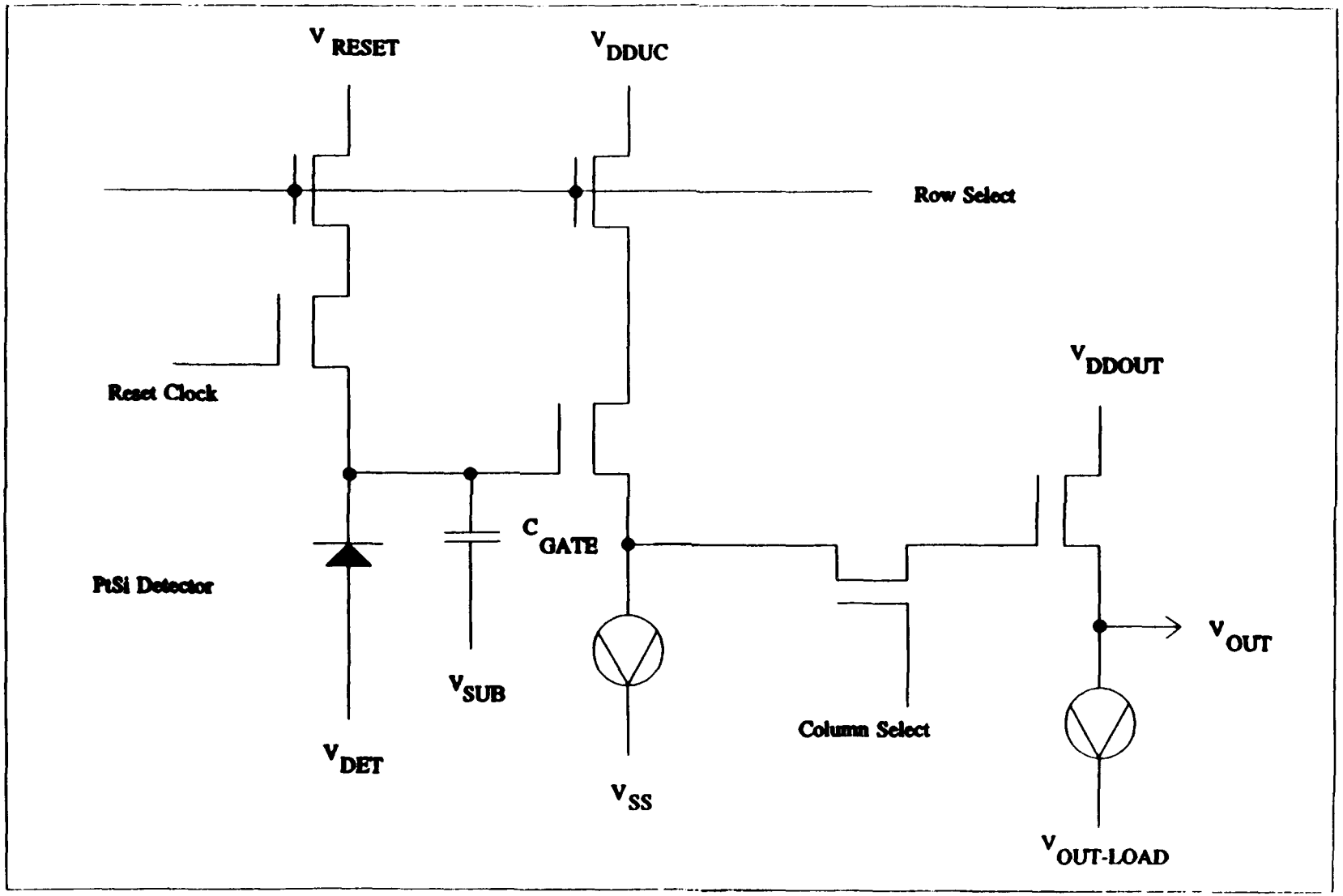

Figure 2.1 Simplified schematic for the CRC-365 Imaging device

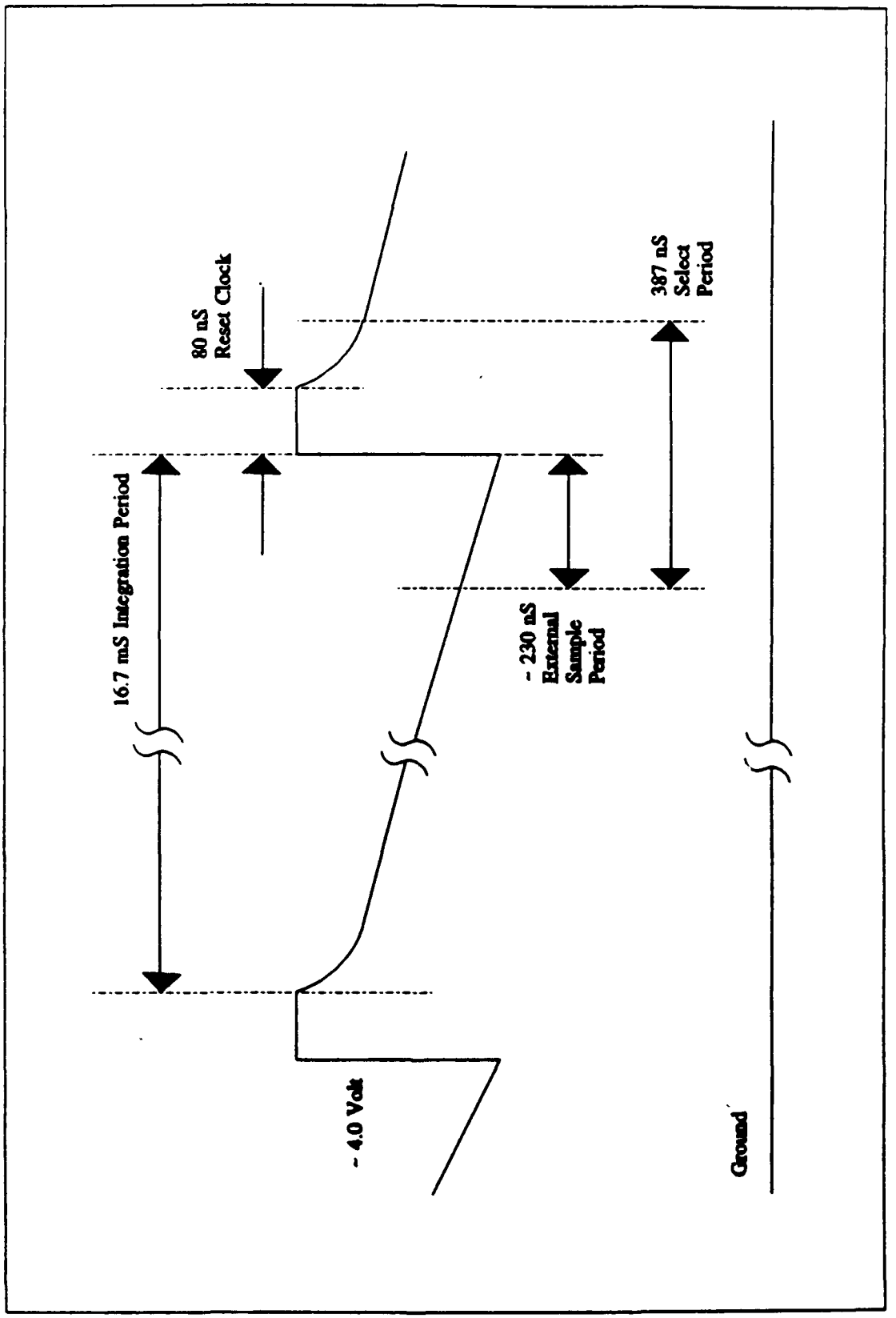

Figure 2.2 Voltage versus time across PtSi detector

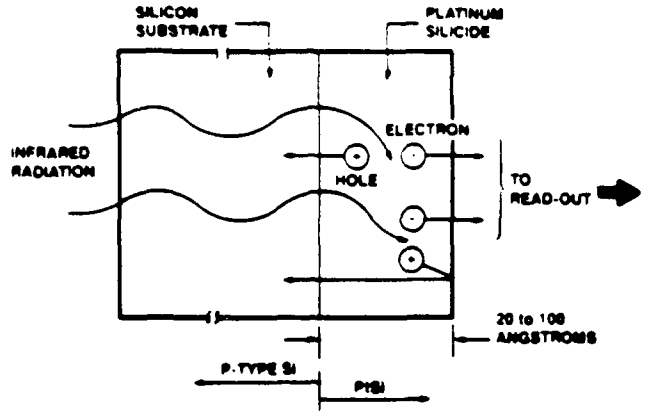

Figure 2.3 PtSi detection process

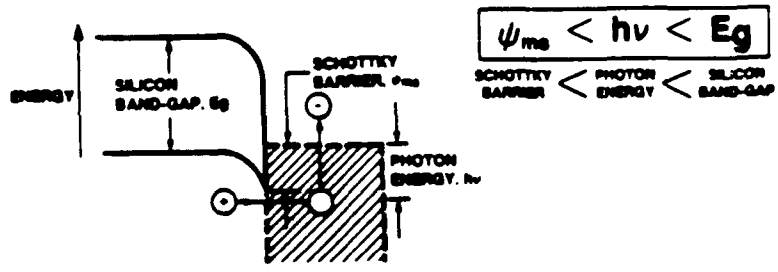

Figure 2.4 PtSi detector band diagram

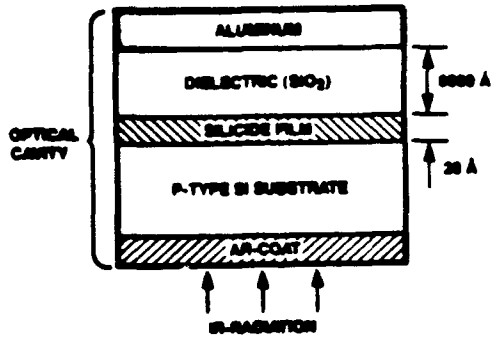

Figure 2.5 PtSi detector with optical cavity

The physics of thin PtSi films have been investigated by a number of researchers. Vickers (Vickers, 1971) and Cohen (Cohen, 1968) were among the first to quantify their performance in the context of infrared photodetection.

The exact range of wavelengths over which these backside-illuminated detectors respond is given by the following relationship.

$$\psi_{ms} < \frac{hc}{\lambda q} < E_g \tag{2.1}$$

ψ_{ms} is called the Schottky barrier height, expressed in electron volts (eV). E_g is the energy gap of the silicon substrate,whose value is 1.1 eV. The wavelength of the incoming radiation is represented by λ, h is Planck's constant, c is the speed of light, and q is the electron charge.

The quantum efficiency as a function of wavelength for these detectors is expressed as follows.

$$\eta(\lambda) = \frac{C_1 \lambda}{1.24}\left[\frac{1.24}{\lambda} - \psi_{ms}\right]^2 \tag{2.2}$$

C_1 is called the Schottky quantum yield, expressed in $(eV)^{-1}$. Note that in this expression, λ is in μm. The constant 1.24 is proportional to hc/q, which appears in Eq. (2.1). C_1 is actually a function of wavelength, but will be treated as a constant for the 3-5 μm waveband of this investigation.

As an example of these ideas, consider a PtSi photodiode whose barrier height and quantum yield are 0.22 eV and 0.20 eV^{-1} respectively. Equations (2.1) and (2.2) predict a cutoff wavelength of 5.6 μm and a quantum efficiency of 1 percent at 3.5 μm.

Uncorrected Thermal Response

In this section, an expression for the response of a PtSi camera to thermal radiation will be derived. This expression will permit calculation of the uncorrected nonuniformity, and will be used in subsequent sections to explore the improvements offered by nonuniformity correction. Throughout these derivations, the subscript notation (i,j) will be used to refer to the specific picture element, or pixel, under consideration.

For convenience, the flux incident on the detectors will be calculated in photon units. The effects of atmospheric absorption will be ignored. Thermal objects imaged by the optical system will be treated as perfect blackbody radiators unless otherwise noted. Making these simplifications, the photon flux $\Phi_{ij}(T_{ij})$ collected by the $(i,j)^{th}$ detector is

$$\Phi_{ij}(T_{ij}) = \left[\int_{\lambda_1}^{\lambda_2} L(\lambda, T_{ij})\, d\lambda\right] A_{ij}\, \Omega\, \tau_{eff} \tag{2.3}$$

$\Phi_{ij}(T_{ij})$ is expressed in photons per second. $L(\lambda, T_{ij})$ is the spectral radiance of the $(i,j)^{th}$ object space cell, expressed in photons per second-steradian-μm-cm^2. Its temperature is T_{ij}, given in degrees Kelvin. A_{ij} is the active area of the detector in cm^2, Ω is the projected solid angle subtended by the exit pupil, and τ_{eff} is the effective transmittance of the optical system. τ_{eff} is considered here to be independent of image field height, and includes the transmission losses for all elements of the optical system. Note that the projected solid angle Ω is also considered to be independent of field height and it, too, carries no (ij) subscript. A more general analysis would treat both τ_{eff} and Ω as functions of image plane position. λ_1 and λ_2 are the cutoff wavelengths defined by the optical system bandpass filter. $L(\lambda, T_{ij})$ is given by Planck's law for photons, shown in the following equation.

$$L(\lambda, T_{ij}) = \frac{2c}{\lambda^4 \left[e^{c_2/\lambda T_{ij}} - 1\right]} \tag{2.4}$$

The constant c is the speed of light, and c_2 is referred to as the second radiation constant. Its value is hc/k, where k is Boltzman's constant. The solid angle subtended by the exit pupil of the optical system may be expressed in terms of its F/number (F/#).

$$\Omega = \frac{\pi}{4(F/\#)^2 + 1} \tag{2.5}$$

Now that the flux is known, the detector response may be calculated. As shown in Eq. (2.2), the quantum efficiency of these detectors has a strong wavelength dependence. For this reason, we cannot simply scale the flux by a constant, as is done for some detectors. To calculate the detector photocurrent, the flux expression must be modified, integrating the product of the radiance and the quantum efficiency. As mentioned earlier, the PtSi detectors are operated in a charge integrating mode. To convert from photocurrent to charge, one need only multiply by the integration time, t_{int}. The result of these steps is shown in the following expression for N_{ij}, the number of photogenerated carriers collected at detector (i,j).

$$N_{ij}(T_{ij}) = \left[\int_{\lambda_1}^{\lambda_2} L(\lambda, T_{ij})\, \eta_{ij}(\lambda)\, d\lambda\right] A_{ij}\, \Omega\, \tau_{eff}\, t_{int} \tag{2.6}$$

As an example of the results obtained thus far, consider the following nominal F/2 optical system, imaging a room-temperature scene. Let the optical bandpass extend from 3.5 to 5.5 μm with an effective transmittance of 0.75. The integration time is 1/60 second

and the active area is $(28\ \mu m)^2$. The quantum efficiency is defined by a barrier height of 0.22 eV and a quantum yield of 0.20 eV^{-1}. These values are summarized in Table 2.1, and shall be used for a number of subsequent example calculations.

Using these nominal camera parameters, Eq. (2.6) yields the photoresponse shown in Table 2.2. Note that output signals will be reported as time-averaged values, in units of electrons, unless otherwise noted. For a source temperature of 26°C, note that the average photoresponse is 195,756 electrons. The signal contrast shown in Table 2.2 is about 7500 electrons per degree Kelvin. This is the temperature derivative of the output signal. In the case of a DRO readout with a 0.10 pF sense-node capacitance, the equivalent signal contrast is 12 millivolts per degree Kelvin.

In practice, photodetectors suffer from dark current. This unwanted reverse current flows during the signal integration period, and effectively adds a DC bias to the output signal. One may include dark current in Eq. (2.6) by adding the term D_{ij}, the average number of dark current carriers collected per integration period. A response coefficient R_{ij} is introduced to simplify the expression.

$$N_{ij}(T_{ij}) = R_{ij} \int_{\lambda_1}^{\lambda_2} L(\lambda, T_{ij})\, \eta_{ij}(\lambda)\, d\lambda + D_{ij} \tag{2.7}$$

$$R_{ij} = \left[\frac{\pi}{4(F/\#)^2 + 1}\right] \tau_{eff}\, t_{int}\, A_{ij} \tag{2.8}$$

By examination of Eq. (2.7), it is clear than unless R_{ij}, D_{ij}, and η_{ij} are the same for each detector in the array, nonuniformity effects will be present. Consider the case in which a particular detector differs from its neighbors. Table 2.3 shows the change in output produced by typical variations seen in real detectors. The temperature equivalent

Table 2.1

Nominal PtSi Camera Parameters

F/2 cold stop

3.5 μm - 5.5 μm bandpass

75% effective optical transmittance

1/60 second integration period

$(28\ \mu m)^2$ detector active area

Schottky barrier height = .22 eV

Schottky quantum yield = 0.20 eV^{-1}

Table 2.2

PtSi Camera Response

Background Temperature °K	°C	Output Signal, e^-
298.15	25.0	188,520
299.15	26.0	195,756
300.15	27.0	203,223

Table 2.3

26°C Response Variations

Conditions	Output Signal, in e^-	Change in Signal, e^-	Temp. Equiv. of Change, Deg.
Nominal	215,756	N/A	N/A
+4% D_{ij}	216,556	+800	0.11
+2% R_{ij}	219,671	+3915	0.53
-0.25% ψ_{ms-ij}	219,954	+4198	0.57

values shown on the far right were obtained by dividing the change in output by the signal contrast discussed earlier. Recall that the signal contrast is about 7500 electrons per degree Kelvin. All nominal camera parameters were the same as in the previous example. Dark charge was taken to be 20,000 electrons. The reasons for choosing this value will be discussed in a later section.

One way to evaluate the importance of these effects is to compare their magnitude to the temporal noise. To this point in the discussion, time-averaged values have been used. Consider now the frame-to-frame fluctuations observed for a single detector. Due to the uncertainty associated with the emission and detection processes, one will see substantial temporal fluctuations in the output signal (Frieden, 1983). For blackbody radiation whose wavelength is less than 30 μm, it can be shown that the statistical fluctuations on the output signal obey the Poisson probability law (Grum and Becherer, 1979). For the Poisson distribution, the variance is equal to the mean signal level. Applying this rule to an average 26°C output of 215,756 electrons, an rms fluctuation of about 465 electrons would be expected. Its temperature equivalent is 465/7500 or 0.06°C. This measure of performance has been discussed by many authors, and is called the noise-equivalent temperature difference, or NETD (Lloyd, 1975). In this example the R_{ij} and ψ_{ms-ij} output changes are almost ten times greater than the NETD. Nonuniformity effects of this magnitude would seriously degrade thermal imaging performance.

To further describe these effects, a statistical approach will be taken, whereby modifying Eq. (2.7) will explicitly show the impact of various nonuniformity terms. In this approach, it shall now be assumed that the thermal source is perfectly uniform. The resulting irradiance at the detector array is the same for all detectors, independent of position. When this is true, any spatial variation in the output will be strictly attributable to imaging device nonuniformity.

Under uniform illumination, since each object-space cell is at the same temperature, all the T_{ij} values are identical. For this reason, the (ij) subscript associated with blackbody temperature will be replaced with a single subscript, denoting the temperature of the uniform source. When viewing a source of temperature T_s, the average detector output is as shown.

$$\langle N_{ij}(T_s)\rangle = \langle R_{ij}\rangle \int_{\lambda_1}^{\lambda_2} \langle \eta_{ij}(\lambda)\rangle \, L(\lambda, T_s)\, d\lambda + \langle D_{ij}\rangle \tag{2.9}$$

The bracket notation is used for spatial averages, taken for all detectors in the focal plane array. Equation (2.9) was obtained from Eq. (2.7) by applying the definition for expected value, and assuming statistical independence between R_{ij} and η_{ij}.

The properties of a given detector shall now be defined as the sum of an array-wide average value and the deviation from this average. This step is shown in Eqs. (2.10), (2.11), and (2.12).

$$D_{ij} = \langle D_{ij}\rangle + d_{ij} \tag{2.10}$$

$$R_{ij} = \langle R_{ij}\rangle + r_{ij} \tag{2.11}$$

$$\eta_{ij}(\lambda) = \langle \eta_{ij}(\lambda)\rangle + \kappa_{ij}(\lambda) \tag{2.12}$$

The incremental terms d_{ij}, r_{ij}, and $\kappa_{ij}(\lambda)$ are often referred to as offset, slope, and spectral errors, respectively.

In Eq. (2.12), the spatial average of the quantum efficiency is a function of wavelength. This is evaluated by averaging the quantum efficiency spatially, on a wavelength-by-wavelength basis. Note that the deviation terms d_{ij}, r_{ij}, and $\kappa_{ij}(\lambda)$ are zero-mean random variables. Substituting these expressions into Eq. (2.7), dropping an unimportant term, and making use of the $\langle N_{ij}(T_s) \rangle$ expression of Eq. (2.9), one obtains

$$N_{ij}(T_s) = \langle N_{ij}(T_s) \rangle + d_{ij} + \frac{r_{ij}}{\langle R_{ij} \rangle} [\langle N_{ij}(T_s) \rangle - \langle D_{ij} \rangle] + \langle R_{ij} \rangle \int_{\lambda_1}^{\lambda_2} \kappa_{ij}(\lambda) L(\lambda, T_s)\, d\lambda \quad . \tag{2.13}$$

Equation (2.13) shows how the output of a specific detector differs from the array-wide average output, in terms of its deviations d_{ij}, r_{ij}, and κ_{ij}.

Equations (2.6) through (2.13) constitute a general method of nonuniformity analysis. This method appears in the article by Mooney (Mooney, 1989a).

Note that there would be no nonuniformity if each of these terms were zero. This condition is stated mathematically as

$$N_{ij}(T_s) = \langle N_{ij}(T_s) \rangle \quad \text{iff.} \quad d_{ij} = r_{ij} = \kappa_{ij}(\lambda) = 0 \tag{2.14}$$

Detector-to-detector differences exist because of spatial variations in the raw materials and manufacturing processes used to make them. The properties of the electronic readout have not been mentioned explicitly in this discussion of uncorrected nonuniformity. Recall that the output of each detector is brought out of the imaging device with at most an offset and slope adjustment. In the linear theory of nonuniformity, pixel-to-pixel variations in the electronics are indistinguishable from detector dark current and response coefficient

variations. For this reason, the terms detector output, device output, and camera output will continue to be used interchangeably, unless otherwise noted.

Equation (2.13) may be used to predict the spatial noise present in the camera output. This assumes that the spread in various detector parameters is known. Applying the definition of variance, and assuming statistical independence between D_{ij}, R_{ij}, and $\eta_{ij}(\lambda)$, the following expression is obtained.

$$\sigma_N^2 = \sigma_D^2 + \frac{\sigma_R^2}{\langle R_{ij} \rangle^2} [\langle N_{ij}(T_s) \rangle - \langle D_{ij} \rangle]^2 + \langle R_{ij} \rangle^2 \left\langle \left| \int_{\lambda_1}^{\lambda_2} \kappa_{ij}(\lambda) L(\lambda, T_s) \, d\lambda \right|^2 \right\rangle \tag{2.15}$$

The symbols σ_N^2, σ_D^2, and σ_R^2 represent the variance on the output, dark charge, and response coefficient, respectively. In high-quality photodiodes, the dark charge may be strongly correlated with the detector active area and quantum efficiency. In this case, the assumptions of statistical independence are violated, and Eq. (2.15) will yield slightly optimistic predictions for the total spatial noise.

To evaluate Eq. (2.15) for a PtSi focal plane array, an expression for $\kappa_{ij}(\lambda)$ must be obtained. Recall that the quantum efficiency for PtSi photodiodes is shown in Eq. (2.2). The Schottky quantum yield, $C_{1\text{-}ij}$, and Schottky barrier height, $\psi_{ms\text{-}ij}$, specify the performance of the ij^{th} detector. Since $C_{1\text{-}ij}$ is considered to be a constant in this analysis, it may be paired with A_{ij} in the system response coefficient R_{ij}. When this is done, a simplified expression for the quantum efficiency is obtained. The new expressions are as follows.

$$R'_{ij} = R_{ij}\, C_{1\text{-}ij} = \left[\frac{\pi}{4(F/\#)^2 + 1}\right] \tau_{eff}\, t_{int}\, A_{ij}\, C_{1\text{-}ij} \tag{2.16}$$

$$\eta'_{ij}(\lambda) = \frac{\eta_{ij}(\lambda)}{C_{1\text{-}ij}} = \frac{\lambda}{1.24}\left(\frac{1.24}{\lambda} - \psi_{ms\text{-}ij}\right)^2 \tag{2.17}$$

Note that if $C_{1\text{-}ij}$ and $\psi_{ms\text{-}ij}$ are assumed to be statistically independent, the results shown in Eqs. (2.13) and (2.15) are unchanged.

An expression for $\kappa_{ij}(\lambda)$ may be obtained by rearranging Eq. (2.12).

$$\kappa_{ij}(\lambda) = \eta_{ij}(\lambda) - \langle \eta_{ij}(\lambda) \rangle \tag{2.18}$$

The new definition for quantum efficiency, shown in Eq. (2.17), may be substituted into Eq. (2.18).

$$\kappa_{ij}(\lambda) = \frac{\lambda}{1.24}\left(\frac{1.24}{\lambda} - \psi_{ms\text{-}ij}\right)^2 - \left\langle \frac{\lambda}{1.24}\left(\frac{1.24}{\lambda} - \psi_{ms\text{-}ij}\right)^2 \right\rangle \tag{2.19}$$

By introducing a new variable, δ_{ij}, Eq. (2.19) can be expressed as follows.

$$\kappa_{ij}(\lambda) = -2\,\delta_{ij} + \frac{\lambda}{1.24}\left(2\,\delta_{ij}\langle \psi_{ms\text{-}ij} \rangle + \delta_{ij}^2 - \sigma_p^2\right) \tag{2.20}$$

$$\psi_{ms\text{-}ij} = \langle \psi_{ms\text{-}ij} \rangle + \delta_{ij} \tag{2.21}$$

The term δ_{ij} represents the incremental deviation in barrier height of the ij^{th} photodiode. The term σ_p^2 is the variance on Schottky barrier height. For PtSi photodiodes whose

nominal barrier height is around 0.2 eV, and whose rms spread in barrier height is less than 2 percent or so, Eq. (2.20) simplifies to

$$\kappa_{ij} \approx -2\,\delta_{ij}\left(1 - \frac{\lambda}{1.24}\langle \psi_{ms\text{-}ij}\rangle\right) \quad . \tag{2.22}$$

This is the desired result. When this expression is substituted into Eq. (2.13) or (2.15), exact performance predictions for a PtSi imaging device can be made. Substituting this result into Eq. (2.15), the following expression is obtained.

$$\sigma_N^2 = \sigma_D^2 + \frac{\sigma_{R'}^2}{\langle R'_{ij}\rangle^2}\left[\langle N_{ij}(T_s)\rangle - \langle D_{ij}\rangle\right]^2 + 4\,\sigma_P^2\langle R'_{ij}\rangle^2\left\{\int_{\lambda_1}^{\lambda_2}\left(1 - \frac{\lambda\langle \psi_{ms\text{-}ij}\rangle}{1.24}\right)L(\lambda, T_s)\,d\lambda\right\}^2 \tag{2.23}$$

Some representative results of this step are shown in Figures 2.6 through 2.9. The rms spatial noise versus background temperature is plotted, using the nominal camera parameters of earlier examples. The spatial noise is reported in both electron and equivalent source temperature difference units. The temporal noise is provided for reference.

Figure 2.6 shows only the first term of Eq. (2.23). The rms nonuniformity in D_{ij} is 4 percent. Figures 2.7 and 2.8 show the second and third terms of Eq. (2.23). The rms nonuniformity in R_{ij} and $\psi_{ms\text{-}ij}$ is 2 percent and 0.25 percent, respectively. Note that in Figures 2.6 through 2.8, the spatial noise may be scaled linearly for any level of nonuniformity.

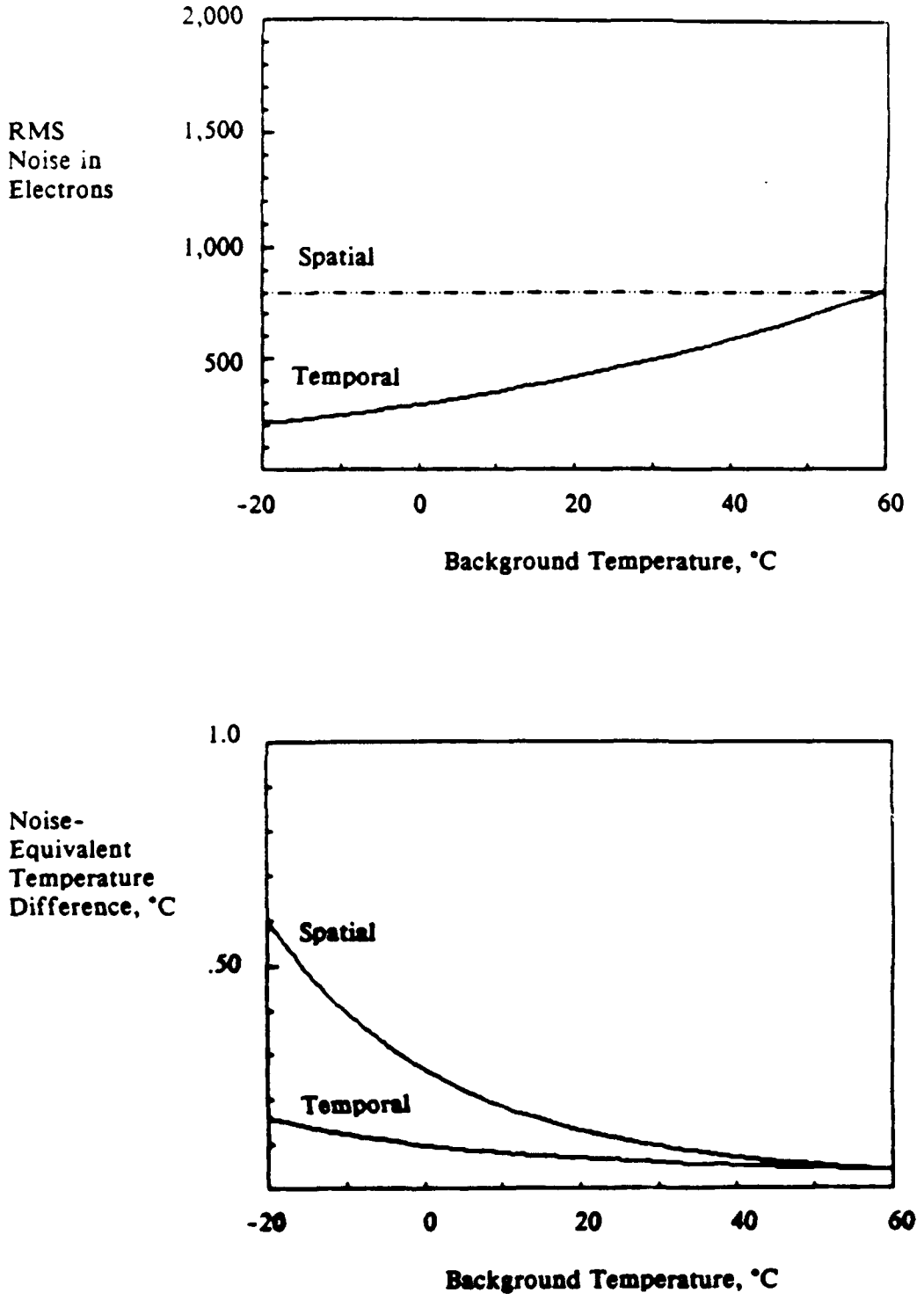

Figure 2.6 Spatial noise versus background temperature for 4 percent dark charge nonuniformity

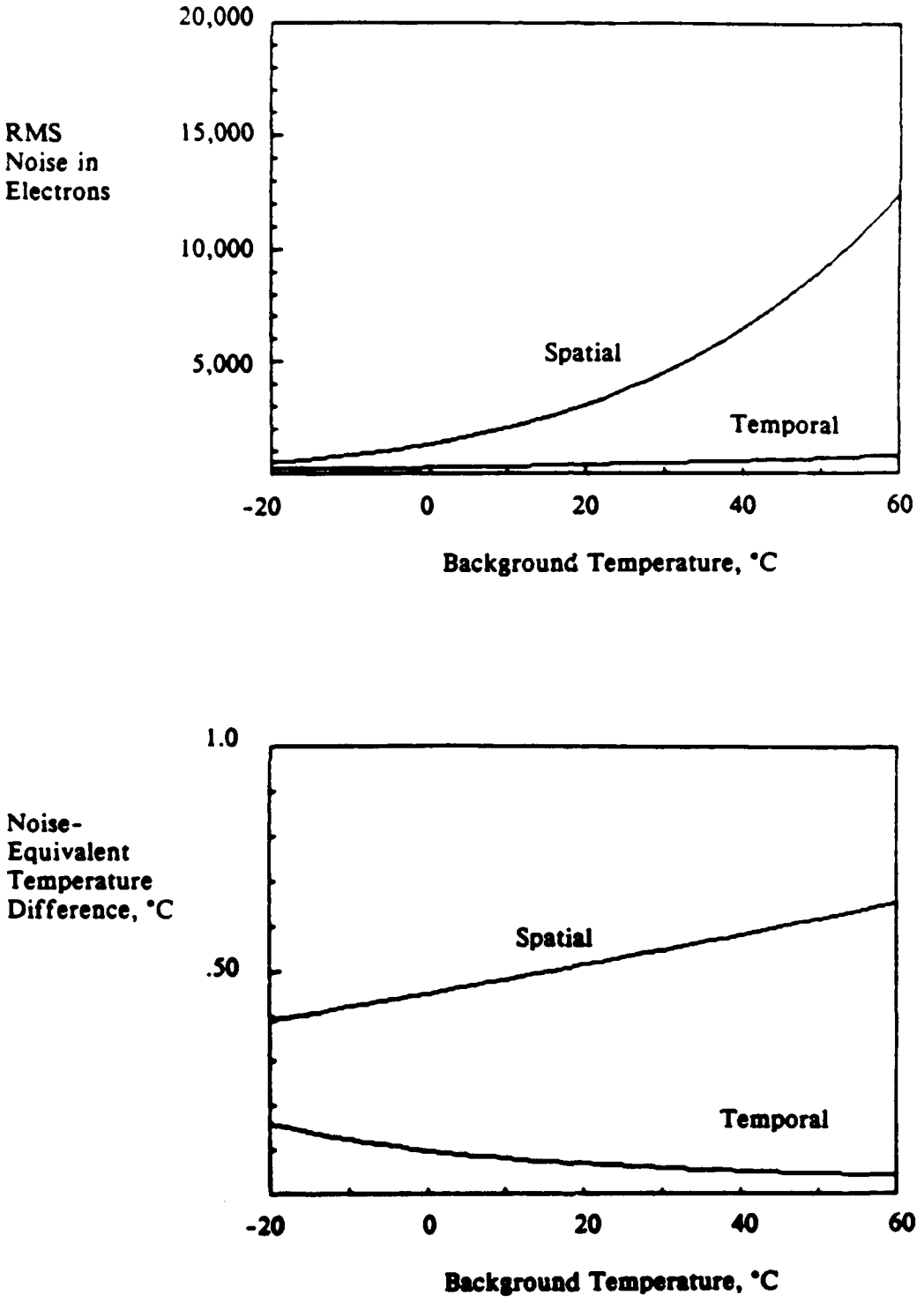

Figure 2.7 Spatial noise versus background temperature for 2 percent response coefficient nonuniformity

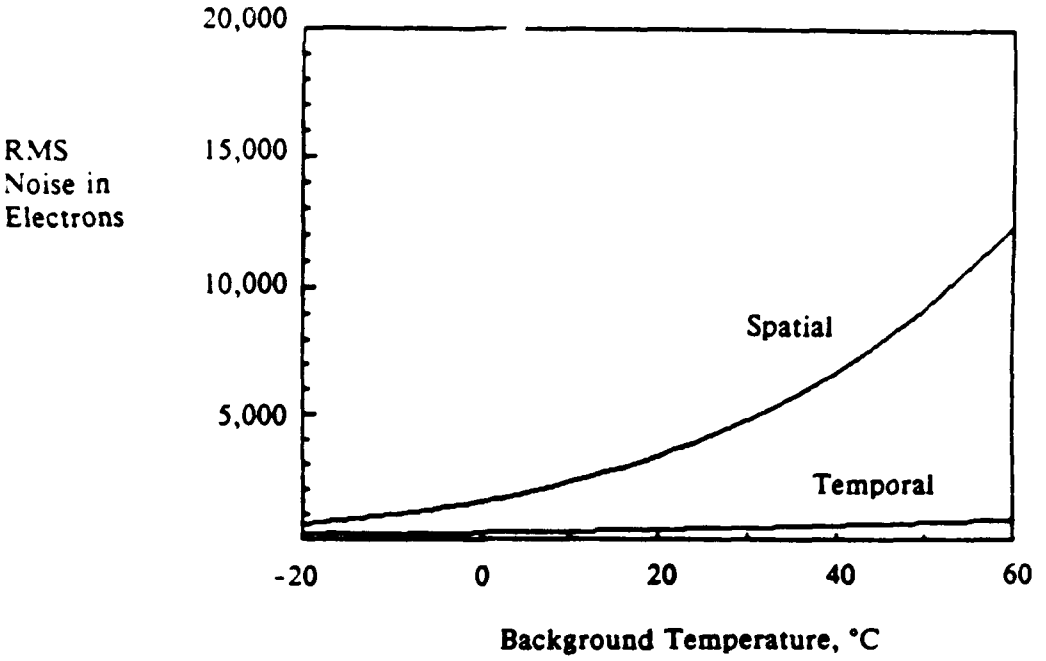

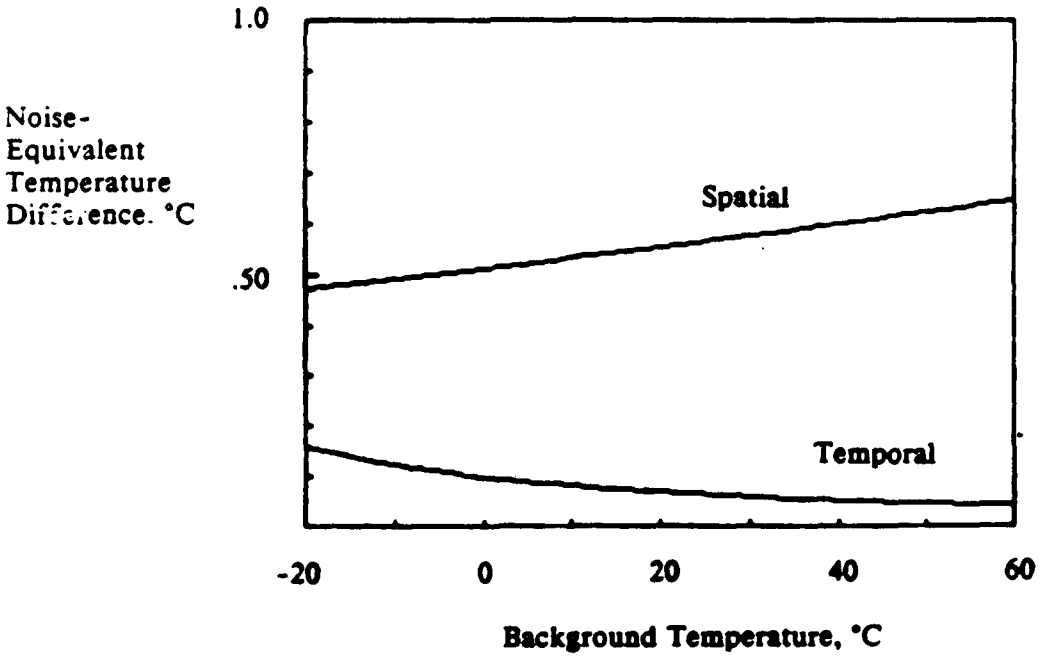

Figure 2.8 Spatial noise versus background temperature for 0.25 percent barrier height nonuniformity

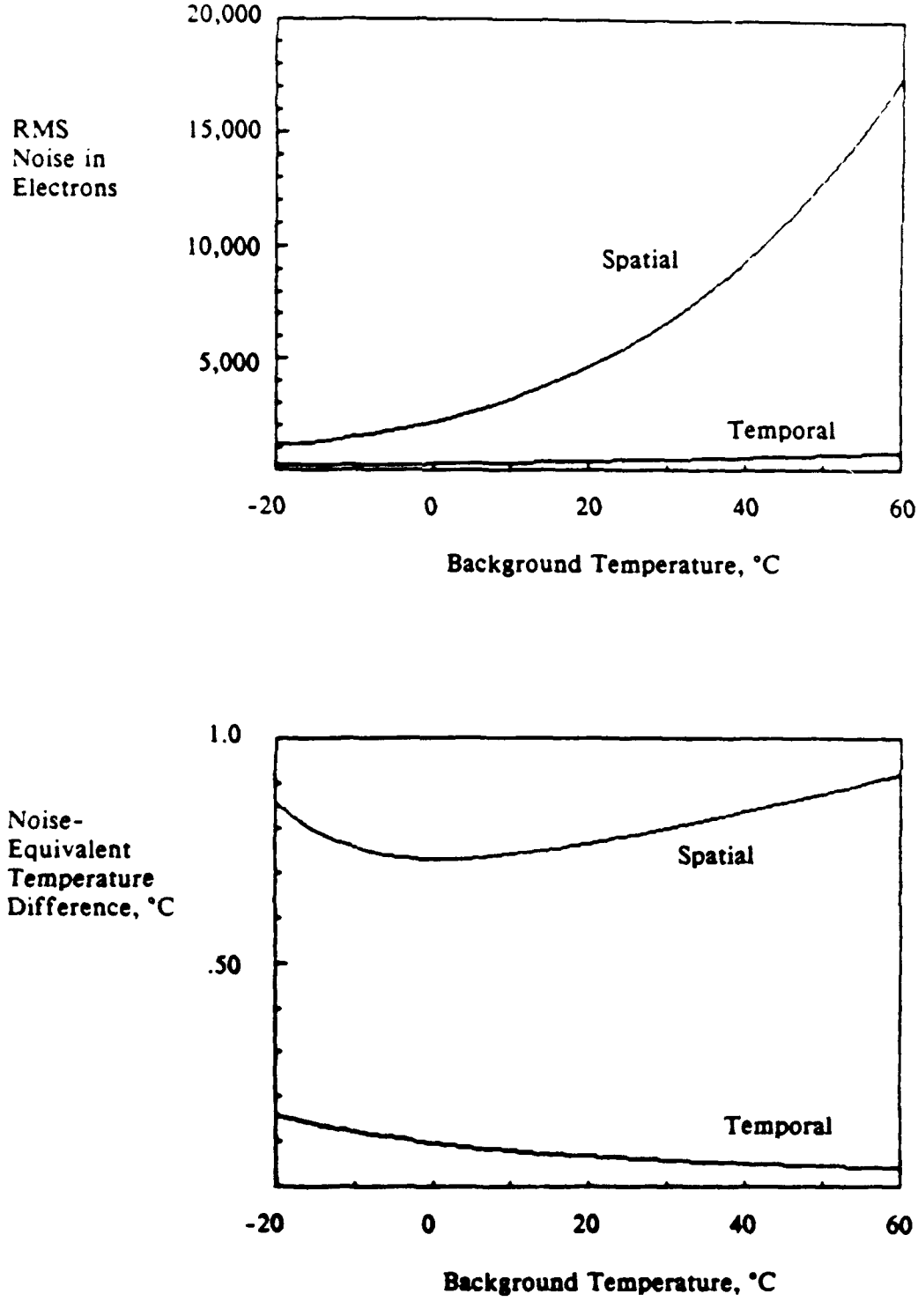

Figure 2.9 Combined spatial noise effects versus background temperature

Figure 2.9 illustrates the combined effect of dark charge, response coefficient, and barrier height nonuniformities. Nonuniformity levels are 4 percent, 2 percent, and 0.25 percent, respectively. The spatial noise shown in the lower plot of Figure 2.9 is expressed in equivalent source temperature units. Note that the spatial noise is largely independent of background temperature, with a weak minimum value at a background temperature of 0°C. This minimum occurs because the dark charge spatial noise of Figure 2.6 is a decreasing function of background temperature, whereas the spatial noise associated with the response coefficient and barrier height (Figures 2.7 and 2.8) are increasing functions of background temperature.

Note that at 26°C, the spatial noise plotted in these figures agrees with the predictions of Table 2.3. This comparison provides a check of the statistical approach of Eq. (2.9) through (2.23).

This concludes the discussion of the uncorrected response of a PtSi camera. The most important result of this discussion is held in Eq. (2.13). Equation (2.13) suggests that nonuniformity effects can be reduced through appropriate external processing. In particular, the additive and multiplicative errors appear to be completely correctable. Removal of these unwanted nonuniformity terms will be discussed in detail in the following two sections.

Residual Spatial Noise Under One-Point Correction

One-point correction requires the use of a single uniform source temperature to characterize the nonuniformity of the imaging device. During characterization, the camera views only the uniform source. The average output of each detector is recorded. When the user is ready to observe the desired thermal scene, this correction frame is simply subtracted from all subsequent camera outputs. The result is a large reduction in the spatial

noise, if the observed scene temperatures are close to the characterization temperature. In this section the benefits of this scheme are analyzed.

To better understand how the one-point correction works, consider the following simple example. Table 2.4 shows hypothetical outputs from a PtSi camera for three uniform background temperatures. The entries shown in the table are similar to the 26°C data of Table 2.3, illustrating the effect of typical detector-to-detector variations. As before, these values were obtained by integrating Eq. (2.7), using the camera characteristics of earlier discussions.

Table 2.5 shows the effect of performing a one-point correction on this data, using a calibration at 0°C. The one-point calculation was performed by considering each row of the table individually. Each entry in the row was offset by a single constant, such that all rows produce the same response at the calibration temperature.

Post-correction errors relative to the nominal output are shown in Table 2.6, for the 26°C data point. These values may be directly compared to the values in the far right column of Table 2.3. Recall that Table 2.3 illustrates the impact of uncorrected nonuniformity effects. The one-point correction has entirely removed the dark charge nonuniformity. Comparing the last two rows of Table 2.6 to Table 2.3, the response coefficient and barrier height nonuniformities have been considerably reduced.

Clearly, the correction is easily computed, and offers reasonable improvements in performance. An exact analysis of these improvements follows.

Consider now a uniform source whose temperature is T_{cal1}. This temperature shall be defined as the one-point characterization temperature. Equation (2.13) may be used to calculate the device output at this temperature.

Table 2.4

PtSi Camera Response Variation Versus Temperature

Conditions	0°C Output in e^-	26°C Output in e^-	50°C Output in e^-
Nominal	87,636	215,756	472,653
+4% D_{ij}	88,436	216,556	473,453
+2% R_{ij}	88,988	219,671	481,706
-0.25% ψ_{ms-ij}	89,185	219,954	481,869

Table 2.5

PtSi Camera Output Under One-Point Correction

Conditions	One-Point Offset Term	Corrected Outputs in e^- 0°C	26°C	50°C
Nominal	0	87,636	215,756	472,653
+4% D_{ij}	-800	87,636	215,756	472,653
+2% R_{ij}	-1352	87,636	218,319	480,354
-0.25% ψ_{ms-ij}	-1549	87,636	218,405	480,320

Table 2.6

Residual Error Under One-Point Correction

Conditions	Corrected 26°C Output	Residual Error e^- &	°C
Nominal	215,756	$0e^-$	0.00 Deg.
+4% D_{ij}	215,756	$0e^-$	0.00 Deg.
+2% R_{ij}	218,319	$2563e^-$	0.35 Deg.
-0.25% ψ_{ms-ij}	218,405	$2649e^-$	0.36 Deg.

$$N_{ij}(T_{cal1}) = \langle N_{ij}(T_{cal1}) \rangle + d_{ij} + \frac{r_{ij}}{\langle R_{ij} \rangle}[\langle N_{ij}(T_{cal1}) \rangle - \langle D_{ij} \rangle] + \langle R_{ij} \rangle \int_{\lambda_1}^{\lambda_2} \kappa_{ij}(\lambda) L(\lambda, T_{cal1})\, d\lambda \tag{2.24}$$

Following the prescription for a one-point correction, this output must be subtracted from the uncorrected output of Eq. (2.13). The result of this subtraction is the one-point corrected output, $O_{ij}(T_S)$. Usually, an additional constant, $\langle N_{ij}(T_{cal1}) \rangle$, is added to this result so that the mean value of the corrected output is equal to the mean value of the uncorrected output. The final value for $O_{ij}(T_S)$ then is

$$O_{ij}(T_s) = \langle N_{ij}(T_s) \rangle + \frac{r_{ij}}{\langle R_{ij} \rangle}[\langle N_{ij}(T_s) \rangle - \langle N_{ij}(T_{cal1}) \rangle] + \langle R_{ij} \rangle \int_{\lambda_1}^{\lambda_2} \kappa_{ij}(\lambda)[L(\lambda, T_s) - L(\lambda, T_{cal1})]\, d\lambda \quad . \tag{2.25}$$

This is the complete expression for a one-point corrected camera. The spatial noise present in the camera output may be found by taking the variance of Eq. (2.25). This result is shown in the following expression. R_{ij} and $\kappa_{ij}(\lambda)$ have again been assumed independent.

$$\sigma_O^2 = \frac{\sigma_R^2}{\langle R_{ij} \rangle^2}[\langle N_{ij}(T_s) \rangle - \langle N_{ij}(T_{cal1}) \rangle]^2 + \langle R_{ij} \rangle^2 \left\langle \left\{ \int_{\lambda_1}^{\lambda_2} \kappa_{ij}(\lambda)[L(\lambda, T_s) - L(\lambda, T_{cal1})]\, d\lambda \right\}^2 \right\rangle \tag{2.26}$$

Consider now the uncorrected noise of Eq. (2.15) and the result of Eq. (2.26). Under one-point correction, the dark charge term has been removed. Additionally, if the

ource temperature, T_S, is close to the calibration temperature, T_{cal1}, the spatial noise is essentially eliminated. When observing thermal scenes near T_{cal1}, the full performance potential of the camera is realized. Under these highly corrected conditions, the only significant noise source is that of the background itself.

The general result of Eq. (2.26) may be used to predict the one-point corrected spatial noise of a PtSi camera. This is done by substituting Eq. (2.22) for $\kappa_{ij}(\lambda)$. The result of this substitution is as shown below.

$$\sigma_O^2 = \frac{\sigma_{R'}^2}{\langle R'_{ij} \rangle^2} \left[\langle N_{ij}(T_s) \rangle - \langle N_{ij}(T_{cal1}) \rangle \right]^2 + 4\sigma_P^2 \langle R'_{ij} \rangle^2 \left\{ \int_{\lambda_1}^{\lambda_2} \left(1 - \frac{\lambda}{1.24} \langle \psi_{ms} \rangle \right) \left[L(\lambda, T_s) - L(\lambda, T_{cal1}) \right] d\lambda \right\}^2 \tag{2.27}$$

Recall that the definitions for R'_{ij} and $\eta'_{ij}(\lambda)$ given in Eqs. (2.16) and (2.17) must be used to evaluate this expression. Although not stated explicitly in the previous section, the spatially averaged quantum efficiency $\langle \eta'_{ij}(\lambda) \rangle$ used to compute $\langle N_{ij}(T) \rangle$ is

$$\langle \eta'_{ij}(\lambda) \rangle = \frac{\lambda}{1.24} \left[\left(\frac{1.24}{\lambda} - \langle \psi_{ms\text{-}ij} \rangle \right)^2 + \sigma_P^2 \right] . \tag{2.28}$$

$$\langle \eta'_{ij}(\lambda) \rangle \approx \frac{\lambda}{1.24} \left[\frac{1.24}{\lambda} - \langle \psi_{ms\text{-}ij} \rangle \right]^2 \tag{2.29}$$

Equation (2.29) is a reasonable approximation to Eq. (2.28) when used under integration with $L(\lambda, T)$. These functions are not valid beyond the wavelength at which the weakest responding photodiode reaches cutoff.

Figures 2.10 through 2.12 graphically illustrate the behavior of a PtSi camera under one-point correction. As in earlier figures, the spatial noise is plotted as a function of background temperature. All nominal camera parameters are the same as in previous examples. The one-point calibration temperature was chosen to be 0°C.

Figures 2.10 and 2.11 show the first and second terms, respectively, of Eq. (2.27). The rms nonuniformity in the response coefficient and barrier height are 2 percent and 0.25 percent, respectively. Figure 2.12 shows the combined effect of both sources of nonuniformity. Note that in all of these plots, the spatial noise is indeed zeroed at the calibration temperature. Note also that the spatial noise at 26°C agrees with the predictions of Table 2.6. This comparison provides a check on the statistical approach of Eqs. (2.24) through (2.29).

In Figure 2.12, there is a temperature range of about five degrees over which the spatial noise is less than the NETD. For some applications, a single-point correction alone may allow fulfillment of system requirements.

In applying the one-point scheme, there are at least two approaches to selection of the calibration temperature. One approach is to attempt to achieve some level of correction for all background temperatures in the operating temperature range. A comparison of Figure 2.12 to Figure 2.9 shows this criterion has nearly been met. Note that the corrected noise is actually a little worse than the uncorrected noise on the low end of the temperature scale. With this approach, the user must accept the particular calibration point which best controls the corrected noise at the endpoints of the operating temperature range.

Alternatively, the user may choose to calibrate the camera at a temperature for which complete correction of spatial noise is desired. In this case, the corrected noise may significantly exceed the uncorrected noise at one end of the temperature range, but good performance is guaranteed near the temperature of interest.

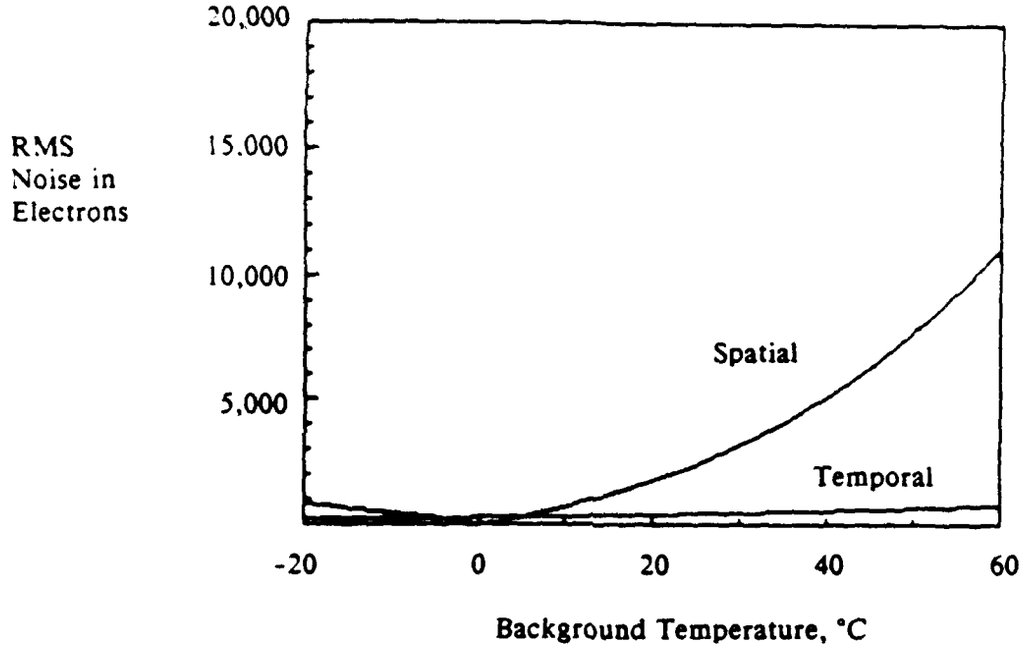

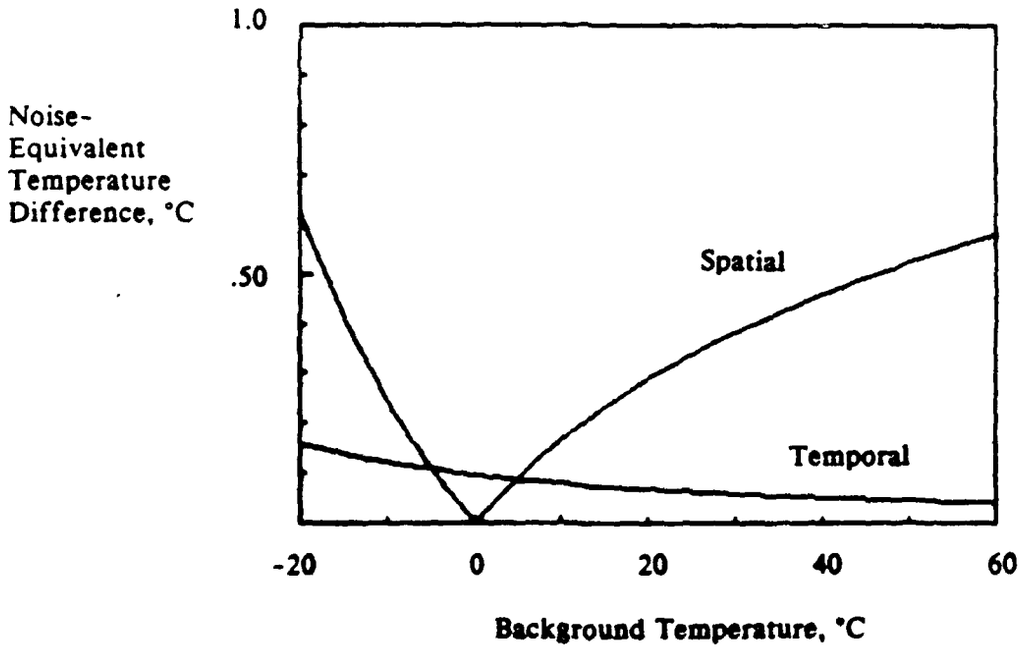

Figure 2.10 One-point-corrected spatial noise versus background temperature for 2 percent response coefficient nonuniformity

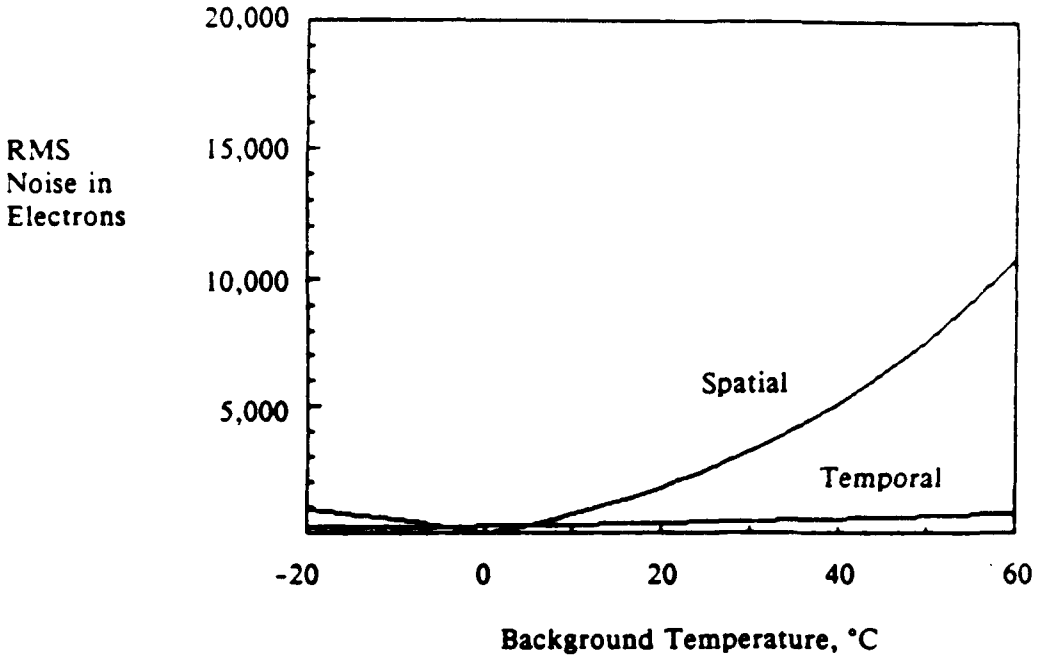

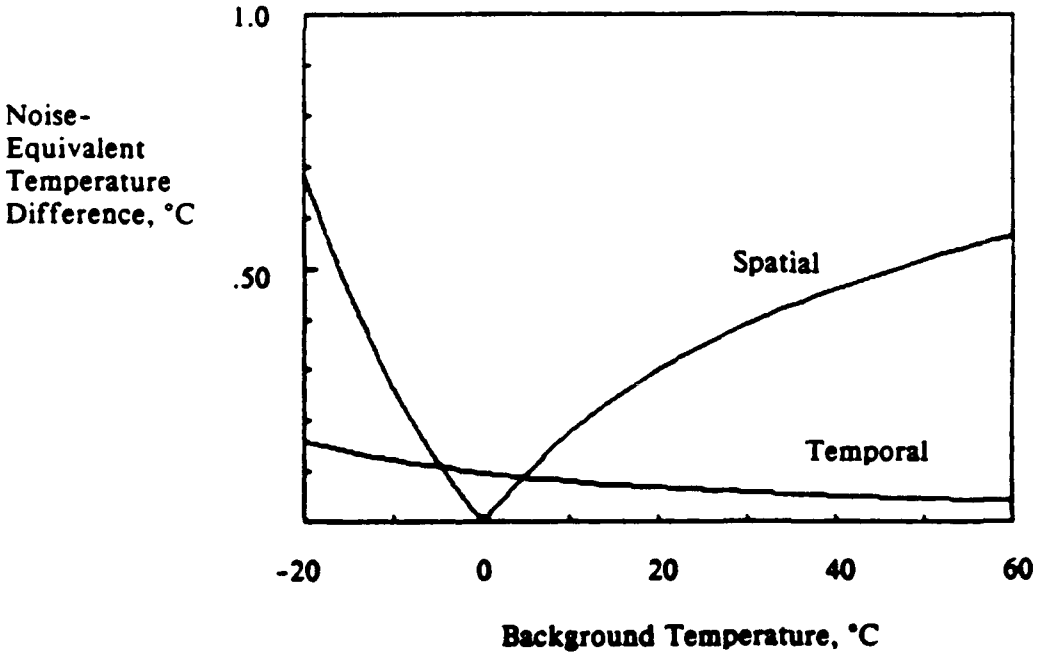

Figure 2.11 One-point-corrected spatial noise versus background temperature for 0.25 percent barrier height nonuniformity

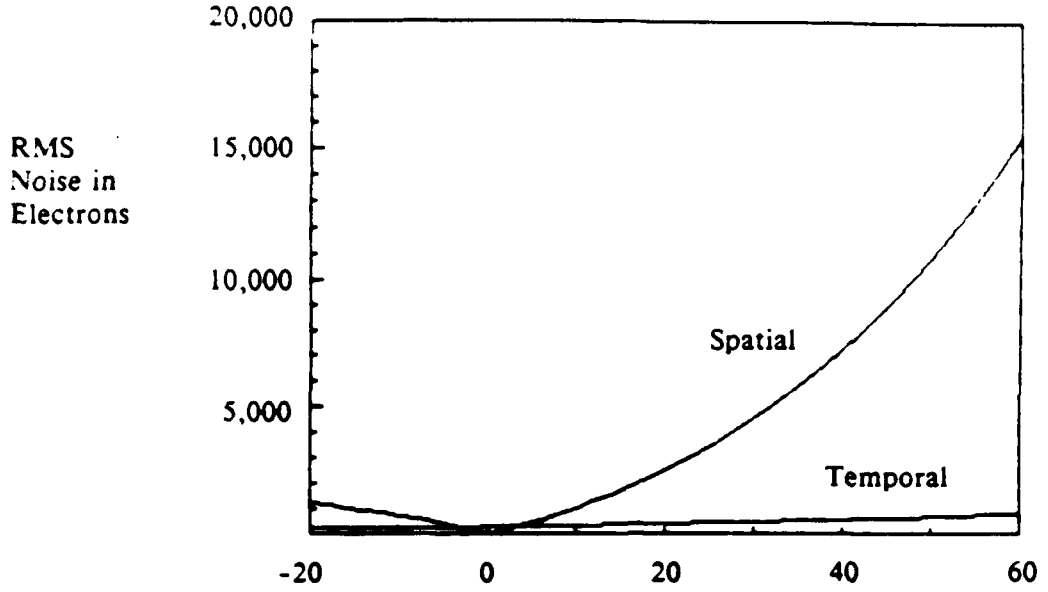

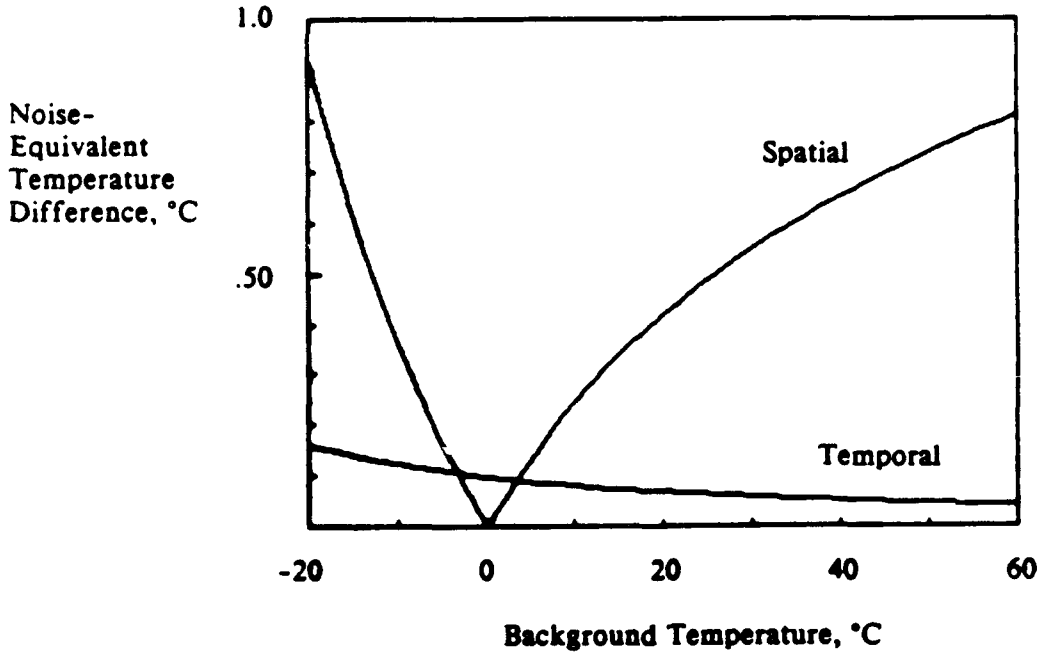

Figure 2.12 One-point-corrected spatial noise versus background temperature for combined response coefficient and barrier height nonuniformity

In the examples of spatial noise considered thus far, it has been assumed that the user is operating the camera over the full waveband offered by the imaging device. This allows the user to achieve low NETD values. An interesting option exists in PtSi camera systems when the user is free to restrict the optical bandwidth.

Consider the case in which the user can tolerate somewhat higher NETD values than that achieved for the entire waveband. Given a design NETD value, the user is free to select a sub-band within the 3.0 - 5.0 μm range. Trial calculations have shown that sub-bands near the low end of the 3.0 - 5.0 μm range can both meet the NETD requirement and minimize the effects of barrier height nonuniformity.

This concludes a discussion of the one-point correction scheme. It has been shown that this simple method can eliminate spatial noise completely near the system calibration temperature. The corrected camera output, represented by Eq. (2.25), still contains a multiplicative nonuniformity term. Removal of this term is considered in the following section.

Residual Spatial Noise Under Two-Point Correction

As suggested in the previous section, the two-point correction scheme can be used to lessen the effects of both offset and response coefficient nonuniformities. In practice, the user must calibrate the camera system by viewing uniform sources at two distinct temperatures. The use of two temperatures permits calculation of the usual one-point correction term, as well as a multiplier term. As in the one-point method, correction terms are calculated for each pixel in the imaging device. This method is more difficult to implement in hardware, but rewards the user with dramatic reductions in spatial noise.

Before considering the mathematics of the two-point correction scheme in detail, a simple example is appropriate. Recall that Table 2.5 indicates the output of a one-point-corrected PtSi camera.

Table 2.7 shows the result of multiplicatively scaling the data of Table 2.5. The 26°C and 50°C outputs, relative to the 0°C output, have been scaled by the indicated factors. The factors were chosen such that exact nonuniformity correction is now obtained at both 0°C and at 50°C.

Post-correction errors relative to the nominal output are shown in Table 2.8, for the 26°C data point. These values may be directly compared to the far right column of Table 2.3. Recall that Table 2.3 illustrates the impact of uncorrected nonuniformity effects.

The two-point correction has entirely removed the dark charge and response coefficient nonuniformities. Comparing the last row of Table 2.8 to Table 2.3, barrier height nonuniformity has been greatly reduced. The excellent performance offered by the two-point scheme will now be further examined, using a mathematical approach.

To begin the analysis, consider a one-point-corrected camera whose calibration point is T_{cal1}. Equation (2.25) may be used to predict the output of this system when viewing the second calibration source. Let the temperature of the second source be represented by T_{cal2}. The output of the camera at T_{cal2} is as shown.

$$O_{ij}(T_{cal2}) = \langle N_{ij}(T_{cal2})\rangle + \frac{r_{ij}}{\langle R_{ij}\rangle}[\langle N_{ij}(T_{cal2})\rangle - \langle N_{ij}(T_{cal1})\rangle] + \langle R_{ij}\rangle \int_{\lambda_1}^{\lambda_2} \kappa_{ij}(\lambda)[L(\lambda, T_{cal2}) - L(\lambda, T_{cal1})]\, d\lambda \tag{2.30}$$

This expression may be rewritten by introducing the new terms m_{ij}, K_1 and F_1.

$$O_{ij}(T_{cal2}) = \frac{\langle N_{ij}(T_{cal2})\rangle - \langle N_{ij}(T_{cal1})\rangle}{m_{ij}} + \langle N_{ij}(T_{cal1})\rangle \tag{2.31}$$

Table 2.7

PtSi Camera Output Under Two-Point Correction

Conditions	Two-Point Multiplier	Corrected Outputs in e^-		
		0°C	26°C	50°C
Nominal	1.00	87,636	215,756	472,653
+4% D_{ij}	1.00	87,636	215,756	472,653
+2% R_{ij}	0.98	87,636	215,756	472,653
-0.25% ψ_{ms-ij}	0.98	87,636	215,852	472,653

Table 2.8

Residual Error Under Two-Point Correction

Conditions	Corrected 26°C Output in e^-	Residual Error e^- & °C	
Nominal	215,756	0e^-	0.000 Deg.
+4% D_{ij}	215,756	0e^-	0.000 Deg.
+2% R_{ij}	215,756	0e^-	0.000 Deg.
-0.25% ψ_{ms-ij}	215,852	96e^-	0.013 Deg.

$$m_{ij} = \frac{1}{1 + \frac{r_{ij}}{\langle R_{ij} \rangle} + \frac{F_1}{K_1}} \tag{2.32}$$

$$K_1 = \langle N_{ij}(T_{cal2}) \rangle - \langle N_{ij}(T_{cal1}) \rangle \tag{2.33}$$

$$F_1 = \langle R_{ij} \rangle \int_{\lambda_1}^{\lambda_2} \kappa_{ij}(\lambda) [L(\lambda, T_{cal2}) - L(\lambda, T_{cal1})] \, d\lambda \tag{2.34}$$

When written in this way, an appropriate algorithm for the two-point correction is easily obtained. Let the two-point-corrected output be denoted by $W_{ij}(T)$. If we require that the two-point correction be perfect at the second calibration point, then all $W_{ij}(T_{cal2})$ must identically equal a constant. Let that constant be $\langle N_{ij}(T_{cal2}) \rangle$. Substituting $W_{ij}(T_{cal2})$ for $\langle N_{ij}(T_{cal2}) \rangle$ in Eq. (2.31) yields the following expression.

$$W_{ij}(T_{cal2}) = [O_{ij}(T_{cal2}) - \langle N_{ij}(T_{cal1}) \rangle] \, m_{ij} + \langle N_{ij}(T_{cal1}) \rangle \tag{2.35}$$

By now substituting T_s for T_{cal2} in this expression, an operational definition for the two-point correction is obtained.

$$W_{ij}(T_s) = [O_{ij}(T_s) - \langle N_{ij}(T_{cal1}) \rangle] \, m_{ij} + \langle N_{ij}(T_{cal1}) \rangle \tag{2.36}$$

This algorithm guarantees that spatial noise is zeroed at the two calibration points. In practice, the two-point coefficients m_{ij} are calculated by using Eq. (2.31), during the camera characterization.

Now that the two-point algorithm has been explicitly defined, an expression for the residual spatial noise may be derived. This is done by first writing an expression for $O_{ij}(T_s)$. As in the case of $O_{ij}(T_{cal2})$, $O_{ij}(T_s)$ is obtained through use of Eq. (2.25). The new terms F_2 and F_3 were introduced to simplify further manipulations.

$$O_{ij}(T_s) = \langle N_{ij}(T_s) \rangle + \frac{r_{ij}}{\langle R_{ij} \rangle} F_2 + F_3 \tag{2.37}$$

$$F_2 = [\langle N_{ij}(T_s) \rangle - \langle N_{ij}(T_{cal1}) \rangle] \tag{2.38}$$

$$F_3 = \langle R_{ij} \rangle \int_{\lambda_1}^{\lambda_2} \kappa_{ij}(\lambda) [L(\lambda, T_s) - L(\lambda, T_{cal1})] \, d\lambda \tag{2.39}$$

Note the similarity between F_2 and K_1, and between F_3 and F_1. The terms F_2 and F_3 become K_1 and F_1, respectively, as T_s approaches T_{cal2}.

Substituting Eq. (2.37) into Eq. (2.36), and rearranging terms, the following expression is obtained.

$$W_{ij}(T_s) = \left\{ \left[1 + \frac{r_{ij}}{\langle R_{ij} \rangle} \right] F_2 + F_3 \right\} m_{ij} + \langle N_{ij}(T_{cal1}) \rangle \tag{2.40}$$

Further manipulation of Eq. (2.40) is hampered by the quotient form of m_{ij}. Recall that m_{ij} is given by Eq. (2.32). To obtain a more usable form of Eq. (2.40), an approximation to Eq. (2.32) may be made.

For small values of ε, the expression $1/(1 + \varepsilon)$ is closely approximated by $(1 - \varepsilon)$. This relationship may be applied to Eq. (2.32) by noting that, indeed, the far right terms in

the denominator are small. They are in the range 0 - 0.02 for the examples considered thus far. The new expression for Eq. (2.32) is as shown.

$$m_{ij} \approx \left[1 - \frac{r_{ij}}{\langle R_{ij} \rangle}\right] - \frac{F_1}{K_1} \tag{2.41}$$

Using Eq. (2.41) in Eq. (2.40) yields the desired result. After significant algebraic manipulation, and discarding unimportant terms, the following expression for the two-point corrected output is obtained.

$$W_{ij}(T_s) \approx \langle N_{ij}(T_s) \rangle + F_2 \left(\frac{F_3}{F_2} - \frac{F_1}{K_1}\right) \tag{2.42}$$

The spatial noise present in the camera output may be found by taking the variance of Eq. (2.42). This result is shown in the following expression.

$$\sigma_W^2 \approx F_2^2 \left\langle \left(\frac{F_3}{F_2} - \frac{F_1}{K_1}\right)^2 \right\rangle \tag{2.43}$$

Consider now the uncorrected noise of Eq. (2.15), and the result of Eq. (2.43). Under two-point correction, the dark charge and response coefficient nonuniformity terms have both been removed. Additionally, if the source temperature T_s is close to a calibration temperature, T_{cal1} or T_{cal2}, the spatial noise is essentially eliminated. The magnitude of the residual spatial noise away from the calibration points depends on the specific form of $\kappa_{ij}(\lambda)$, and on the temperature difference between calibration points.

The general result of Eq. (2.43) may be used to predict the two-point-corrected spatial noise of a PtSi camera. This is done by substituting Eq. (2.22) for $\kappa_{ij}(\lambda)$. The result of this substitution is shown below.

$$\sigma_W^2 \approx 4\,\sigma_P^2 \left[\langle N_{ij}(T_s) \rangle - \langle N_{ij}(T_{cal1}) \rangle \right]^2 \times \tag{2.44}$$

$$\langle R'_{ij} \rangle^2 \left[\frac{\int_{\lambda_1}^{\lambda_2} \left(1 - \frac{\lambda}{1.24} \langle \psi_{ms\text{-}ij} \rangle\right) \left[L(\lambda, T_s) - L(\lambda, T_{cal1}) \right] d\lambda}{\langle N_{ij}(T_s) \rangle - \langle N_{ij}(T_{cal1}) \rangle} \right.$$

$$\left. - \frac{\int_{\lambda_1}^{\lambda_2} \left(1 - \frac{\lambda}{1.24} \langle \psi_{ms\text{-}ij} \rangle\right) \left[L(\lambda, T_{cal2}) - L(\lambda, T_{cal1}) \right] d\lambda}{\langle N_{ij}(T_{cal2}) \rangle - \langle N_{ij}(T_{cal1}) \rangle} \right]^2$$

Figure 2.13 graphically illustrates the behavior of a PtSi camera under two-point correction. As in earlier figures, the spatial noise is plotted as a function of background temperature. All nominal camera parameters are the same as in previous examples. The two-point calibration temperatures are 0°C and 50°C.

The rms spatial noise of Figure 2.13 was predicted by Eq. (2.44), for a 0.25 percent level of barrier height nonuniformity. Note that the residual noise at 26°C agrees exactly with the predictions of Table 2.8. This comparison provides a check on the mathematical approach and approximations of Eqs. (2.30) through (2.44).

The two-point-corrected performance of this example is extremely good. At no point in the operating range does the spatial noise exceed the NETD. The user of such a camera may reduce the residual spatial noise to arbitrarily low levels, simply by reducing the temperature difference between calibration points. In extremely critical applications,

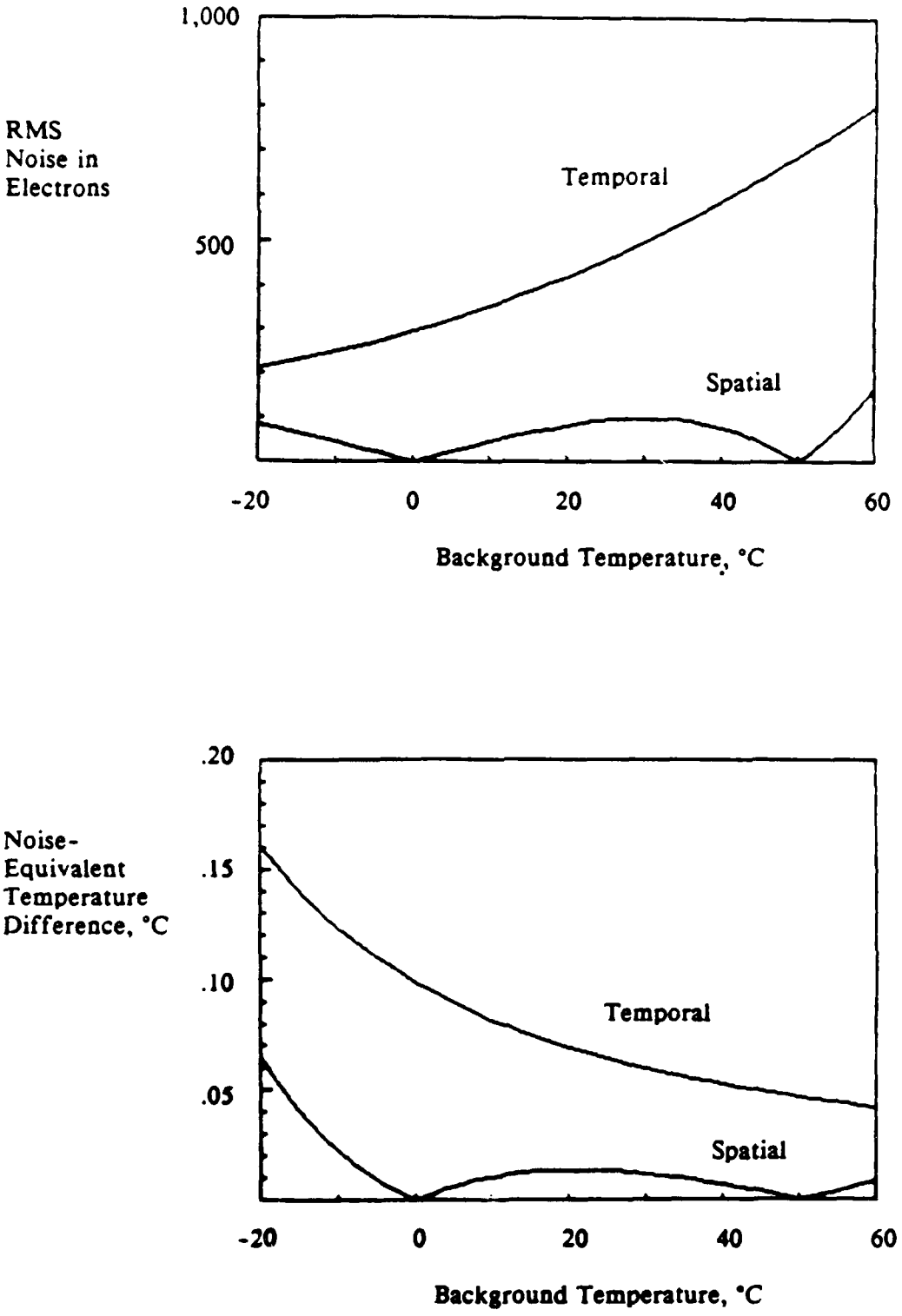

Figure 2.13 Two-point-corrected spatial noise versus background temperature for 0.25 percent barrier height nonuniformity

multiple two-point corrections or a look-up table approach might be used to cover a broad operating range.

Given the simplicity and effectiveness of a single two-point correction, all further discussions of nonuniformity will assume its use.

Summary of Linear Theory of Nonuniformity

A linear theory of nonuniformity was developed in preceding sections. It was specifically applied to PtSi imaging devices. Typical spatial noise levels were compared to the temporal noise. Uncorrected spatial noise was found to greatly exceed the NETD. It was shown that adequate thermal imaging performance may be obtained over a limited range under one-point correction. More demanding applications require use of the two-point correction. In this case, the level of residual noise may be controlled by restricting the temperature difference between calibration points.

Nonlinear Effects in the Hughes 256 × 256 Hybrid Imaging Device

The linear theory of nonuniformity discussed in previous sections is adequate for general analysis of PtSi imaging devices. In that approach, two fundamental assumptions are made. The quantum efficiency must be constant throughout the optical integration cycle, and the electronic readout mechanism must be linear. In practice, it is known that these assumptions are not always valid.

In PtSi detectors, the quantum efficiency is a weak function of detector bias. In present-day imaging devices, this bias voltage decreases as a function of collected photocharge. Additionally, in hybrid devices such as the CRC-365, the voltage transfer function from the detector to the output is nonlinear. These effects make small but

measurable contributions to the thermal response. Determining the impact of these nonlinear effects, specifically for the CRC-365, is the subject of this section.

Recall that each photodiode in the CRC-365 is connected directly to the input of its own source-follower amplifier. This was shown schematically in Figure 2.1. To simplify the analysis that follows, the input admittance of this amplifier shall be considered to be purely capacitive, and independent of the input voltage. By making this assumption, the nonuniformity properties of the photodiodes may be analyzed without considering the remainder of the readout device explicitly, and vice versa.

Nonlinearity of Detector Response with De-Biasing

With the Hughes CRC-365, and with other devices of its type, one may think of the photodiode as performing two distinctly different functions. Its primary function is to respond to incoming infrared radiation. It does so by separating photogenerated hole-electron pairs, which form in the vicinity of the Schottky barrier. Its secondary function, in conjunction with the readout device input circuit, is to convert the photocharge to a change in voltage. This change in voltage is the quantity relayed to the outside world, via the source followers of the readout.

The charge-to-voltage conversion takes place across the parallel combination of the PtSi photodiode capacitance and the input capacitance of the readout device. At the beginning of the optical integration cycle, the potential across the photodiode is at a maximum. The potential drops as photocharge accumulates. A typical potential versus time plot was shown earlier in Figure 2.2.

Since the quantum efficiency is a function of voltage, it changes continuously throughout the optical integration cycle. Its value decreases with reduced bias levels. The capacitance of the PtSi photodiode is also a function of voltage. As the potential across the diode drops, its capacitance increases.

It is now clear that both the detection and charge-to-voltage functions depend on the instantaneous bias across the photodiode. The overall photoresponse decreases throughout the integration cycle.

To further illustrate these effects, consider a hypothetical example in which a neutral density filter is used to attenuate the optical signal present at the imaging device. If the filter had a transmittance of 50 percent, one might expect the device output to drop by 50 percent as the filter is inserted into the optical path. In fact, due to the bias dependence of the photoresponse, the output would drop by somewhat less than 50 percent. This effect shall variously be referred to as response nonlinearity, or simply nonlinearity.

Nonlinearity by itself would not pose a serious problem, if each detector and its associated input circuit were identical. If, however, the individual detectors and their input circuits vary spatially, the overall effect of these nonuniformities will be modified by the presence of the nonlinearity. Determining the extent to which nonlinearity impacts earlier linear predictions of post-correction spatial noise is the goal of the following analysis.

In performing this analysis, the nonlinearity of dark charge generation was also included. A total of four bias-dependent photodiode properties were considered overall. These include the dark charge generation rate, the Schottky barrier height and quantum yield, and the depletion capacitance. Before describing this nonlinear analysis in detail, the voltage dependence of each of these detector properties will be introduced.

A mathematical statement for the photodiode output voltage, V_R, makes use of the familiar charge-voltage relationship for a capacitor. The usual (i,j) subscript notation will be dropped for this analysis to simplify notation.

$$V_R = V_{reset} - \frac{Q_{acc}}{C(V_R)} \tag{2.45}$$

Here, $C(V_R)$ represents the voltage-dependent capacitance of the detector and amplifier input node. Q_{acc} is the instantaneous value for the photocharge, in Coulombs. V_{reset} is the reset voltage to which the photodiode is initially biased. All variables in Eq. (2.45) are positive in sign.

As mentioned earlier, the detector capacitance, $C_{ptsi}(V_R)$, and amplifier input capacitance, C_{gate}, combine in parallel. This is expressed as follows.

$$C(V_R) = C_{gate} + C_{ptsi}(V_R) \tag{2.46}$$

A suitable expression for $C_{ptsi}(V_R)$ is given by Sze (Sze, 1981). It may be simplified by requiring that the reverse-bias voltage across the photodiode, V_R, is much larger than the built-in potential, V_{bi}. In this analysis, V_R will never be less than about 3 Volts, whereas the built-in potential is about 0.2 Volt. The simplified expression is as shown.

$$C_{ptsi}(V_R) = A\left(\frac{q\,\varepsilon_s\,N_a}{2V_R}\right)^{\frac{1}{2}} \quad \text{for } V_R >> V_{bi} \tag{2.47}$$

The effective impurity concentration is represented by N_a, expressed in number per cubic centimeter. The permittivity of silicon is represented by ε_s, in Farads per centimeter. Recall that A is the photodiode active area and q is the electronic charge. Consider now a trial calculation of the total capacitance one would expect in the CRC-365.

Using a reverse bias voltage of 4 Volts, an impurity concentration of 10^{15}, an active area of $(28\ \mu m)^2$, and letting ε_s be $11.8 \times 8.854 \times 10^{-14}$, one obtains about 0.035 pF for the detector capacitance. Fowler (Fowler, 1989) quotes about 0.06 pF for the input capacitance, so one would see a total capacitance of around 0.10 pF at 4 Volts.

The behavior of the Schottky barrier height with reverse bias is also described by Sze. His result is shown, where (V_R + V_{bi}) has again been replaced by V_R for this analysis.

$$\psi_{ms}(V_R) = \psi_o - \frac{q}{2\varepsilon_s}\left(\frac{2\varepsilon_s N_a V_R}{\pi^2 q}\right)^{\frac{1}{4}} \quad \text{for } V_R >> V_{bi} \tag{2.48}$$

The term ψ_o is the intrinsic barrier height in the absence of image-force barrier lowering. Its value is in the range 0.24 - 0.25 eV. If one uses a ψ_o value near 0.24 eV, for example, and the N_a, ε_s and reverse bias values quoted earlier, 0.22 eV is obtained for the barrier height. Recall that this was the value used in all previous quantum efficiency calculations.

The behavior of the Schottky quantum yield (C_1) versus bias is given in an article by Mooney (Mooney, 1989b). His results are as shown, again replacing (V_R + V_{bi}) by V_R for this analysis.

$$C_1(V_R) = C_{1o} e^{-(x_m / l_s)} \tag{2.49}$$

$$x_m = \frac{1}{4}\left(\frac{q}{2\pi^2 \varepsilon_s N_a V_R}\right)^{\frac{1}{4}} \quad \text{for } V_R >> V_{bi} \tag{2.50}$$

The term x_m, representing the metal-to-barrier distance in the silicon, was provided by Sze. The term l_s is the mean free path for holes in silicon. Mooney quotes a typical l_s value of around 70 Angstroms in his article. The term C_{1o} is a scaling constant. In this analysis, C_{1o} includes the yield enhancements of the optical cavity discussed earlier.

As an example, consider using the N_a, ε_s, and bias values of previous examples. For a C_{1o} of about 0.30 eV^{-1}, one obtains a quantum yield of 0.20 eV^{-1} at 4 Volts. Recall that this was the C_1 used in all previous quantum efficiency calculations.

The reverse current density of a PtSi photodiode, J_{sat}, is also given by Sze. Making the V_R simplification used earlier, his expression is as follows.

$$J_{sat}(V_R) = A^* T^2 e^{-[q \psi_{th}(V_R) / kT]} \tag{2.51}$$

The term T is the temperature of the detector in degrees Kelvin. The term A* is called Richardson's constant. Its value, for holes in p-type silicon, is 32 Amps per cm^2 (Kittel, 1960; Silverman, 1986). The term $\psi_{th}(V_R)$ is the thermal barrier height, including image-force lowering. The thermal barrier height is typically 0.04 eV or so below the optical barrier height, $\psi_{ms}(V_R)$ (Mooney, 1987). Since the thermal barrier height is subject to the same image-force effects as the optical barrier height, the following approximation will be used.

$$\psi_{th}(V_R) \approx \psi_{ms}(V_R) - \psi_{ms\text{-}th} \tag{2.52}$$

The term $\psi_{ms\text{-}th}$ was introduced to account for the barrier height difference noted earlier. For simplicity, this term will be considered to be spatially invariant.

As an example, if $\psi_{ms}(V_R)$ and $\psi_{ms\text{-}th}$ were 0.22 eV and 0.022 eV, respectively, then the thermal barrier height would be 0.198 eV. Using this in Eq. (2.51), at 77.3°K, a dark current density of about 25 nA per cm^2 is obtained. Recall that the optical integration cycle for the CRC-365 is 1/60 second, and that the active detector area is $(28\ \mu m)^2$. Under these conditions, 20,000 electrons per integration cycle would be generated if the detector

was kept at constant bias. Recall that 20,000 electrons was the value used in all previous analyses requiring the dark charge.

In review of these new relationships, note that detector (i,j) is now described by six spatially varying quantities. Table 2.9 summarizes these quantities.

Recall that in the linear theory of nonuniformity, each detector was uniquely defined by its area, barrier height, quantum yield, and total dark charge per cycle. That theory may now be seen as a special case of the present situation. The linear theory is valid only when the bias does not change significantly during optical integration.

Now that the various voltage dependences have been explicitly defined, their impact on nonuniformity may be calculated. This is done by first solving for the photoresponse of a nominal detector. To predict the nonuniformity effects, the various quantities of Table 2.9 may then be incrementally perturbed, and the resulting detector photoresponses compared to the nominal photoresponse.

Due to the number and complexity of individual bias dependences involved, a computer simulation was used to calculate the photoresponses. It is believed that Orias (Orias, 1986) used this type of approach in his analysis of the Hughes Aircraft Company CRC-228. The CRC-228 is a 58 x 62 DRO focal plane array fitted with Indium Antimonide photodiodes.

In this approach, the optical integration time is divided into a large number of equal sub-intervals. If small enough time increments are used, all the voltage-dependent parameters of the detector may be treated as constants during these sub-intervals.

A personal computer was programmed to evaluate Eq. (2.7) for each of 100 sequential time sub-intervals. Recall that this expression gives the total amount of signal charge expected from a PtSi detector. In calculating R_{ij}, a scaled optical integration time of

Table 2.9

Defining Quantities for Nonlinear PtSi Photodiode (i,j)

Active area, A

Intrinsic barrier height, ψ_o

Initial quantum yield, C_{1o}

Effective impurity concentration, N_a

Readout input capacitance, C_{gate}

Reset voltage, V_{reset}

0.01 times the usual 1/60 second was used. The dark charge accumulation during each sub-interval was computed with the following expression.

$$D(V_R) = \frac{J_{sat}(V_R)\, A\, t_{int}}{100q} \tag{2.53}$$

Before the first time sub-interval, all voltage-dependent detector parameters were initialized by setting V_R equal to V_{reset}. The photocharge, Q_{acc}, was initialized to zero.

A running sum was kept on the photocharge. The reverse voltage, V_R, was determined as follows. Starting from its initial value of V_{reset}, the change in V_R was calculated at the end of each sub-interval. This was done by dividing the incremental signal charge for the sub-interval by the total capacitance for the sub-interval. The new V_R value was then taken to be its old value, plus the incremental change.

Before beginning the next sub-interval, new values for all of the voltage-dependent parameters were calculated. At the end of the 100^{th} such sub-interval, V_R was then declared to be the final photodiode output.

This iterative procedure was applied to each background temperature of interest. Table 2.10 summarizes the nominal photodiode parameters and other constants used in these simulations. All other camera parameters were those of earlier calculations.

Before attempting to assess nonuniformity effects, several preliminary simulations of the nonlinear photoresponse were done. These simulation results are shown in Table 2.11. The first row of Table 2.11 corresponds to a case in which all nonlinear effects were suppressed. These outputs are identical to the nominal linear response shown earlier in Table 2.4.

The second through fifth rows of Table 2.11 correspond to simulations in which only one of the four bias-dependent quantities was allowed to affect the photoresponse.

Table 2.10

Constants Used in Nonlinear PtSi Photodiode Simulation

Nominal Photodiode Parameters

Active area, A	$(28\ \mu m)^2$
Intrinsic barrier height, ψ_o	0.24067 eV
Initial quantum yield, C_{1o}	0.30488 eV^{-1}
Effective impurity concentration, N_a	$10^{15}\ cm^{-3}$
Reset voltage, V_{reset}	4.0 Volts
Barrier height difference, ψ_{ms-th}	0.02226 eV
Amplifier input capacitance, C_{gate}	0.06 pF

Silicon Constants

Permittivity, ε_s	$11.8 \times 8.854 \times 10^{-14}$
Hole mean free path, l_s	70 Angstroms

Table 2.11

Nonlinear PtSi Response Versus Background Temperature

Conditions	Photocharge, in e^-, and Output Voltage		
	0°C	26°C	50°C
No nonlinear effects	87,636 3.853 531	215,756 3.639 398	472,653 3.210 035
$D(V_R)$ only	87,355 3.854 000	215,065 3.640 552	471,141 3.212 562
$C_1(V_R)$ only	87,505 3.853 749	214,805 3.640 987	467,636 3.218 420
$\psi_{ms}(V_R)$ only	87,373 3.853 970	213,988 3.642 353	464,004 3.224 490
$C(V_R)$ only	87,636 3.854 538	215,756 3.645 625	472,653 3.241 168
All nonlinear effects	86,967 3.855 640	212,418 3.651 011	458,169 3.263 438

This was done to determine the relative influence of each source of response nonlinearity. In practice, all four bias-dependences occur simultaneously.

The last row of Table 2.11 corresponds to the case in which all four sources of nonlinearity are present. When the results of the last row of Table 2.11 are compared to the linear case of the first row, a slight reduction in photoresponse is seen. The photocharge and output voltage change over the 50 degree range are about 3.6 percent and 8.0 percent lower, respectively, than the linear case. The NETD at 26°C is about 2 percent greater.

Considering the voltage outputs of Table 2.11 further, note that, indeed, none of the individual effects nor the combined effects can be represented as simple slope and offset changes from the linear response shown in the first row of the table.

To quantify the relative amount of nonlinearity associated with the four voltage dependences as well as the overall nonlinearity, the two-point correction method was used.

The nonlinear responses of Table 2.11 were two-point corrected, using the linear response of its first row as a reference. In each case, the corrected 26°C response was then compared to the linear response at 26°C. These results are shown in Table 2.12, and are reported in microvolts, electrons, and equivalent source temperature units. The signal contrast for the linear case, reported earlier at around 7500 electrons per degree Kelvin, was used for scaling to equivalent source temperature units.

Remember that the two-point correction was used only to draw attention to the relative amount of nonlinearity imparted by each voltage-dependent parameter. When all voltage dependences are considered, Table 2.12 shows that the CRC-365 theoretically exhibits no more than 1.3 percent nonlinearity at 26 degrees. This is the peak nonlinearity, expressed as a fraction of the 50 degree operating range.

The voltage-dependent capacitance of the photodiode is the biggest individual contributor to the nonlinearity. This might have been guessed prior to the simulation.

Table 2.12

Relative Impact of PtSi Nonlinearity Effects

Conditions	Nonlinearity at 26°C		
	μVolts	Electrons	Temp. Diff.
$D(V_R)$ only	0	0	0.00
$C_I(V_R)$ only	-1364	816	0.11
$\psi_{ms}(V_R)$ only	-2196	1314	0.18
$C(V_R)$ only	-5041	3016	0.41
All effects	-8220	4919	0.67

Recall that the capacitance has a square root relationship to the reverse voltage, whereas the quantum efficiency is related through the fourth root. The dark current nonlinearity has no significant effect.

To conclude this discussion of preliminary nonlinearity simulations, consider the change in each voltage-dependent parameter during the optical integration period. Table 2.13 shows the initial and final values for various detector parameters, and the fractional change in each for a 26°C background temperature. The initial and final values occur at the beginning and end of the optical integration cycle, respectively.

Note that although the dark charge generation rate changes the most throughout the integration period, it has the least effect on the nonlinearity. Note also that the fixed amplifier input capacitance tends to moderate the effects of the changing photodiode capacitance.

This concludes a discussion of preliminary nonlinearity simulations. Consider now the impact of nonuniformity when nonlinear photoresponse is present.

As mentioned earlier, nonuniformity effects may be analyzed by incrementally perturbing each of the quantities appearing in Table 2.9. Two percent incremental changes were evaluated for each detector parameter, with the exception of the intrinsic barrier height. Due to its strong influence, the 0.25 percent perturbation of earlier linear examples was also retained.

These results are shown in Table 2.14. The results are arranged in order of increasing effect on the output.

Recall that under the linear theory of nonuniformity, the two-point correction scheme was used to reduce spatial noise well below the NETD. Consider now a two-point correction to the nonlinear photodiode data of Table 2.14. The two-point-corrected output at 26°C and residual errors are shown in Table 2.15. Source equivalent temperatures were

Table 2.13

PtSi Properties Versus Bias for 26°C Background

Parameter	Initial Value	Final Value	Percent Change
Dark charge per cycle, $D(V_R)$	20,000e^-	18,660e^-	-6.7
PtSi capacitance, $C_{ptsi}(V_R)$	35.86 fF	37.52 fF	+4.6
Total capacitance, $C(V_R)$	95.86 fF	97.52 fF	+1.7
Quantum yield, $C_1(V_R)$	0.20 eV^{-1}	0.1981 eV^{-1}	-0.95
Barrier height, $\psi_{ms}(V_R)$	0.22 eV	0.2205 eV	+0.23

Table 2.14

Nonlinear PtSi Response Variation Versus Temperature

Conditions	Output in Volts		
	0°C	26°C	50°C
Nominal	3.855 640	3.651 011	3.263 438
+2% N_a	3.854 983	3.649 980	3.261 905
-2% V_{reset}	3.777 425	3.574 899	3.191 546
+2% A	3.853 885	3.646 894	3.255 294
-2% C_{gate}	3.853 849	3.646 811	3.255 129
+2% C_{1o}	3.853 440	3.644 881	3.250 349
-0.25% ψ_o	3.849 832	3.640 906	3.246 191

Table 2.15

Residual Error Under Two-Point Correction with Nonlinear Photoresponse

Conditions	Corrected 26°C Output in Volts	Residual Error μ Volts	°C
Nominal	3.651 011	0	0.000
+2% N_a	3.650 940	-71	0.006
-2% V_{reset}	3.650 928	-83	0.007
+2% A	3.650 858	-153	0.013
-2% C_{gate}	3.650 856	-155	0.014
+2% C_{1o}	3.650 847	-164	0.014
-0.25% ψ_o	3.650 673	-338	0.029

obtained by using the signal contrast for the nominal nonlinear output. This value is 11.52 millivolts per degree, at 26°C.

Recall that Table 2.8 listed the residual error, under two-point correction, for a linear camera. Comparing the present results with those of Table 2.8, several interesting observations may be made.

In the present analysis, no detector property is directly analogous to the D_{ij}, or additive offset, term considered under linear theory. Such a term would be featured in the present analysis only if a hypothetical field-independent leakage term were included in the J_{sat} expression of Eq. (2.51).

In the linear theory of nonuniformity, neither N_a nor V_{reset} were considered. The nonlinear results of Table 2.15 show that even under two-point correction, these quantities can produce significant residual spatial noise.

Linear theory showed that slope errors are entirely removed under two-point correction. These were previously referred to as variations in R_{ij}. Recall that R_{ij} variations arise under linear theory whenever the detector area, A_{ij}, or the quantum yield, $C_{1\text{-}ij}$, vary spatially. In the present analysis, slope-type nonuniformities arise from variations in A_{ij}, $C_{1o\text{-}ij}$, and $C_{gate\text{-}ij}$. Table 2.15 shows that this type of nonuniformity is no longer entirely removed under two-point correction.

Linear theory additionally showed that post-correction spatial noise under two-point correction is strictly attributable to barrier height variations. Table 2.8 showed that a $\psi_{ms\text{-}ij}$ variation of 0.25 percent leaves 0.013 rms degrees of residual spatial noise at the center of the operating temperature range. In the present analysis, Table 2.15 shows that the residual spatial noise has more than doubled, for the same variation in barrier height.

The simulations of this section show that in the design and fabrication of devices such as the CRC-365, one must be concerned with at least six independent spatial

variables. To achieve the performance considered under linear theory, one would have to limit the combined effect of all six of these nonuniformity sources to around 0.015 degrees rms at 26°C.

By scaling the results of Table 2.15, one may develop a tolerance budget for design purposes. Table 2.16 illustrates this idea. The left column shows the allowable rms variation in a single variable which would produce 0.015 degree residual spatial noise, in the absence of any other spatially varying parameter. The right column shows the allowable rms variation for the same quantity, when considering its effect in R.S.S. combination with the other five variables. In this case, equal individual noise levels of 0.0062 degree were assumed.

The requirements on N_a and V_{reset} shown in Table 2.16 do not seem unreasonable. The requirements on C_{gate} and active area, A, may be interpreted in light of an article by Mooney (Mooney, 1985).

For photolithographically defined square features of dimension x, and a rms tolerance of σ_x, the uncertainty in area is $(2\ \sigma_x)/x$. If x and σ_x were 28 μm and 0.1 μm, respectively, then the achievable tolerance on area is around 0.7 percent. By this analysis, the requirements of Table 2.16 on area, and probably on C_{gate}, can be met.

The most demanding requirements of Table 2.16 are made on the quantum yield and barrier height. It is not clear from present knowledge that these tolerances can be held. In particular, the tolerance on intrinsic barrier height is extremely tight. Laboratory testing will reveal the levels to which these quantities are controlled.

In this section, it has been shown that de-biasing can affect both the quantum efficiency and charge-to-voltage conversion processes. In devices such as the CRC-365, this de-biasing reduces the effectiveness of the two-point correction.

Table 2.16

Tolerance Limits Required to Control Corrected Spatial Noise to 0.015 Degrees

Spatial Variable	Maximum Percent Variation in Variable	
	Acting Alone	In R.S.S. Combination
N_a	4.84	1.97
V_{reset}	4.17	1.68
A	2.26	0.92
C_{gate}	2.22	0.91
C_{1o}	2.10	0.86
ψ_o	0.13	0.05

Nonlinear analysis shows that, in addition to the tight control of barrier height mandated by linear analysis, control of at least five other detector and operating parameters is called for. A one percent manufacturing tolerance is suggested for the impurity concentration, active area, amplifier input capacitance, and quantum yield. Also suggested is a one percent tolerance on the detector-to-detector variation in reset potential.

It should be noted that a reduction in de-biasing can be achieved through more complex circuit designs. Work is currently in progress to use capacitance switching techniques to dramatically reduce de-biasing during the signal integration period (Salcido, 1991).

Nonlinearity of Readout Device

In the previous section, the nonlinearity associated with detector de-biasing was investigated under the assumption of an ideal readout device. In this section, the detector array shall be considered to be ideal, and the nonlinearity of the readout will be examined.

As discussed earlier, the readout device is used to sequentially address each PtSi photodiode in the detector array. As each detector is selected, the voltage across it is brought out of the readout. Ideally, one would prefer a readout device with unity gain, zero offset, no nonlinear effects, and perfect spatial uniformity.

In practice, readout devices like that used in the CRC-365 fall somewhat short of this ideal. Typical devices exhibit gain and offset figures of around 0.9 V/V and 1.5 Volts, respectively, and suffer from both nonlinearity and spatial nonuniformity.

From previous discussions, it is clear that if each amplifier in the readout device were linear, no significant spatial noise penalty would be incurred as the detector signal is brought to the outside world. Simple gain and offset differences might exist from amplifier to amplifier, but the two-point correction scheme mentioned earlier could totally remove them.

The objective of this section is to explore the amount of nonlinearity associated with the readout device, and to determine the effect of nonuniformity in various material, fabrication and operating point parameters. It will be shown that, with care, the readout nonlinearity, and as a consequence, nonuniformity problems, may be kept well below the corresponding levels expected from the detector array.

Recall that Figure 2.1 shows a schematic representation of the readout electronics. The analysis of this section will assume that this figure adequately represents the CRC-365. By examining the figure carefully, it is clear that the source follower connected to the detector, as well as the common output device, are of the same exact circuit configuration. This analysis will take advantage of that fact.

By deriving a general relationship between the input and output voltage for this basic sub-circuit, the overall transfer function may easily be obtained. The output voltage for the first source follower becomes the input voltage for the output source follower.

Although many popular simulation packages exist for this type of analysis, conventional circuit analysis was favored. By using conventional circuit methods, the effect of various circuit variables may be explicitly determined. A simple simulation package was used only to check the accuracy of the various analytical relationships.

Before beginning the analysis, several properties of the N-MOS transistors used in the readout must be introduced. The surface-channel N-MOS transistor is well understood, and has been covered in detail by many authors. The expressions shown in Eqs. (2.54) through (2.59) were obtained from an excellent text by Streetman (Streetman, 1980) and from a circuit analysis package written by Roden (Roden, 1989).

Both transistors under consideration are operated in the pinch-off, or saturation, region. In this region, the drain-to-source current, I_{DS}, is proportional to the square of the

gate-to-source voltage, V_{GS}. For simplicity, the weak dependence of I_{DS} on the drain-to-source voltage, V_{DS}, was ignored. These ideas are mathematically stated as follows.

$$I_{DS} = 0.5\beta (V_{GS} - V_T)^2 \tag{2.54}$$

The term V_T is the gate-to-source threshold potential, measured in Volts. The proportionality constant β is a function of various material and fabrication parameters. Its value is given by the following relationship.

$$\beta = \bar{\mu}_n \left(\frac{\varepsilon_{ox}}{t_{ox}}\right)\left(\frac{W}{L}\right) \tag{2.55}$$

The term (W/L) is the width-to-channel-length ratio, whose value is nominally determined during photolithographic mask design. The term t_{ox} is the thickness of the gate oxide. This thickness is determined during fabrication, and is typically in the range 0.02 μm to 0.10 μm. The effective surface mobility under saturation is given by $\bar{\mu}_n$. At liquid nitrogen temperatures, this mobility figure will be taken to be 5000 $cm^2\ V^{-1}\ sec^{-1}$ (Alwardi, 1989; Pierret, 1983). The permittivity of the oxide material is given by ε_{ox}. For silicon dioxide, this value is $3.9 \times 8.854 \times 10^{-14}$ Farads per centimeter.

As an example, consider an N-MOS transistor whose (W/L) ratio is 5.0, constructed with a 0.05-μm oxide layer. Its β value is then around 0.002. If the device were operated with a gate-to-source potential 0.075 Volt above the threshold potential, then one would expect around 5 microamps of drain current.

Note that the ratio of permittivity to oxide thickness seen in Eq. (2.55) is actually the oxide capacitance. To simplify notation, the term C_{ox} will be used for this ratio.

$$C_{ox} = \left(\frac{\varepsilon_{ox}}{t_{ox}}\right) \tag{2.56}$$

The threshold voltage, V_T, is a complex function of a number of material and fabrication variables. For integrated MOS devices, the threshold voltage is also a function of substrate-to-source bias. In this analysis, it is that effect which gives rise to nonlinearity. This effect is not usually seen in discrete circuitry, in which the transistor source and substrate are typically shorted together.

It is convenient to write the threshold voltage as the sum of a zero-bias threshold value, V_{TO}, plus a voltage-dependent component.

$$V_T = V_{TO} + \gamma \left[\left(2\phi_F - V_{BS}\right)^{\frac{1}{2}} - \left(2\phi_F\right)^{\frac{1}{2}} \right] \tag{2.57}$$

When written in this way, the bias dependence may be "turned off" later, if desired, by setting γ to zero. This term is sometimes referred to as the body-effect coefficient. The body-effect is the phenomenon mentioned earlier in which the effective turn-on voltage for a MOS transistor varies with source-to-substrate bias. The term ϕ_F is the potential difference in Volts between the Fermi level and the center of the silicon bandgap. For acceptor concentrations in the 10^{15} cm^{-3} range and liquid nitrogen temperatures, Sze (Sze, 1981) shows a value of around 0.55 Volts. The term V_{BS} is the substrate-to-source bias.

The body-effect coefficient, γ, is determined during device fabrication. It is a strong function of the oxide thickness and effective impurity concentration, N_a.

$$\gamma = \frac{\left(2\varepsilon_s\, q\, N_a\right)^{\frac{1}{2}}}{C_{ox}} \tag{2.58}$$

Note that ε_s is the permittivity of silicon, given earlier as 11.8 x 8.854 x 10^{-14} Farads per centimeter.

As an example, consider an N-MOS transistor operating at liquid nitrogen temperature, fabricated with a 0.05 μm thick silicon dioxide gate. If the effective impurity concentration was 5 x 10^{14} cm^{-3}, then the body-effect coefficient would be around 0.2.

If the source-to-substrate voltage was 4.0 Volts, Eq. (2.57) shows that the gate-to-source threshold potential would be raised about 225 millivolts from its zero-bias value.

The initial, or zero-bias threshold potential used for this analysis is as shown.

$$V_{TO} = 2\phi_F + \phi_{ms} + \frac{1}{C_{ox}}\left[2(\varepsilon_s q N_a \phi_F)^{\frac{1}{2}} - Q_i + Q_{ion}\right] \qquad (2.59)$$

New terms appearing in this expression are the gate-to-silicon work function difference, ϕ_{ms}, in Volts, the effective interface charge, Q_i, and the ion-implant dose, Q_{ion}. In this expression, both Q terms are expressed in Coulombs, and are positive in sign.

The gate material for N-MOS transistors is typically either aluminum or polysilicon. In many applications, a polysilicon gate is selected for its low work function difference and process compatibility. For a p^+ polysilicon gate, the work function difference, ϕ_{ms}, is around 0.40 Volts (Sze, 1981).

The effective interface charge is a highly variable function of the crystallographic orientation of the silicon substrate, as well as oxide growth techniques and cleanliness. For this analysis, a value of 5 x 10^{11} positive charges per cm^2 will be used. Its value in Coulombs is around 8 x 10^{-8}.

Ion implantation is used during device fabrication to raise the threshold voltage to the desired positive value. As an example of this, consider an implant dose of around 7 x

10^{10} negative ions per cm^2. If the remaining variables of Eq. (2.59) are the same as in previous examples, then the gate-to-source threshold potential is around 0.70 Volts.

This concludes a description of the N-MOS transistor model used for this analysis. It is now appropriate to consider the exact operation of the source follower subcircuit.

In this analysis, the current source in the output lead shall be considered to be independent of the voltage across it, with value I_{BIAS}. Referring back to Eq. (2.54), the drain-to-source current, I_{DS}, then becomes I_{BIAS}. If the gate is defined to be the circuit input, and the source the circuit output, then the term V_{GS} of Eq. (2.54) may be replaced by $(V_{IN} - V_{OUT})$.

$$I_{DS} = I_{BIAS} \tag{2.60}$$

$$V_{GS} = V_{IN} - V_{OUT} \tag{2.61}$$

Upon making these substitutions into Eq. (2.54), the following expression is obtained.

$$I_{BIAS} = 0.5\beta (V_{IN} - V_{OUT} - V_T)^2 \tag{2.62}$$

Recall that the gate-to-source threshold voltage was given by Eq. (2.57). Note also that the body-to-source bias, V_{BS}, is simply equal to $-(V_{OUT})$. Making these substitutions into Eq. (2.62) yields the following equations.

$$V_{BS} = - V_{OUT} \tag{2.63}$$

$$I_{BIAS} = 0.5\beta \left(V_{IN} - V_{OUT} - V_{TO} - \gamma\left[\left(2\phi_F + V_{OUT}\right)^{\frac{1}{2}} - \left(2\phi_F\right)^{\frac{1}{2}}\right]\right)^2 \tag{2.64}$$

To aid further algebraic manipulation of Eq. (2.64), the following intermediate constants are introduced.

$$X_1 = \left(\frac{I_{BIAS}}{0.5\beta}\right)^{\frac{1}{2}} \tag{2.65}$$

$$X_2 = X_1 + V_{TO} - \gamma\left(2\phi_F\right)^{\frac{1}{2}} \tag{2.66}$$

After a fair amount of algebraic manipulation, and application of the quadratic formula, the following expression for the DC response of the circuit is obtained.

$$V_{OUT} = V_{IN} - \left(X_1 + V_{TO}\right) + \left[\left(\frac{\gamma^2}{2} + \gamma\left(2\phi_F\right)^{\frac{1}{2}}\right) - \frac{\gamma}{2}\left[4\left(V_{IN} - X_2\right) + \gamma^2 + 8\phi_F\right]^{\frac{1}{2}}\right] \tag{2.67}$$

The terms have been arranged to draw attention to the effects of the body-effect coefficient. It is seen that the body effect gives rise to both an offset term and, most importantly, a nonlinear contribution. The nonlinear term is roughly proportional to the square root of the input voltage.

The large-signal gain, A_V, may be found by differentiating V_{OUT} with respect to V_{IN}. The result of this step is shown below.

$$A_V = 1 - \frac{\gamma}{\left[4\left(V_{IN} - X_2\right) + \gamma^2 + 8\phi_F\right]^{\frac{1}{2}}} \tag{2.68}$$

Note that the large-signal gain of the circuit, in absence of the body effect, is 1.0. This is the same result predicted by conventional small-signal analysis, when using the

MOS transistor model described earlier and a constant-current "load resistor." The body effect may thus be thought of in small signal terms as a gain-spoiling effect. The amount of gain reduction is the greatest for large γ values, and when the quiescent point is low.

In large-signal terms, the body effect is best thought of as in input-signal-dependent offset term, which in effect makes the DC transfer function nonlinear, and reduces its slope at all points in the voltage range.

The degree of curvature present in the large-signal response may be found by differentiating the large-signal gain with respect to V_{IN}. The result of this step is shown below.

$$\frac{\partial A_V}{\partial V_{IN}} = \frac{2\gamma}{\left[4 (V_{IN} - X_2) + \gamma^2 + 8\phi_F \right]^{\frac{1}{2}}} \qquad (2.69)$$

By examining this relationship, one may see that the curvature, or degree of nonlinearity, in the response function is greatest for large γ values and low input voltages.

It is now clear that one may simultaneously minimize the nonlinearity, and achieve reasonable large-signal gain values, by fabricating the readout device with a low body-effect coefficient. Since the output source follower is operated at a lower input voltage than the detector source follower its contribution to the overall nonlinearity will be the greatest.

To this point in the discussion, the transient response of the readout device has not been mentioned. In actual operation, the readout is required to rapidly select and output the detector data on a row-by-row and column-by-column basis. A new column is selected about every 400 nanoseconds. A new row is selected about every 63 microseconds.

The specific detector and source follower presented to the output source follower is determined by the row and column access lines shown in Figure 2.1. Upon selection of a

new column bus, the driving source follower in the currently selected row must be able to rapidly slew the gate of the output transistor to its particular output level. In turn, the output device must rapidly slew the output node voltage to its final value.

If the output impedance of the source followers is too high, the source followers will not be able to charge the various distributed capacitances fast enough. Millman (Millman, 1972) shows that the small-signal output impedance of a source follower is related to stray device and load capacitances and to the transconductance, g_m. The transconductance is a small-signal quantity which may be obtained from Eq. (2.54).

$$g_m \equiv \frac{\partial I_{DS}}{\partial V_{GS}} \approx \beta (V_{GS} - V_T) \tag{2.70}$$

For this analysis, this expression may be simplified by again applying Eq. (2.54) and substituting Eq. (2.60). The result is shown below.

$$g_m \approx (2 I_{BIAS} \beta)^{\frac{1}{2}} \tag{2.71}$$

An exact analysis of the stray capacitance and resistance associated with the source-follower transistors, column bus, switching devices, output bus, and output load is impossible without complete knowledge of the device layout and fabrication parameters. It can only be assumed that any such device will be designed so as to permit adequate transient response.

If only the transconductance is considered, the output resistance, R_{OUT}, is given by the following equation.

$$R_{OUT} \approx \frac{1}{g_m} \tag{2.72}$$

Examination of Eqs. (2.71) and (2.72) reveal that the user must be careful to set the column and output bias currents high enough to achieve the design transconductance values. Only then will the full linearity of the source follower chain be realized. It should be noted that next-generation versions of the CRC-365 have added an extra drive transistor at the end of each column bus. This addition lessens the column bias current requirement and further improves transient response (Sato, 1990).

To demonstrate the results of this analysis, Eqs. (2.55), (2.56), (2.58), (2.59), (2.65), (2.66), and (2.67) were evaluated using a personal computer. Table 2.17 summarizes all relevant constants used in the program.

As highlighted in Table 2.17, the only differences between the two transistors are in their (W/L) ratios and I_{BIAS} values. Using the parameters shown, the corresponding β values are 0.0017 and 0.0034 Amps per Volt^2. Both have an initial threshold voltage, V_{TO}, of 0.70 Volt, and a body-effect coefficient of around 0.2. The bias currents chosen were based on output impedance considerations, and on knowledge of the CRC-365.

The equations were first used to predict the output of the detector source follower. That result was then used as the input to the output transistor, and the calculation repeated for V_{OUT} with appropriate changes to β, X_1, and X_2.

Recall that a typical PtSi photodiode of the previous section operates with a 4.0-Volt reset potential. When viewing thermal scenes in the range 0°C to 50°C, the photodiode voltage ranges from about 3.85 Volts at 0°C to 3.25 Volts at 50°C. Analysis of the readout electronics was performed over this voltage range.

Table 2.18 shows the output voltage corresponding to a nominal detector source follower, and the resulting voltage which appears at the final output.

Table 2.17

Constants Used in Nonlinear Readout Device Analysis

Material Properties at 77.3°K

Impurity concentration, N_a	5×10^{14} cm^{-3}
Surface mobility at pinch-off, $\bar{\mu}_n$	5000 cm^2 V^{-1} sec^{-1}
Fermi level, ϕ_F	0.55 Volt
Gate to silicon work function, ϕ_{ms}	0.40 Volt
Silicon permittivity, ε_s	$11.8 \times 8.854 \times 10^{-14}$
Oxide permittivity, ε_{ox}	$3.9 \times 8.854 \times 10^{-14}$

Transistor Fabrication Parameters

Detector source follower (W/L)	5.0
Output source follower (W/L)	10.0
Gate oxide thickness, t_{ox}	0.05 μm
Interface states density, Q_i/q	5×10^{11} cm^{-2}
Ion implant dose, Q_{ion}/q	7.05×10^{10} cm^{-2}

Bias Current Levels

Detector source follower I_{BIAS}	5 microamps
Output source follower I_{BIAS}	300 microamps

Table 2.18

Nonlinear Readout Device Response

Input Voltage	Output Voltage	
	Detector Source Follower	Output Source Follower
3.85	2.895 890	1.664 067
3.75	2.800 392	1.573 702
3.65	2.704 947	1.483 471
3.55	2.609 556	1.393 377
3.45	2.514 223	1.303 429
3.35	2.418 949	1.213 632
3.25	2.323 736	1.123 994

Using the 3.25 and 3.85 Volt inputs, the average gain and offset for the entire range was calculated. With this line as a linearity reference, the worst-case deviation from a perfectly linear transfer function was noted at 3.55 Volts. The results of these calculations are shown in Table 2.19.

The gain and offset associated with each of the two stages is consistent with actual device performance, which will be discussed in greater detail in the next chapter. As expected, the output stage dominates the nonlinearity.

In the previous section, the response of an integrating PtSi photodiode under constant discharge was compared to a photodiode operated at constant bias. It was seen that the mapping between the de-biased response and the constant-bias case was nonlinear. The deviation between the two cases, after accounting for slope and offset differences, was a nonlinearity of around 1.3 percent.

Table 2.19 shows that the nonlinearity associated with the readout device is about ten times smaller than that associated with the detector. This encouraging result suggests that the readout device will not degrade overall performance of the CRC-365 significantly. This observation will be verified in the next section.

In the previous section, the impact of detector nonuniformity was evaluated in the presence of nonlinearity. Consider now the effects of nonuniformity in the readout device. Assuming that a perfectly uniform detector could be obtained, spatial variations in the readout device would be the only source of spatial noise.

In review of the various relationships presented thus far, it is apparent that spatial nonuniformity in the readout may come from many sources. Table 2.20 summarizes the spatially-varying quantities that determine the performance of amplifier (i,j).

Table 2.19

Summary of Nonlinear Readout Device Response

Quantity	Detector Source Follower	Output Source Follower	Total Device
Offset in Volts	-0.775	-1.070	-1.801
Gain	0.954	0.944	0.900
Nonlinearity at mid-scale	0.045%	0.076%	0.121%

Table 2.20

Defining Quantities for Nonlinear Amplifier (i,j)

Width to length ratio, (W/L)

Local impurity concentration, N_a

Initial threshold potential, V_{TO}

Local oxide thickness, t_{ox}

Column bias current, I_{BIAS}

For simplicity, nonuniformity effects were assessed by incrementally perturbing each quantity of Table 2.20, and noting the change in output predicted by the equations presented in this section.

Incremental changes of 10 percent were used, with only one of the entries of Table 2.20 changed at a time. Nominal values were those of Table 2.17. In some cases, the output changes were so small that 0.10 microvolt resolution in the output was required. Table 2.21 shows the result of these studies. The results are arranged in order of increasing effect on the output.

As in the previous section, these response variations were evaluated under the assumption of a single two-point correction spanning the 50°C operating range of the camera. The results shown in Table 2.21 were two-point corrected with the nominal amplifier as a reference. The residual errors at mid-scale were all found to be quite small. These errors are shown in Table 2.22.

Table 2.22, as well as earlier analytical relationships, show that I_{BIAS} variations are indistinguishable from (W/L) variations.

At the 10 percent level, spatial variations in I_{BIAS}, (W/L) and t_{ox} produce essentially a linear scaling of the nominal transfer function. Under two-point correction, these response variations are entirely removed.

Only variations in N_a and initial threshold voltage, V_{TO}, appear to significantly modify the nonlinearity of the nominal transfer function. Fortunately, under two-point correction, their effect is quite small.

If the level of spatial nonuniformity for all five of these quantities is held to 5 percent each, the resulting R.S.S. spatial noise at mid-scale would be about 15 microvolts. Using a gain of 0.9 V/V, and the 26°C signal contrast quoted earlier, this level of spatial nonuniformity corresponds to about 0.0015 rms degrees of equivalent source temperature.

Table 2.21

Nonlinear Amplifier Response Variations

Conditions	Output in Volts		
	V_{IN} = 3.85 V	V_{IN} = 3.55 V	V_{IN} = 3.25 V
Nominal	1.664 066 5	1.393 377 3	1.123 993 5
+10% (W/L)	1.667 269 3	1.396 565 8	1.127 165 5
-10% I_{BIAS}	1.667 598 3	1.396 893 2	1.127 491 2
-10% t_{ox}	1.611 136 1	1.339 444 7	1.069 059 5
-10% N_a	1.681 487 1	1.410 088 3	1.139 966 5
-10% V_{TO}	1.727 397 6	1.456 427 7	1.186 723 3

Table 2.22

Residual Error Under Two-Point Correction with Nonlinear Amplifier Response

Conditions	Corrected Output for V_{IN} = 3.55	Residual Error in μ Volts
Nominal	1.393 377 3	0
+10% (W/L)	1.393 378 4	+1.1
-10% I_{BIAS}	1.393 378 5	+1.2
-10% t_{ox}	1.393 379 3	+2.0
-10% N_a	1.393 393 2	+15.9
-10% V_{TO}	1.393 398 0	+20.7

Recall that for the detector, the residual spatial noise under two-point correction can theoretically be held to about 0.015 degrees. Comparing the detector array to the readout, it appears that the detector will dominate the output spatial noise. The predicted spatial noise level for the detector is ten times greater than that produced by the readout amplifiers, assuming that 5 percent tolerances can be maintained.

Combined Nonlinear Effects

It was shown in the previous section that nonlinearity and spatial nonuniformity in the readout device can be held to negligibly small levels. To further demonstrate that the readout has only a small effect on the overall spatial noise, another simulation study was conducted. This simulation examined the performance of a nonlinear detector array operating in combination with a nonlinear readout device.

In this final analysis of nonlinearity effects, the nonuniform detector outputs of Table 2.14 were processed by the nominal transfer function derived in the previous section. The results of those calculations are shown in Table 2.23.

The data of Table 2.23 were then two-point corrected, using the nominal detector as a reference. The residual error at 26°C was calculated, based on a gain-adjusted signal contrast of around 10.4 millivolts per degree. These results are shown in Table 2.24, along with the residual error figures of Table 2.15. Recall that the results of Table 2.15 were obtained under the assumption of linear amplification.

Examination of the residual error figures shows that the amplifier nonlinearity indeed has little impact on the spatial noise expected from the detector array. Considering any of the entries of the table, the residual error is never more than 0.0015 degree above the result predicted under the assumption of a perfectly linear readout device.

The results of Tables 2.23 and 2.24 constitute an end-to-end simulation of the CRC-365, in the absence of readout nonuniformity. As a final check, several trial

Table 2.23

Detector Nonuniformity Effects with De-Biasing and Nonlinear Amplification

Conditions	Device Output in Volts		
	0°C	26°C	50°C
Nominal	1.669 167	1.484 382	1.136 030
+2% N_a	1.668 573	1.483 452	1.134 656
-2% V_{reset}	1.598 472	1.415 796	1.071 673
+2% A	1.667 580	1.480 670	1.128 735
-2% C_{gate}	1.667 547	1.480 595	1.128 587
+2% C_{lo}	1.667 177	1.478 855	1.124 306
-0.25% ψ_o	1.663 915	1.475 272	1.120 582

Table 2.24

Residual Error Under Two-Point Correction with De-Biasing and Nonlinear Amplification

Conditions	Corrected 26°C Output in Volts	Residual Error, °C	
		Nonlinear Amp.	Linear Amp.
Nominal	1.484 382	0.0000	0.0000
+2% N_a	1.484 316	0.0063	0.0062
-2% V_{reset}	1.484 293	0.0086	0.0072
+2% A	1.484 237	0.0140	0.0133
-2% C_{gate}	1.484 235	0.0142	0.0135
+2% C_{lo}	1.484 222	0.0155	0.0142
-0.25% ψ_o	1.484 064	0.0307	0.0293

calculations were performed, in which the readout was also allowed to be nonuniform. As suspected, these nonuniformities had negligible effect on the overall post-correction spatial noise.

Summary of Nonlinear Effects

In this section, the operation of the CRC-365 imaging device has been analyzed, taking into account detector de-biasing and readout device nonlinearity. The objective of this analysis was to determine the extent to which nonlinearity degrades earlier linear predictions of spatial noise.

It has been shown, through various simulations and engineering calculations, that actual system performance achievable by the device is excellent, when a two-point correction is employed. If manufacturing tolerances for the detector and electronics are held to the levels prescribed, there will be no more than 0.015 degree of post-correction spatial noise over a 50°C operating range.

It has also been shown that for a representative choice of fabrication parameters, the nonuniformity effects of the detector array will dominate those of the readout amplifiers. For this reason, the two-point-corrected test results of the next chapter will be interpreted in terms of detector nonuniformity alone.

The next chapter summarizes the measured performance of an actual CRC-365 device. In addition to reporting the results of routine detector tests, the nonuniformity properties addressed in this chapter will be discussed in detail.

CHAPTER 3

TESTING OF THE HUGHES 256 × 256 HYBRID IMAGING DEVICE

In the preceding chapter, a complete theoretical analysis of the Hughes CRC-365 imaging device was presented. In regard to nonuniformity performance, it was shown that corrected thermal imaging will be degraded only if certain manufacturing tolerances are exceeded during device fabrication. These tolerances are rather loose, suggesting that any device of this design should perform well when corrected by the two-point method.

In this chapter, the results of actual device testing are presented. In addition to nonuniformity tests, a number of other standard detector tests were performed.

To test the CRC-365, it was necessary to build a complete infrared camera and computer interface. The first section of this chapter will discuss the optical, thermal, mechanical, and electrical details of this detector test system.

Following this description of the test system, results of the various detector tests are presented. It is shown that overall performance of the tested device is excellent.

Post-correction spatial noise was well below the temporal noise level. Camera stability was found to be more than adequate, following complete warm-up.

Anomalous effects were noted in the transient response, temporal noise and crosstalk performance.

Description of Infrared Camera

A block diagram of the infrared camera system is shown in Figure 3.1. Key elements of the system include a cryogenic dewar with custom-made internals and infrared optics, custom-made dewar interface electronics, two separate temperature controllers, a

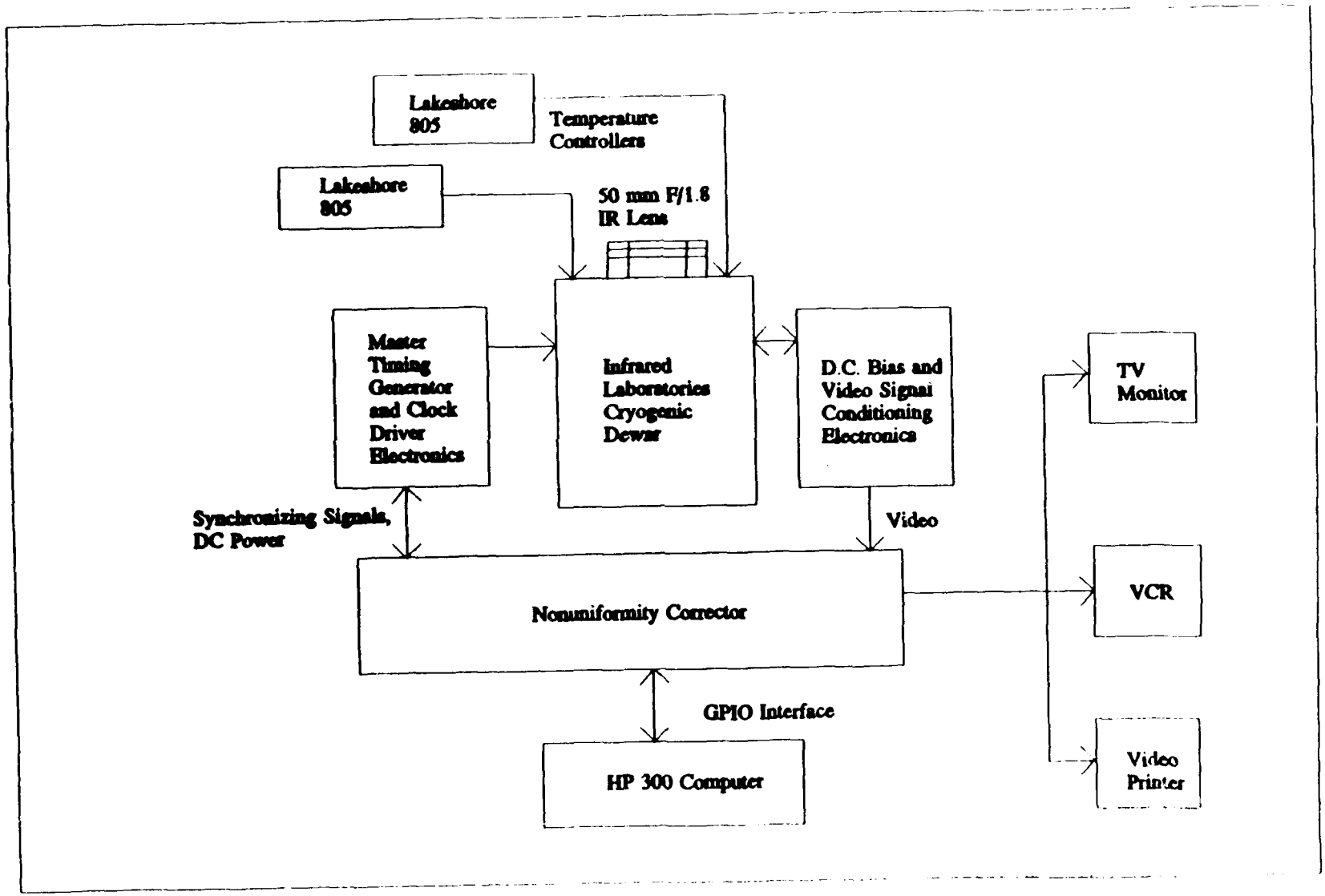

Figure 3.1 Infrared Camera Test System

custom-made nonuniformity corrector with associated video monitoring and recording equipment, and a computer system for data analysis.

In the following sections, a brief description will be given for these subsystems. Optical sources used to perform actual device tests will be described in the individual sections associated with each test.

Cryogenic Dewar

In Chapter 2, the dark current associated with PtSi detectors was discussed. In that discussion, a liquid-nitrogen operating temperature of 77.3°K was assumed. By re-examining Eq. (2.51), it may be seen that temperatures in this range are indeed required to limit the dark current to acceptably low values. Dark charge accumulation must be sufficiently low to prevent degradation of dynamic range and the generation of excessive temporal noise.

An Infrared Laboratories Model HD-3 cryogenic dewar was used to cool the CRC-365 to the desired operating temperature. It was normally operated with its cryogen reservoirs filled with liquid nitrogen. To achieve lower temperatures during dark current tests, a Sargent-Welch mechanical vacuum pump was used to evacuate the air space above the boiling liquid nitrogen. Under these conditions, temperatures as low as 65°K could be obtained.

To achieve precise temperature stabilization, a custom-made cold-finger assembly, electronic temperature sensor, and Lakeshore Cryotronics Model 805 temperature controller were used.

The basic design for the cold finger was obtained from personnel at the National Optical Astronomy Observatories in Tucson, Arizona. This spring-loaded cold-finger was used to establish thermal contact between the bottom of the CRC-365 leadless chip carrier package and the dewar's cold plate. A spring force of around 5 pounds was used. Copper

braid was used to complete the thermal connection between the spring-loaded cold finger and the cold plate. Temperature control of the cold finger and detector package was achieved by varying the amount of electrical power applied to an integral heater resistor.

The temperature of the CRC-365 was sensed by a die-form 1N4148 semiconductor diode. This diode was epoxied to the CRC-365 package and wire-bonded to nearby, unused leads. This delicate task was performed by personnel at the Steward Observatory at the University of Arizona.

When connected to the Lakeshore temperature controller mentioned earlier, this diode was used to provide a readout of the package temperature, as well as serving as feedback for the Lakeshore's control circuits. The control circuits automatically adjust the heater power level to achieve the temperature set on the front panel of the controller.

It was found that peak-to-peak temperature stability could easily be held to 0.04°K. With an operating point of around 1.5 degrees above boiling liquid nitrogen, power input to the heater was around 20 milliwatts. The second channel on the Lakeshore unit was connected to a conventional 1N4148 mounted on the cold plate, giving an indication of its operating temperature.

The CRC-365 leadless chip carrier was securely clamped in a modified Textool (Model 268-4963) socket soldered to its own circuit board. Making a slight change from the schematic of Figure 2.1, a 5000 Ohm resistor was substituted for the current source in each output source-follower output lead. The CRC-365 actually has two video outputs, corresponding to odd- and even-numbered pixels.

Wiring to the circuit board was done with 5 mil Manganin wire and Lakeshore Cryotronics S-1 stainless steel coax. These materials were chosen for their high thermal resistance, to limit the amount of heat conducted to the detector via the lead wiring. All

leads were thermally bonded to the dewar's cold plate with metallic duct tape before being routed to the circuit board.

Bias and ground connections were wired with Manganin leads, whereas the clock inputs and video outputs were wired with coax. The clock leads were routed into the dewar through a dedicated hermetic connector. All remaining detector wiring was routed through a second 32-pin hermetic connector.

Before being routed out of the dewar, each video output line was first buffered by a video amplifier. In addition to providing short-circuit protection for the CRC-365, these amplifiers provide the low drive impedance needed to insure good transient response. The basic design was provided by personnel from Hughes Aircraft. These amplifiers were constructed on their own circuit board, mounted within 5 centimeters of the CRC-365 socket. The amplifiers utilize Siliconix U311 JFETs operated as source followers.

The U311s were hand-selected to minimize amplifier-to-amplifier offset differences. The case of each U311 was fitted to a close-tolerance hole in a temperature-controlled copper heat sink. The case temperature was set to around 3°C above boiling liquid nitrogen. The temperature of this heat sink was controlled by a second Lakeshore Cryotronics temperature controller, operating exactly as described earlier for the cold finger.

Separate six- and ten-pin hermetic connectors were provided for the Lakeshore controllers. Care was taken to maintain ground isolation between the Lakeshore controllers and the CRC-365. No direct ground connection between the dewar body and the CRC-365 was required, although the dewar was securely bonded to the various external electronics enclosures.

Prior to cooling, a Veeco MS-9 leak detection station was used to evacuate the dewar. During routine pump-down, gauge pressure was typically held to around 10^{-5} mm

of mercury for around four hours. Initial cool-down requires about four hours, due to the high thermal resistance of the cold finger. Linde molecular sieve was used inside the dewar as a cryopumping agent.

Even with the extensive wiring required, hold times for the completed dewar assembly were excellent. Operated on its side at one-half its normal cryogen capacity, typical hold times were greater than 24 hours.

The dewar was often kept cold for up to two weeks at a time, refilling the cryogen reservoirs on a daily basis. Slight decreases in the net optical transmission were noted under these circumstances. It is believed that this decrease in transmission was related to the gradual build-up of condensed residual gases and water vapor on the optical bandpass filter. This problem necessitated shorter pump-down and cooling cycles for critical tests.

Infrared Optics

The optical system of the infrared camera was based on knowledge of earlier PtSi camera systems. Major elements of the system include a six-element refractive objective, the dewar entrance window, a cooled aperture stop, a cooled bandpass filter, and cooled baffle assemblies.

The lens chosen was a Diversified Optical 50 mm, F/1.8 unit with around 80 percent effective transmission in the 3.5 μm to 5.0 μm wavelength range. This lens was used for initial camera setup operations, as well as the MRTD tests and other demonstrations of camera performance.

Supplementary ray trace information was provided by Diversified Optical. This analysis included the effects of the particular window chosen for this system, and also showed the suggested placement of optical baffling. This information was used during the mechanical design of various dewar internal supports and surfaces.

The lens was mounted on the front external surface of the dewar, directly over an anti-reflection-coated silicon window. The window was around 50 mm in diameter with a clear aperture of 37 mm and a thickness of 2 mm. Measured effective transmission was around 95 percent.

In normal use the window is subjected to one atmosphere of differential pressure. The thickness was chosen so as to avoid the possibility of fracturing, based on known mechanical properties of silicon. The window was epoxied directly into the dewar entrance aperture. Varian Torr-Seal epoxy was chosen for its excellent mechanical and vacuum sealing properties.

In order to limit the amount of non-imaged infrared light reaching the detector, it was necessary to insert a cooled aperture stop into the optical path, reducing the F-number of the optical system to around F/2.1. This aperture stop was positioned immediately behind the entrance window, and was attached directly to the radiation shield supplied with the dewar. An appropriately-sized clearance hole was added to the radiation shield to allow passage of the optical input.

For this system, this approach yields 100 percent cold-stop efficiency within an image circle extending to the square edges of the detector array. The corners of the array were operated at somewhat less than 100 percent cold-stop efficiency.

A one-inch diameter OCLI (Optical Coating Laboratories, Inc.) bandpass filter was mounted immediately behind the cooled aperture. Two different bandpasses were used, depending on the device test being performed. An opaque disk was used during dark current tests. The thickness of these filters is 1 mm, and they have little effect on the final image plane position.

Completing the optical setup, a cooled baffle was constructed so as to completely enclose the Textool socket, amplifier circuitry, and cold-finger. This cylindrical housing

additionally served as a support structure for the bandpass filter. This baffle, in addition to the radiation shield provided with the dewar, were used to reduce stray infrared radiation to an acceptable minimum.

Dewar Interface Electronics

All dewar interface electronics were constructed from plans provided by the Rome Laboratory. Supplemental information on the electrical characteristics of the CRC-365 were supplied by Hughes Aircraft Company. Modifications were made to the basic plans to include slight timing modifications, temperature-stability enhancements, additional power-supply filtering, and complete aluminum shielding enclosures.

The dewar electronics may be understood most easily by considering each of the four individual circuit cards residing at the dewar. These include a master timing generator board, a clock driver board, a DC bias board, and a video signal conditioning board. Power supplies for these cards are housed in the nonuniformity corrector box, to lessen the coupling of power-line frequency interference to the dewar electronics.

The master timing generator contains a 25.83-Mhz master oscillator from which all system timing is eventually derived. This circuit board provides TTL-compatible timing signals to the clock driver board, video signal conditioning board, and the nonuniformity corrector box. Slight modifications to the original schematics were made, allowing all processes in the nonuniformity corrector to be locked in phase with the dewar electronics. This provides superior rejection of unwanted interference signals during analog-to-digital conversion of the video signals.

The clock driver board acts as a level translator, converting the TTL-level signals from the master timing generator to MOS-compatible clock waveforms. A total of seven AC-coupled clock signals are provided to the CRC-365 from this circuit board, and are routed to the detector via miniature coaxial cables and a dedicated hermetic connector.

These drive waveforms typically are operated between lower and upper rails of 0 and 5 Volts to 7 Volts, respectively.

Bias signals for the CRC-365 are supplied from the DC bias circuit board. This circuit card uses individual operational amplifiers and resistive dividers to supply roughly ten different DC potentials to the imaging device, all of which lie within a range of -1.0 Volts to +5.0 Volts. A single bi-polar voltage reference circuit serves as the master voltage reference for the card.

It was found during initial device testing that some bias signals must be held extremely constant to render the output video free from drift. To identify the most troublesome bias potentials, each was systematically perturbed to determine its effect on the output stability. Two potentials, V_{DDUC} and V_{SS}, were found to have the greatest effect on the overall stability. In these circuits, high-stability OP-07 operational amplifiers were substituted for the usual CA-3140 devices used throughout the design.

The exact bias voltages supplied to the CRC-365 were not found to be critical, with one notable exception. As noted in Chapter 2, the CRC-365 must have sufficient column bias current to deliver its design transient response. This column bias current is controlled by a bias potential named V_{GG}. Proper adjustment of this potential was found only after hours of tedious experimentation and repetition of various device tests.

It cannot be stated too strongly that the profound effect of this bias potential must be thoroughly understood before attempting to finalize device adjustments and testing. Numerous references to this adjustment will be found throughout the remainder of this chapter.

The video signal conditioning board amplifies the video signals as they emerge from the dewar. Following an initial gain of around six, and with an offset adjustment, the video signals are sampled by high-speed sample-and-hold amplifiers. The sample-and-

hold timing is controlled by the master timing generator, as noted earlier. The output of each sample-and-hold amplifier is buffered by a wide-band cable-driving amplifier. Video signals are routed to the nonuniformity correction box over terminated 50-Ohm transmission lines. Taking these cable terminations into account, the net gain through the board is around three.

Best performance was secured by routing all DC power connections and power returns for the various circuit cards through on-board low-pass filters made by Murata Erie. The ground foil on each circuit card was individually grounded to the CRC-365 substrate, with the exception of the digital timing generator. Each circuit card was also securely grounded to its metallic enclosure. The enclosures were securely grounded to the dewar and the nonuniformity-corrector chassis.

Nonuniformity Corrector

The nonuniformity-corrector box design was also provided by the Rome Laboratory. The nonuniformity corrector performs several functions, including supplying power to the dewar interface electronics, digitization of video signals from the dewar interface electronics, processing and display of this video output, and supplying digital video data to the computer system.

The nonuniformity corrector is controlled by a mode switch on its front panel. Using this switch, the user may view either uncorrected video, one-point corrected video, or the one-point correction frame itself. The computer system has continuous access to the same video information appearing on the monochrome video monitor. Video data is digitized to 12-bit resolution.

Controls are also provided for the contrast and brightness of the displayed image. The video output is presented in standard RS-170 format. If desired, the user may capture the video output on a standard VCR, or print out individual images on a video copier.

The one-point correction frame is obtained under a special sub-mode offered by the nonuniformity corrector. By pressing a front panel switch, the nonuniformity corrector calculates an average correction frame. This average is formed by summing 256 sequential frames of video data, during which time the camera is viewing a uniform calibration source. The resulting estimate is almost entirely free of shot noise. It is stored as the new correction frame as long as the power remains on, and is used whenever the mode control calls for one-point-corrected output. This hardware averaging feature is also invaluable in analysis of device performance, offering tremendous time savings over conventional software frame averaging.

Interface to the computer system is established by means of the Hewlett-Packard GPIO scheme. This is a 16-bit parallel duplex interface which can operate at relatively high transfer rates. Each pixel in the detector array is randomly accessible. The user may either capture entire images, or capture small subarrays on a real-time, or sequential-frame basis.

Computer System

The computer selected for the test system was a Hewlett-Packard Model 320. A complete software package was supplied by the Rome Laboratory. This package was written in Pascal, and performs numerous essential functions. New functions were added as needed to the baseline program.

As mentioned earlier, the computer is connected to the nonuniformity corrector box via a GPIO interface. Under software control the user may acquire, analyze, store, and retrieve archival images. Complete images may be captured, or stored or retrieved from disk, in about 15 seconds. Storage options include both hard and soft disk choices. Two complete 12-bit images may be stored on a single mini-floppy diskette.

Analysis options include compensation for dead, hot, and marginally active pixels, generation of pixel-value histograms, calculation of spatial mean and rms values, display of

complete images, with or without contrast enhancements, spatial value probing of displayed images, calculation of single-pixel statistics over time, calculation of one- and two-point corrections, and software frame averaging.

Due to the variety and number of different device tests required, data taking was accomplished through use of the basic analysis functions listed above. Intermediate results were recorded by hand. Manual post-mortem analysis was then performed on these intermediate measurements to obtain the final test result.

Test Methods and Results

The test results of this section represent a comprehensive performance survey of CRC-365 device number IVA193. These tests were performed over roughly a six-month period during which overall performance was slowly refined, most notably through readjustment of bias potential V_{GG}. Recall that V_{GG} determines the bandwidth of the readout device.

Every possible effort has been made to insure that the results presented are self-consistent, and representative of device performance in the field. Table 3.1 shows the bias values applied to the device. Unless noted otherwise, these values were maintained throughout the performance of all tests.

In most cases, final interpretation of various test results is provided. In-depth analysis of the nonuniformity tests is deferred until Chapter 4. A quick summary of results is provided at the end of this chapter.

Measurement of Signal Channel Transfer Functions

To verify proper imager and video preamplifier operation, several oscilloscope measurements were made on the video output from the dewar. Additionally, the overall system gain from the detectors through the analog-to-digital conversion process was

Table 3.1

Nominal Biasing Used During Imaging Device Tests

DC Bias Potentials

CRC-365 Pin Designation	Function	Value in Volts
$V_{DDOUT1,DDOUT2}$	Output source-follower drains	5.00
$V_{DEND,FDEND}$	Shift register monitor S.F. drains	5.00
V_{DDUC}	V_{DD} for readout	3.75
V_{GG}	Column current source control gate	0.85
V_{SUB}	Substrate connection	0.00
V_{DET}	PtSi detector common anode	0.00
V_{SS}	V_{SS} for readout	-0.18
V_{3S}	V_{SS} for slow-axis shift register	-0.20
V_{3F}	V_{SS} for fast-axis shift register	-0.20
$V_{OUT1-LOAD}$	Odd output channel load resistor	-0.50
$V_{OUT2-LOAD}$	Even output channel load resistor	-0.50

Clock Potentials

CRC-365 Pin Designation	Function	Value in Volts Low	High
$\phi_{1F,2F}$	Fast-axis clock lines	0.07	6.40
$\phi_{1S,2S}$	Slow-axis clock lines	-0.01	5.10
ϕ_{SYNCHS}	Slow-axis shift register synch. input	0.25	5.20
ϕ_{SYNCHF}	Fast-axis shift register synch. input	0.07	5.00
ϕ_{RST}	Reset clock line	0.35	5.40

measured. This quantity was needed later in calculation of the detector sense node capacitance.

The Hughes literature mentioned earlier, plus various engineering calculations presented in Chapter 2, provided the necessary background for these tests. Both video outputs were examined, and were found to perform properly.

Gain and Offset of JFET Preamplifiers. Recall that each output source follower of the CRC-365 is connected to a similarly wired JFET source follower, in close proximity to the imager. These JFETs are directly connected to the terminal labeled V_{OUT} on Figure 2.1. To verify their operation, they were individually analyzed using oscilloscope measurements. A Tektronix model 2445A oscilloscope with cursor voltage readout was used to measure output signal levels to within one millivolt.

During the vertical reset period associated with the imager, it is possible to measure the properties of the JFET amplifiers alone, without direct access to the JFET gates. During this time interval, the CRC-365 outputs are completely shut off. The JFET gate potentials are identically equal to externally supplied load resistor potentials, which may easily be measured with a voltmeter.

By slightly varying the CRC-365 load resistor potentials, one may observe the changes in the dewar output video, and infer the gain and offset of the JFET amplifiers. With this method, no additional dewar wiring is needed to perform the measurement.

The results of this study are shown in Eqs. (3.1) and (3.2). These expressions show the DC transfer functions corresponding to the amplifiers connected to the even and odd CRC-365 video outputs. Input and output quantities are expressed in Volts.

$$V_{JFET2} = (0.945) \times (\text{Even CRC-365 Output Channel}) + 0.537 \qquad (3.1)$$

$$V_{JFET1} = (0.940) \times (\text{Odd CRC-365 Output Channel}) + 0.556 \qquad (3.2)$$

As noted earlier, these devices were hand-picked for close offset matching. The selection process was completed at room temperature, where the devices were matched to within 15 millivolts. These results show that the match is still within about 20 millivolts at cryogenic operating temperatures. Recall that these amplifiers are stabilized at a temperature of about 80°K.

The gain values shown are consistent with those predicted by conventional circuit analysis. For a FET source-follower operated with a resistive load R_L, the gain is given by Eq. (3.3).

$$A_v = (1 + 1/(g_m R_L))^{-1} \qquad (3.3)$$

These amplifiers utilize a load resistance of 1000 Ohms. The transconductance, g_m, of the U311 JFETs is around 0.02 Mhos. Using these values in Eq. (3.3), one would expect a gain value of 0.952. The experimentally measured values are both within 1.5 percent of this theoretical value. Additionally, the two amplifiers are gain-matched to within 0.5 percent.

The results of this section verify that the cryogenic JFET video amplifiers used to buffer the CRC-365 outputs operate in close agreement with simple theoretical predictions, and are nearly identically matched when operated at cryogenic temperatures. The results of Eqs. (3.1) and (3.2) will be used in subsequent calculations of the imager's properties.

Gain and Offset of the Imaging Device. Recall that in Chapter 2 engineering calculations were performed to predict the gain and offset of the readout device. To

provide a quick check on device performance, these quantities were measured, using an oscilloscope technique similar to that of the previous section.

Refer again to Figure 2.1. By varying the PtSi reset potential slightly, and observing the dewar output, one may estimate the gain and offset associated with the CRC-365. Since observations are made at the output of the JFET source followers, their transfer functions must be taken into account in expressing the final results. These transfer functions were discussed in the previous section.

The video output waveform was observed during its horizontal reset period, during which time the output is essentially a gain and offset adjusted version of the reset potential. By varying the reset potential over a 250 millivolt range, in 50 millivolt steps, the following transfer functions were obtained.

$$V_{JFET2} = 0.710 \times (V_{RESET}) - 0.962 \tag{3.4}$$

$$V_{JFET1} = 0.713 \times (V_{RESET}) - 0.943 \tag{3.5}$$

Now by equating Eq. (3.1) to Eq. (3.4), and similarly equating Eq. (3.2) to Eq. (3.5), one may algebraically solve for the CRC-365 transfer functions. The result of this step is shown below.

$$\text{Even CRC-365 Output Channel} = 0.751 \times (V_{RESET}) - 1.586 \tag{3.6}$$

$$\text{Odd CRC-365 Output Channel} = 0.758 \times (V_{RESET}) - 1.595 \tag{3.7}$$

Examining the offset terms first, it is seen that the measured offset values agree fairly well with the theoretically predicted value of -1.800 Volts. Differences are less than 250 millivolts. Note also that the offset matching between the two CRC-365 output channels is extremely tight. The odd and even pixels, on average, are brought out of the device with less than 10 millivolts of offset difference.

The gain terms are somewhat lower than expected. Recall that the analysis of Chapter 2 assumed the use of a current source in the output leads of the CRC-365. In practice, since load resistors have been substituted for these current sources, the gain has been reduced from the theoretically predicted value of 0.900.

By applying Eq. (3.3), a revised theoretical gain estimate may be made. Using the R_L value of 5000 Ohms mentioned earlier, and an estimated transconductance, g_m, of 0.0015 Mhos, an output source-follower gain of 0.88 is predicted. Combining this with the detector source-follower gain of Table 2.18, one obtains a new net gain estimate of 0.95 x 0.88, or 0.84.

The gain values shown in Eqs. (3.6) and (3.7) are within about 10 percent of the revised theoretical gain estimate. Note also that the gain mismatch between CRC-365 output channels is less than 1 percent.

The results of this section support the analysis given in Chapter 2, and demonstrate that the device under test is worthy of further testing. These results also show that no gross misadjustments of the device operating potentials have been made.

System Gain. In review of the entire signal path, recall that the CRC-365 amplifies the output of each PtSi detector, with gain and offset values as given in Eqs. (3.6) and (3.7). After leaving the imaging device, the signal is amplified by the JFET source followers described by Eqs. (3.1) and (3.2). After emerging from the dewar, the

video outputs are amplified and offset one more time by the video signal conditioning circuitry, which in turn is connected to the analog-to-digital converters.

To verify proper operation of the video signal conditioning and analog-to-conversion circuitry, the gain of the entire system was measured. In this test, the camera was flood illuminated by an Electro Optical Industries Model 1805 blackbody. The blackbody was maintained at 30°C.

As in the previous section, V_{RESET} was varied over a limited range. Minor changes in photoresponse with detector bias were ignored. For each V_{RESET} value, the average output value for the central portion of the array was calculated, using the software analysis program described earlier.

By fitting a line to the input and output data, the system gain in analog-to-digital units (ADU) per Volt was found. These calculations were performed for both the even and odd signal channels. These results are shown below.

$$\text{Even Channel System Gain} = 3547 \text{ ADU / Volt} \tag{3.8}$$

$$\text{Odd Channel System Gain} = 3565 \text{ ADU / Volt} \tag{3.9}$$

The analog-to-digital converters operate with a scale factor of 0.00061 Volts per ADU. Using this fact, and the results of Eqs. (3.4) and (3.8), one may calculate the gain of the odd channel of the video conditioning board. This value is 3.05, which is in close agreement with the design value of 3.00. Similarly, the gain of the even video conditioning board channel was also found to be 3.05. There is no appreciable mismatch between the two video signal conditioning channels.

The results of this section verify proper operation of the video signal conditioning circuitry. Equations (3.8) and (3.9) will be used in a later section to calculate the average sense node capacitance.

Measurement of Dark Current

An early measurement of device dark current is often used to verify proper device cooling, and serves as a screening test of device performance.

The device under test was subjected to several dark current tests. It was discovered that although it has many defective detectors, they are largely concentrated in areas outside the central portion of the detector array.

In the central region of the array, nearly all detectors exhibit low dark current when cooled to liquid nitrogen temperatures or lower. This central region was used almost exclusively for the remaining tests described in this chapter.

Defective Pixel Map. As mentioned in the introduction, the device under test has a large number of dark current defects and other defects which must be accounted for. These defects will be discussed in this section, as well as the software compensation scheme which was used to eliminate their effect on test results.

To perform the dark current tests described in this and subsequent sections, a metal disk was used to block off the optical path inside the dewar.

When operated in this way, the camera output is as shown in Figure 3.2. This picture was obtained from a thermal video copier attached to the RS-170 output. The picture reveals several interesting features related to the fabrication of the imager.

Familiar (x,y) notation will be used to describe detector positions. Note that detector (1,1) is in the lower right corner of the picture. The bright dots and the large

(256,256) (1,256)

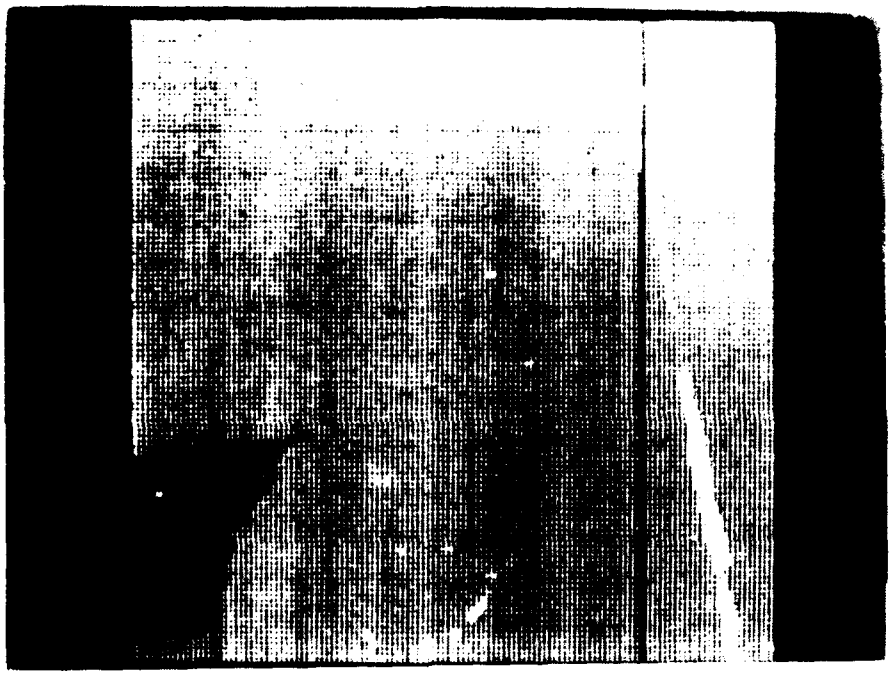

(256,1) (1,1)

Figure 3.2 Dark current at 79°K

streak running diagonally across the array are dark current defects. The streak extends roughly from pixel (15,1) to pixel (49,178).

These defective detectors produce full-scale outputs when digitized. There are approximately 200 such defective detectors when the device is operating near liquid nitrogen temperatures. Some can be brought on scale by further cooling, whereas the majority cannot.

The dark line centered on column 54 is believed to be the result of defective columns in the readout electronics. Detector outputs from this region respond only slightly to optical and thermal stimulation.

The irregular-shaped region in the lower left corner terminates near detector (200,80). The origin of this defect is unknown, but it is believed to be in the detector array. Both optical and thermal stimulation produce stronger-than-average responses from this region.

The high-frequency grid pattern running through the picture comes from slight periodic variations in the readout electronics. This effect will be discussed in greater detail in Chapter 4.

Due to the rather large number of defects appearing in the output, an analysis region in the center of the detector array was selected. The square region defined by coordinates (61,61) and (196,196) was found to be almost defect-free. The detectors in this area comprise roughly 30 percent of the total array. This area was used almost exclusively for the computations discussed throughout this chapter.

Six detector outputs in this central region were found to be defective. To eliminate computational errors associated with these detectors, a simple software compensation scheme was used. Defective outputs were simply replaced by the output of an adjacent, properly operating detector. These substitutions are as shown. From left to right, the

equations represent the coordinates of the properly operating detector, followed by two defective outputs which are read out immediately thereafter.

$$(95,180) = (97,180) = (99,180) \tag{3.10}$$

$$(97,116) = (99,116) = (101,116) \tag{3.11}$$

$$(112,149) = (114,149) = (116,149) \tag{3.12}$$

It is significant that the defective outputs occur in pairs. It appears that when either the odd or even output bus of the CRC-365 is subjected to large voltage changes, it takes more than one pixel period for the bus to be discharged to nominal operating levels. This unexpected observation is evidence of a slew-rate limitation in the CRC-365 readout electronics. This effect has the potential for excessively smoothing high-spatial-frequency details in high-contrast images.

Dark Current Versus Temperature. The array-wide dark current was measured by means of an electrometer inserted in series with the common anode connection of the PtSi detector array. The temperature of the CRC-365 package was varied between 70°K and 90°K, with one degree steps between data points.

The Lakeshore controller mentioned earlier was used to stabilize the temperature during data acquisition. To obtain package temperatures in the lower half of the range, the dewar cold plate temperature was reduced to roughly 65°K by evacuating the cryogen reservoir.

At each temperature setting, the electrometer current was recorded, and the computer acquisition system was used to measure the spatial mean of the entire array and

central subarray described earlier. At the conclusion of data taking, a fairly simple algebraic method was used to reduce this data.

The procedure of recording both the array mean and the central mean was used to verify that the defective pixels mentioned earlier do not significantly alter the final results. In this particular test, it was determined that the excess current passed by the defective pixels has little effect.

This basic test was repeated for a number of different bias conditions, all of which changed the device power dissipation slightly. No dramatic change in dark current was noted. The results of these tests are shown in Figure 3.3. The dark current is expressed as electrons per detector per integration period. The data represents the spatially averaged dark current in the central region of the detector array.

In similar testing at Hughes Aircraft Company, Gates (Gates, 1988) observed 26,000 electrons at 78°K. Figure 3.3 shows that the device under test works slightly better, achieving 26,000 electrons at 80°K.

Under the standard bias conditions of Figure 3.1, and with the boiling liquid nitrogen at standard temperature and pressure, the imager and cold finger can be regulated to temperatures as low as 79°K. Figure 3.3 shows that the dark charge at this temperature averages about 20,000 electrons per pixel per integration period. Note that if the device had a saturation limit of around one million electrons, the dark charge would consume only 2 percent of this working range.

Note also that this level of dark charge is roughly one-tenth of the 26°C background signal which one would expect across the detector. Recall that Table 2.2 indicates a hypothetical 26°C photoresponse of 195,756 electrons. The shot noise on the photosignal alone is about 440 rms electrons. The shot noise on the photosignal plus the dark charge is

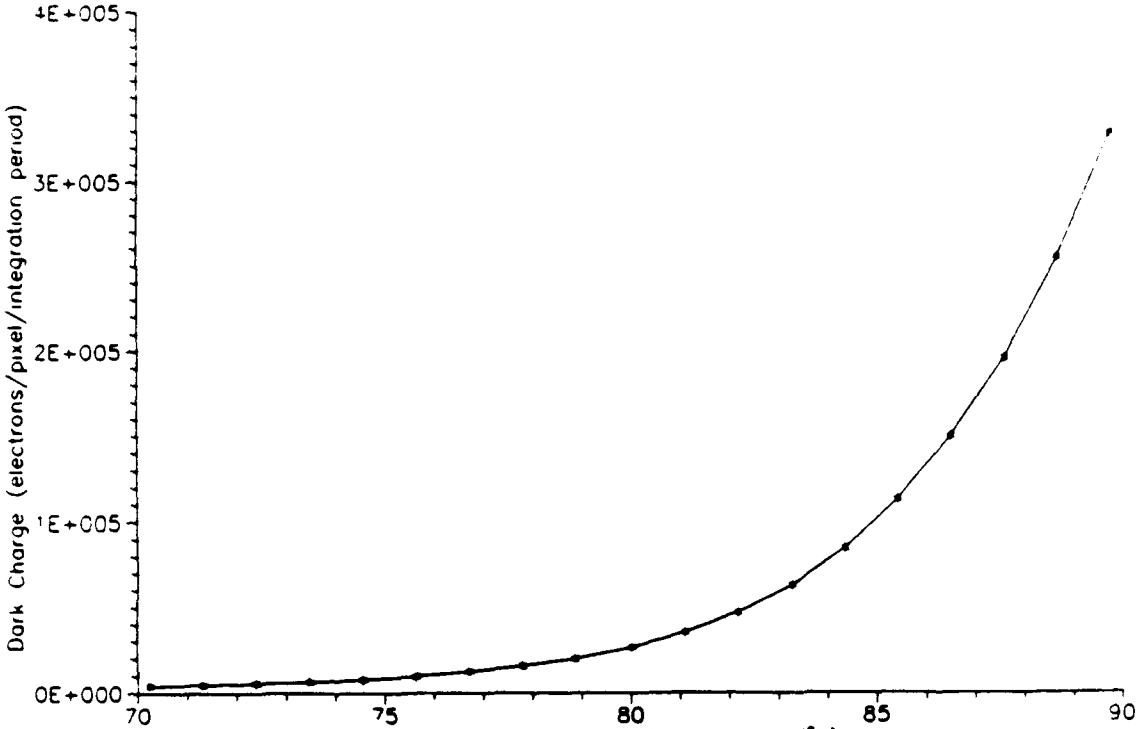

Figure 3.3
Dark Current Versus Temperature

about 465 rms electrons. The dark charge thus raises the temporal noise level by only 5 percent.

By these measures, the dark current performance of the device is excellent. Figure 3.3 shows that further improvements are only slight as the temperature is reduced below 79°K. For this reason, all routine detector testing was done near this temperature. As noted earlier, the pumping procedure is not required at this temperature.

Richardson's analysis was used to further study the data of Figure 3.3. This method plots the natural log of (J_D/T^2) versus 1/T, where T is the detector temperature. The term J_D is the dark current density, in Amps per cm^2. It may be obtained directly from Figure 3.3 by taking into account the number of pixels in the array, the area per pixel, the electronic charge, and the integration time.

Assuming 2^{16} detectors, an active area of $(28\ \mu m)^2$, and 60 frames per second, the conversion factor between electrons and current density is 1.2262×10^{-12}. As an example, consider the 20,000 electron figure discussed earlier. Applying the conversion factor, this corresponds to about 25 nanoamps per cm^2.

The Richardson's plot for this data is shown in Figure 3.4. Notice that above about 79°K, the plot appears as a straight line. This indicates that the dark current is dominated by thermal generation of carriers. Below this point, the plot has a tail, indicating the presence of other dominating leakage terms.

By reexamining Eq. (2.51), it is seen that the Richardson's plot has a y-axis intercept equal to the log of the Richardson's constant, and a slope proportional to the thermal barrier height. The proportionality constant between the slope and the barrier height is -(q/k), where q is the electronic charge and k is Boltzman's constant.

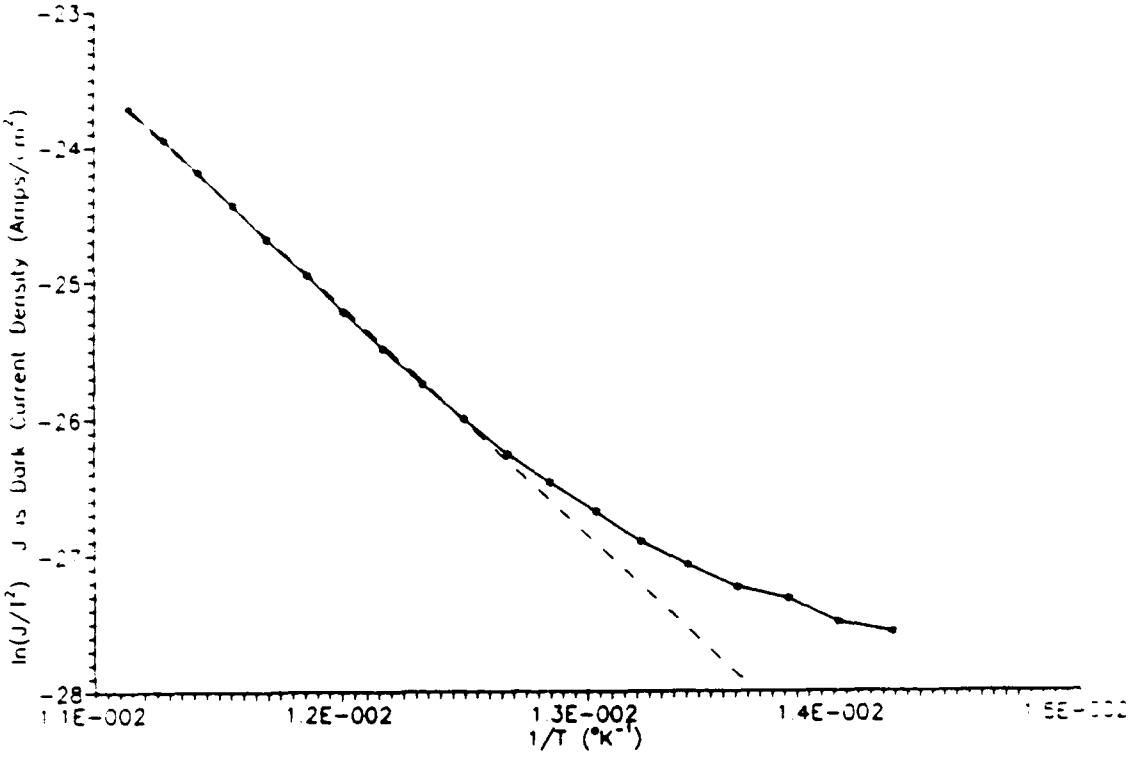

Figure 3.4
Richardson's Analysis of Dark Current

For the plot shown, the Richardson's constant and barrier height were found by using a least-squares fit to the data above 79°K. Unfortunately, the results were considerably different than one would expect.

The Richardson's constant, A*, was found to be 0.0065 Amps per cm^2, whereas the theoretical value is 32 Amps per cm^2. The experimentally determined barrier height was around 0.145 eV, whereas a value of around 0.19 to 0.20 eV was expected. As pointed out by Shepherd (Shepherd, 1991), errors of this magnitude can sometimes be explained by the presence of excessive leakage current. Some improvement in these results was obtained by subtracting a temperature-independent leakage term of 5 nanoamps per cm^2 from the observed dark current density values. Under these conditions, Richardson's analysis yielded an A* value of .02 Amps per cm^2 and a barrier height of .153 eV.

Trial calculations show that these errors might be accounted for by slope errors in the temperature sensor. The slope calibration factor for the temperature sensing diode was determined by using widely spaced calibration points at room temperature and at liquid-nitrogen temperature. It is suspected that a better calibration of the sensor would resolve the problem in this plot.

Another calculation of the thermal barrier height was performed by assuming an emission constant of 32 Amps per cm^2. In this calculation, the current density at 79°K was used. Since this data point is near the calibration point for the sensor, and since it lies on the straight portion of Figure 3.3, it may be used to estimate the barrier height. The calculation is performed by first solving Eq. (2.51) for the barrier height, ψ_{th} (V_R). Upon substituting the current density at 79°K, shown in Figure 3.4, a barrier height of 0.202 eV is obtained. This is close to the value originally expected of this measurement.

Dark Current Versus Detector Bias. In the previous section, the behavior of the dark current at nominal detector bias was investigated. Consider now the effects of

reduced detector bias. Normally, the detector is initially reset to 3.75 Volts. Several dark current versus temperature runs were made at lower bias values.

In all cases, dark current decreased with reductions in the bias. The lowest bias value used was around 1.35 Volts. The dark current profile under these conditions is shown in Figure 3.5. The data of Figure 3.3 have been included for reference.

No anomalous behavior was noted throughout the range of initial bias values tested. The thermal barrier heights for 2.5-Volt and 1.35-Volt bias values were estimated to be 0.210 eV and 0.219 eV respectively.

Dark Current Nonuniformity. Spatial nonuniformity of the dark current was measured as a function of temperature. In this test, the device was first cooled to around 70°K. The frame averaging feature of the nonuniformity corrector was used to form a reference frame at this temperature. This reference frame was stored in the computer and used at all subsequent temperatures to compute the dark current nonuniformity. Recall that the frame-averaging procedure reduces the shot noise in the data. Only spatial variations remain in the data frames.

Data was taken at one-degree intervals between 70°K and 85°K. At each temperature setting, the nonuniformity corrector was used to form a new average frame. To compute the nonuniformity, the reference frame stored in memory was first subtracted from these average frames. Statistics were then computed on these difference frames.

Recall that Figure 3.2 revealed the presence of a periodic variation in the readout device electronics. To eliminate the effect of this pattern on the test data, statistics were computed in a special way.

Under the bias conditions of Table 3.1, the grid pattern associated with the readout was found to have a 4 pixel by 2 pixel repetition sequence in the x and y directions,

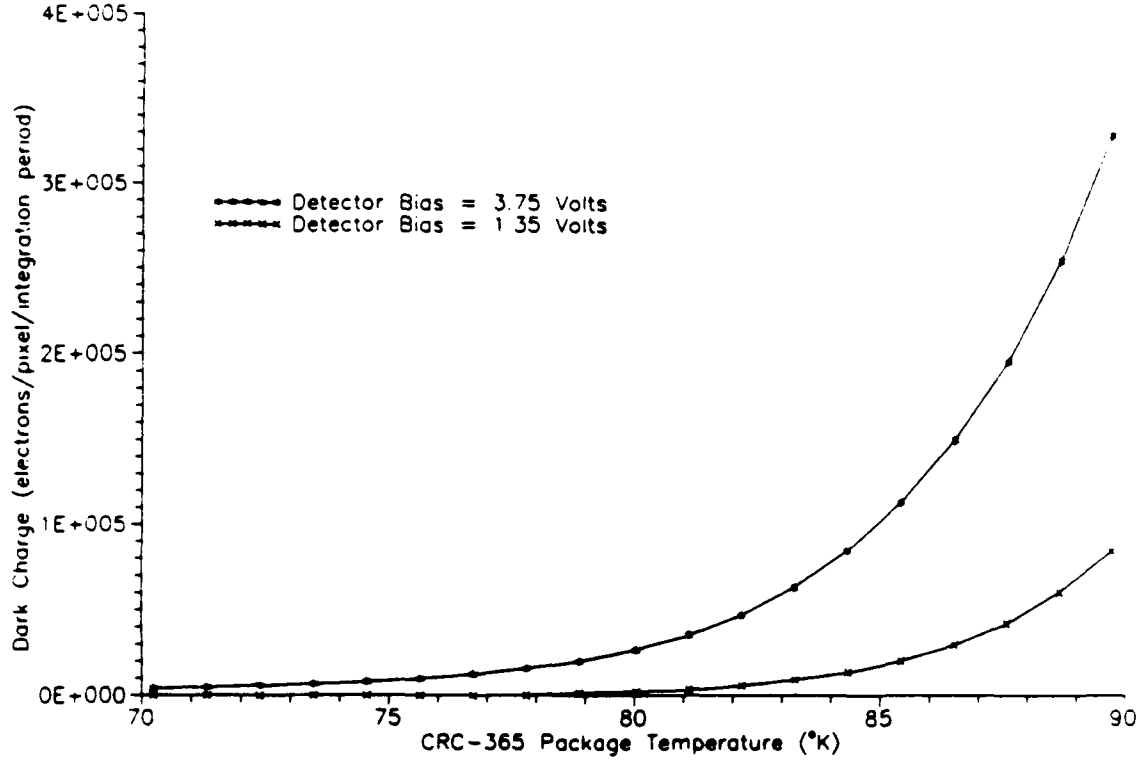

Figure 3.5
Dark Current Versus Temperature For 3.75-Volt and 1.35-Volt Detector Bias

respectively. To compute the dark current nonuniformity, sister pixels within each 4 by 2 group were examined.

The rms nonuniformity for each such grouping of pixels was calculated. To express the final result, the rms variation in dark current was divided by the mean dark current. The results of this study are shown in Table 3.2. Results are shown for the best and worst pixel groups.

Table 3.2 reveals an interesting phenomenon. Recall that the Richardson's plot discussed earlier revealed the existence of non-thermionic leakage effects at lower temperatures. At these low temperatures, spatial variations in the dark current can be quite large. Nonuniformity levels as high as 13 percent are shown in the table. Perhaps some of this nonuniformity is attributable to temperature-related effects in the readout electronics.

As the device temperature is raised, thermionic generation eventually dominates the net dark current. At these higher temperatures, spatial variations in dark current of around three percent are typical. This level of nonuniformity is consistent with that reported for other PtSi imaging devices (Shepherd, 1988).

The preceding sections show that the dark current performance of the tested device is quite adequate for normal thermal imaging tasks. One anomalous effect was discovered in the area of transient response. It was found that the tested device has difficulty tracking the large signal changes associated with dark-current defects.

Measurement of Schottky Barrier Height

In this series of tests, the Schottky barrier height was measured as a function of detector bias. Both the intrinsic barrier height, ψ_o, and the detector impurity concentration, N_a, were found. The value found for ψ_o was close to previously published values. The correlation of barrier height with bias was excellent. The value found for N_a was very close to the value anticipated.

Table 3.2

Dark Current Nonuniformity

Temperature in °K	Worst Pixel Group	Best Pixel Group
70.2	N/A	N/A
72.4	13.4%	11.8%
74.6	8.0%	6.4%
76.7	6.0%	4.8%
78.9	4.8%	3.8%
81.1	3.9%	3.2%
83.3	3.3%	2.8%
85.4	2.8%	2.3%

A modified version of the Fowler method was used to determine the barrier height for a number of bias settings. The impurity concentration was found by plotting these barrier height findings against the applied bias voltage.

The Fowler method may be understood by rewriting the quantum-efficiency expression of Eq. (2.2), replacing the constant 1.24 by hc/q, and replacing $\eta(\lambda)$ by Y. If we choose to work in units of electron-Volts, the electronic charge, q, may be eliminated. The ratio c/λ may be replace by the frequency, v. The result of these changes is shown below.

$$Y = \frac{C_1}{h\nu} (h\nu - \psi_{ms})^2 \tag{3.13}$$

This equation may be rearranged to the form used in the Fowler method.

$$(Y\, h\nu)^{\frac{1}{2}} = (C_1)^{\frac{1}{2}} (h\nu - \psi_{ms}) \tag{3.14}$$

In practice, a monochromatic source is used to measure the quantum efficiency, Y, as a function of wavelength. The quantity on the left is plotted as a function of hv. The slope of the resulting line is the square root of the Schottky quantum yield, or C_1, and the x-axis intercept is the Schottky barrier height, ψ_{ms}

This method requires exact knowledge of the irradiance placed on the detector under test, as a function of wavelength. The optical source used for the test must be calibrated using a reference detector.

If one is willing to sacrifice the measurement of C_1, absolute calibration of the source is not required. One may measure the relative output of the source, and then the relative response of the detector under test, as a function of wavelength.

These results may be used to produce a modified Fowler plot. In this plot, only the barrier height result is used. This is the way the tests of this section were performed. The C_1 coefficient was measured by another method, described in the next section.

Figure 3.6 shows the block diagram of the test setup used to perform these measurements, including the monochromatic source mentioned earlier. The source consists of an electrically heated ceramic rod, called a glow-bar, a spherical mirror, and a Perkin-Elmer Model 98 monochromator. The monochromator uses a sodium chloride (NaCl) prism to disperse the infrared light provided by the glow-bar. Adequate spectral resolution was obtained by setting the entrance and exit slits to 250 μm.

The figure additionally illustrates the equipment used to characterize the relative spectral output of the source. The light chopper, thermopile detector, and lock-in amplifier constitute the detection system. The infrared filter was used during calibration of the wavelength drive mechanism.

The wavelength drive was calibrated first. Several infrared bandpass filters were measured on a Beckman IR-20 spectrophotometer, noting their exact cut-on and cut-off wavelengths. These filters were then placed in the optical path of the monochromator. By observing the output of the lock-in amplifier, the filter edges were easily located. A chart was constructed, showing the connection between the markings on the Model 98's wavelength control and the center wavelength of its bandpass.

After wavelength calibration, the relative output of the source was recorded as a function of wavelength. To convert to photon units, the readings were scaled by the wavelength at which each data point was taken. In testing the PtSi detectors, the output of the monochromator must pass through the dewar window and a bandpass filter. For this reason, the readings were further adjusted, accounting for the known transmission properties of these components.

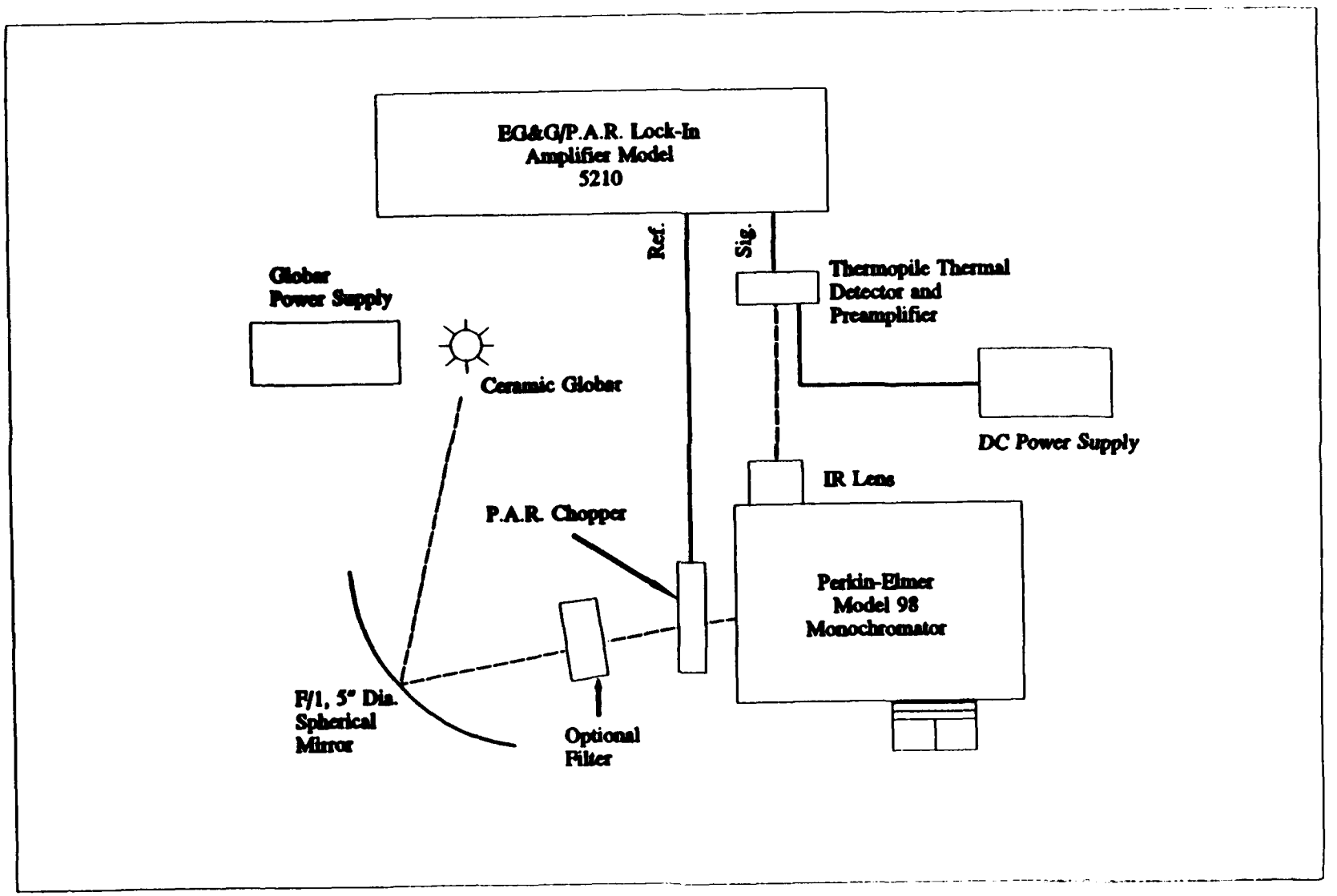

Figure 3.6 Schottky Barrier Height Calibration Set-up

After completing the source characterization, the CRC-365 was tested. For each wavelength used in the source characterization, the relative output of the camera was recorded. This was done by taking the difference between two frames of data. The first frame was taken with the glow-bar illumination to the monochromator blocked. The second frame was captured a short time later, after unblocking the source. The spatial average of the difference frame was recorded at each wavelength.

After recording a full set of data in the 3.4 to 4.9 μm wavelength range, it was divided by the source correction factors described earlier, as well as an arbitrary scaling constant. These values were used as the Y values for the Fowler plot. The procedure was repeated several times, generating data for six detector bias values in the range 1.25 Volts to 3.75 Volts.

The Fowler plot for the 3.75-Volt bias value is shown in Figure 3.7. The plot shows that the Schottky barrier height is around 0.236 eV. This value corresponds to a detector cut-off wavelength of about 5.3 μm.

Recall that Eq. (2.48) gives the relationship between Schottky barrier height and applied bias. By plotting the measured barrier heights versus the fourth root of the bias voltage, one may determine the intrinsic barrier height, ψ_o and the detector impurity concentration, N_a. The y intercept is equal to ψ_o, whereas the slope is proportional to $N_a^{1/4}$. The proportionality constant is easily discerned from Eq. (2.48). Its value is -2.6 x 10^{-6}. This plot is shown in Figure 3.8.

When extrapolated back to the y-axis, the plot yields a ψ_o value of 0.2498 eV. A similar result was obtained by Mooney (Mooney, 1989b). In his testing, ψ_o was found to be 0.2447 eV. The least-squares fit to these data points predicts a barrier height of 0.2362 eV when operating with a bias of 3.75 Volts. This value will be used for a number of

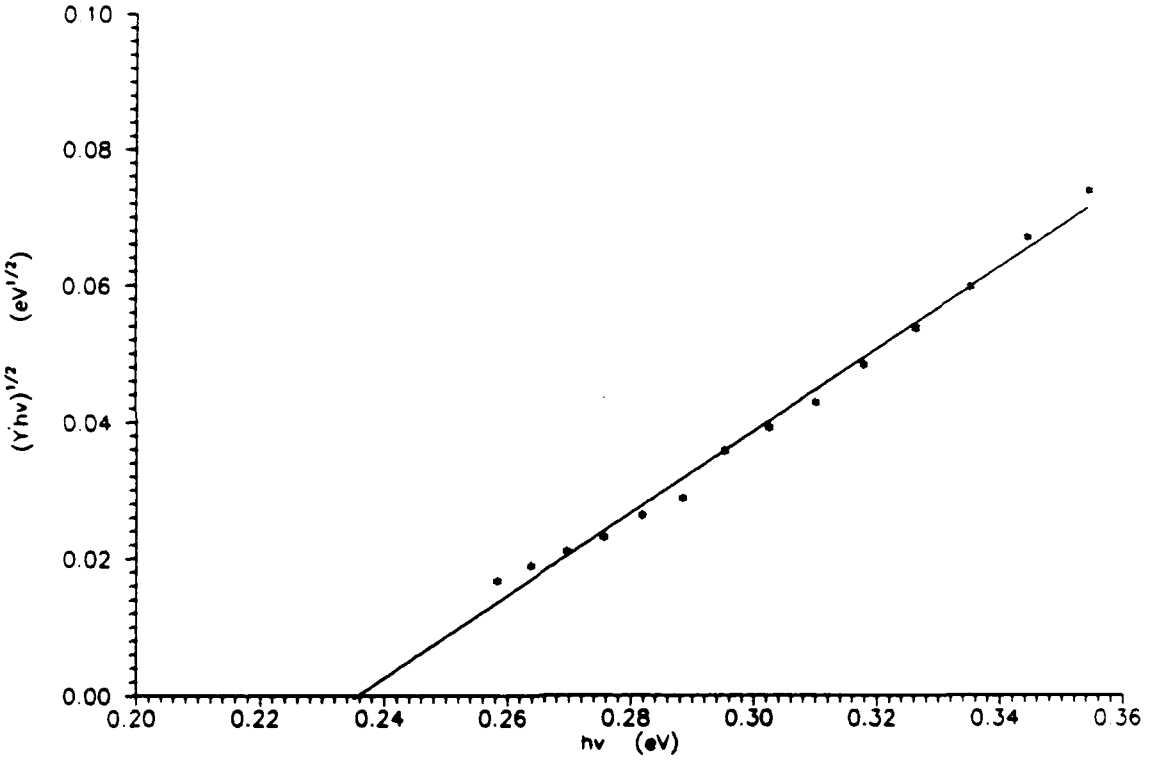

Figure 3.7
Modified Fowler Plot For 3.75–Volt Initial Bias

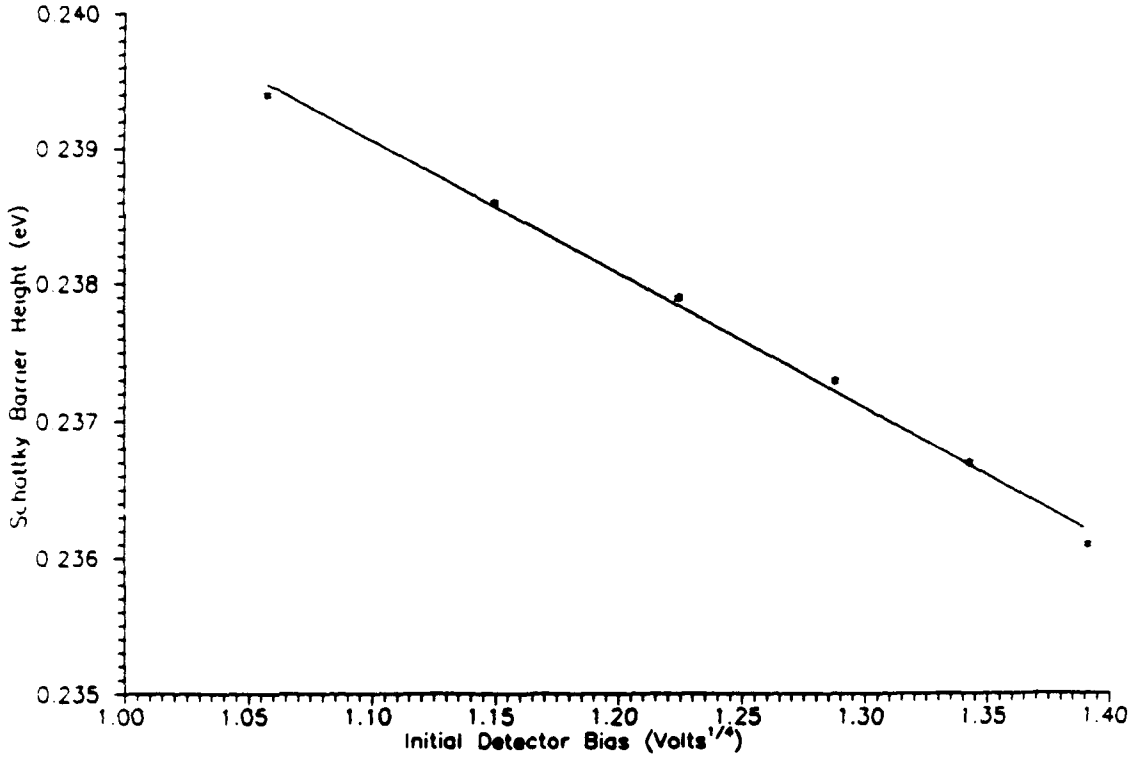

Figure 3.8
Schottky Barrier Height Versus Bias

calculations in following sections. Note that this barrier height is considerably higher than the 0.22 eV value used in the theoretical calculations of Chapter 2.

The impurity concentration was found to be 2 x 10^{14} per cubic centimeter. Typically, these detectors are fabricated with a wafer whose resistivity is around 20 Ohm-centimeters at room temperature (Edwards, 1990). This corresponds to about 10^{15} fully ionized acceptors per cubic centimeter. Sze (Sze, 1981) shows that when cooled to liquid nitrogen temperature, the effective carrier concentration of such a wafer drops to about 3 x 10^{14}.

The close agreement between measured and predicted values for the acceptor concentration, as well as the excellent linearity of the data points in the plots, strongly support the validity of these barrier height measurements.

Measurement of Blackbody Response

To determine the infrared photoresponse of the CRC-365, a number of standard blackbody tests were performed. The output signal and noise were measured over a wide temperature range, repeating measurements for two spectral bands and for a number of different biasing conditions. All tests were performed on a spatial-average basis, using the central portion of the detector array.

Several calculated quantities were obtained from the basic signal and noise data, including the sense node capacitance, signal contrast, Schottky quantum yield, and NETD.

Results were generally favorable overall, with the exception of an anomalous effect associated with the temporal noise.

The Electro Optical Industries Model 1805 blackbody mentioned earlier provided flood illumination of the imager. Most tests were performed over the range 15°C to 55°C. Direct illumination was achieved by removing the target plate normally used with the blackbody, and positioning it immediately in front of the entrance window of the dewar. In

this setup, the imaging device views only the temperature-controlled surface inside the blackbody.

The temperature-controlled surface provided by this blackbody has an emissivity of 0.99 in the MWIR. The rms temporal stability and spatial uniformity are better than 0.01 degree. Extremely repeatable results were observed, independent of the exact position of the blackbody.

Detector Output Versus Background Temperature. In this test, the blackbody temperature was varied between 15°C and 55°C, in one-degree steps. At each temperature, the average output of both the entire array and central subarray were recorded. Additionally, the array-wide photocurrent was measured, using an electrometer inserted in the common anode lead of the detector array.

After recording this data, the relationship between analog-to-digital units and signal charge was established. A quadratic expression for the average array output was found, using the electrometer readings as the independent variable. The effect of off-scale outputs on this calculation was ignored.

It was discovered that this function is fairly sensitive to bias potential V_{GG}. The function must be recomputed any time this control, or any other bias potential, is changed. The result obtained for V_{GG} = 0.85 Volts is as shown. The total signal charge is represented by Q_{acc}, in electrons.

$$\#\text{ of ADU} = 1527.8 + (6.418 \times 10^{-3})\, Q_{acc} - (1.103 \times 10^{-9})\, Q_{acc}^2 \qquad (3.15)$$

As an example, consider the case where an average of 100,000 signal electrons per pixel are detected. Applying Eq. (3.15), the average value for the array output is 2159 ADUs.

This function is nonlinear due to the voltage-dependent capacitance associated with the PtSi detectors, as discussed in Chapter 2. An additional source of nonlinearity is related to the transient response of the readout electronics.

As V_{GG} is increased, the column bias current in the readout, I_{BIAS}, increases. This increase in current improves the transient response of the readout electronics. It was observed that the Q_{acc}^2 coefficient of Eq. (3.15) decreases with the increases in V_{GG}. This coefficient changes throughout the allowable operating range of V_{GG}.

This unexpected result further hints at a bandwidth limitation in the CRC-365. This limitation was first mentioned in the dark current discussion. Concluding remarks will be made on this subject in a later section.

To calculate the average signal charge present at the detectors, Eq. (3.15) was solved for Q_{acc} by using the quadratic formula. That result was used to convert the output readings in ADUs to electrons of signal charge. In this step, data values recorded for the central subarray were used to predict the signal charge for that region.

These results are shown in Figure 3.9. The output for the 3.4 - 4.9 μm band is about twice that obtained in the 3.55 - 4.05 μm range. Notice that in the 3.4 - 4.9 μm band, the output corresponding to a 27°C background is about 136,000 electrons.

Recall that the dark charge is around 20,000 electrons. This indicates that the 27°C photoresponse is 116,000 electrons. Using a slightly greater optical bandwidth, Gates (Gates, 1988) observed 130,000 electrons at this background temperature.

Detector Sense Node Capacitance. Equation (3.15) provides the connection between the signal charge present at the detector, and the data acquisition system signal in analog-to-digital units. The derivative of this function is generally called the conversion gain, relating the change in signal electrons to the change in analog-to-digital units in the

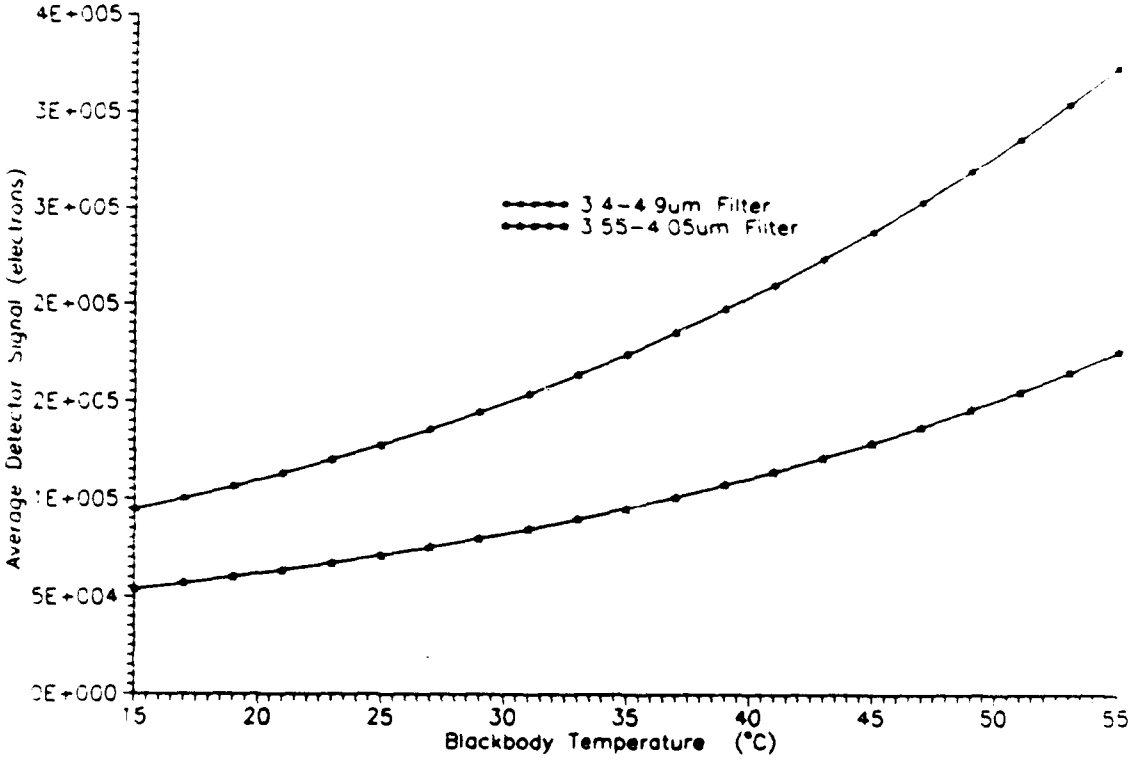

Figure3.9
Detector Output Versus Background Temperature

computer. The conversion gain corresponding to Eq. (3.15) is shown below, expressed in units of ADUs per electron.

$$\text{Conversion Gain} = 6.418 \times 10^{-3} - 2.206 \times 10^{-9}\, Q_{acc} \qquad (3.16)$$

This expression may be divided into the system gain to calculate the effective capacitance present at the sense node. The system gain was discussed in an earlier section. Its value is around 3550 ADUs per Volt.

The detector capacitance is at its minimum value when Q_{acc} is zero. Under these conditions, the effective sense node capacitance is $3550/(6.418 \times 10^{-3})$ or 553,135 electrons per Volt. This result may be expressed in Farads by multiplying by the electronic charge, q. The capacitance is then seen to be 0.089 picofarads. Recall that the value predicted in Chapter 2 was 0.095 picofarads. The measured value is within about 6 percent of the predicted value.

Signal Contrast. Recall that the signal contrast is the derivative of the signal-versus-background temperature curve, expressed in electrons per degree. This is an easily computed measure of camera performance.

The derivative of each signal output curve shown in Figure 3.9 was approximated by calculating the incremental slope at each temperature. These slope calculations involved the data points immediately above and below the temperature of interest. The results are plotted in Figure 3.10.

The signal contrast for the 3.4 - 4.9 μm band is about twice that of the 3.55 - 4.05 μm band. In the 3.4 - 4.9 μm band, about 4200 electrons per degree are obtained, when viewing a background temperature of 27°C.

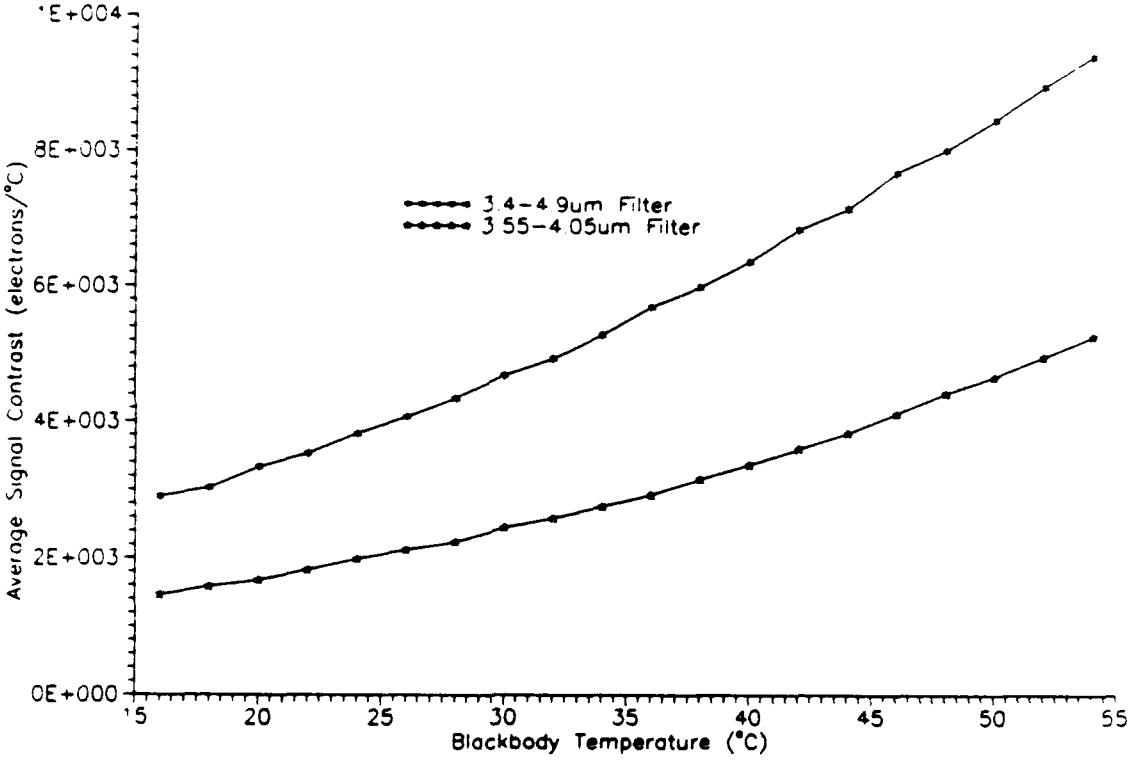

Figure 3.10
Signal Contrast Versus Background Temperature

These results will be used in following sections to compute the Schottky quantum yield and the NETD.

Schottky Quantum Yield. To obtain the Schottky quantum yield, or C_1, coefficient, the signal contrast of the previous section was used. To begin, the theoretical signal contrast was calculated, assuming a C_1 value of 1.00. The experimental C_1 value was then determined by taking the ratio of the two curves. Use of contrast, rather than the total output signal, eliminates additive errors associated with the dark current and imperfect cold shielding.

The theoretical contrast curve was calculated by using the linear methods of Chapter 2. The transmittance of the dewar window and bandpass filter, experimentally measured barrier height, blackbody emissivity, and exact F-number of the system were taken into account in this computation.

The measured and theoretical contrast curves are shown in Figure 3.11, for the 3.4 - 4.9 μm band. The ratio of the two curves is shown in Figure 3.12. Note the similarity between ratios obtained at different background temperatures. The slight downward trend in the ratio, represented by the straight line on the plot, is evidence of detector de-biasing, which for simplicity was not included in the theoretical contrast calculation. The plot shows that the C_1 coefficient has a value of 0.187 at 26°C. Similar results were obtained from the 3.55 - 4.05 μm data.

This C_1 value is not unreasonable when compared to the value of 0.20 used in Chapter 2, but perhaps could be improved on in future devices.

Temporal Noise Versus Detector Output. The temporal noise was measured as a function of background temperature and V_{GG}. The rms noise was then plotted against

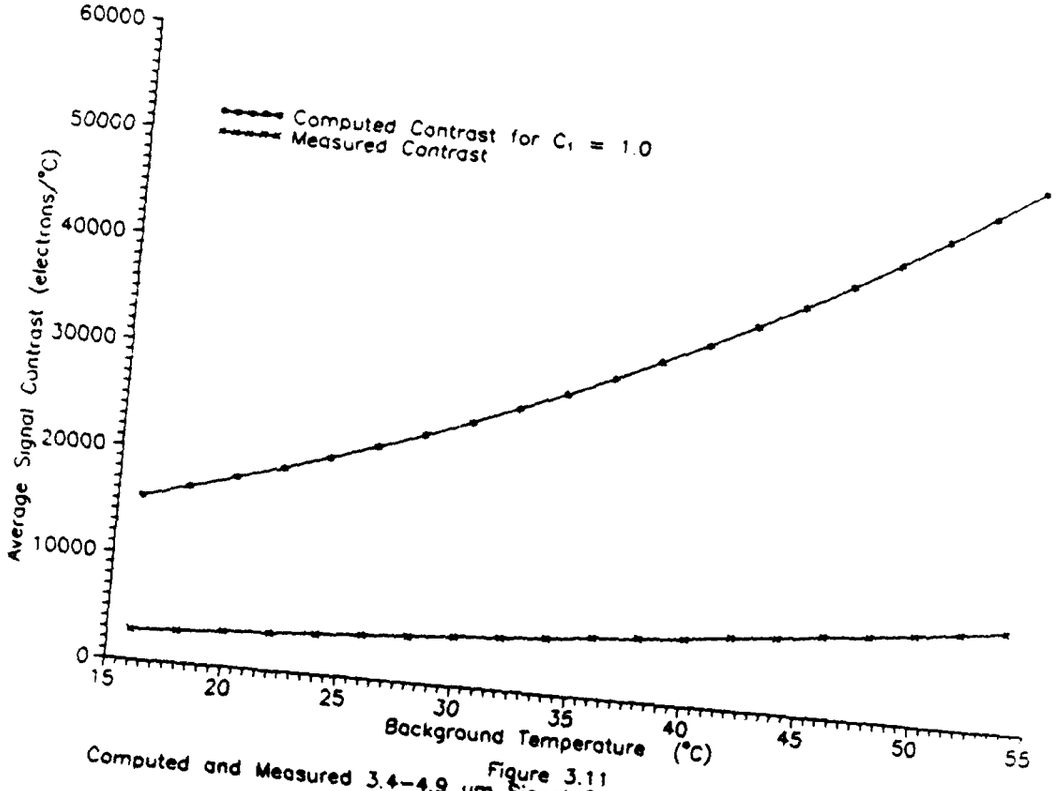

Figure 3.11
Computed and Measured 3.4–4.9 um Signal Contrast Versus Background Temperature

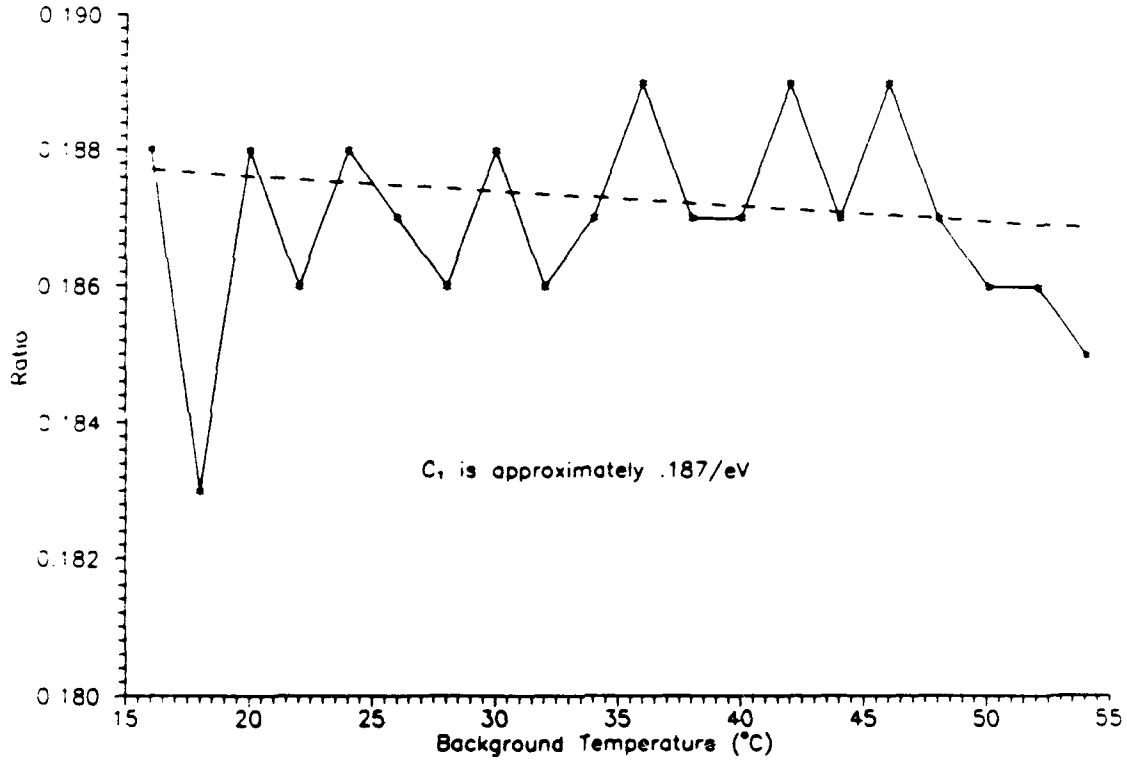

Figure 3.12
Ratio of Measured to Computed Signal Contrast

the mean detector output for further study. Measurements were made for both the 3.4 - 4.9 μm and 3.55 - 4.05 μm spectral bands.

In this test, the Electro Optical Industries blackbody was again used to flood illuminate the imager. Data was collected in two-degree steps between 15°C and 55°C, using a frame differencing method. Extensive checking of results taken between different spectral bands suggest that the blackbody itself imparts no significant error to these measurements.

In this method, the data-acquisition system was programmed to capture only the data from the central subarray. A reference frame was first captured and stored in memory. Immediately thereafter, a second frame was captured and subtracted from the reference frame.

The rms value of this difference frame was then divided by $2^{1/2}$, to account for the double sampling of the noise. Following this step, the result was further adjusted, to remove the quantization noise. This was done by R.S.S. subtracting the reciprocal of the square root of 12 from the reading. This result was then recorded.

This process was repeated from 10 to 20 times at each background temperature. The average value of these readings was taken to be the temporal noise, in analog-to-digital units. Equation (3.16) was then used to scale to electron units.

Figure 3.13 shows the noise results obtained in the 3.4 - 4.9 μm band, using a V_{GG} setting of 0.85 Volts. The measured noise variance is plotted as a function of the mean signal level.

Consider the temporal noise on a mean signal of about 155,000 electrons. Figure 3.13 shows a noise variance of around 200,000 electrons, which is equivalent to 450 rms electrons. Using Eqs. (3.6), (3.8), and (3.16), this corresponds to about 575 microvolts

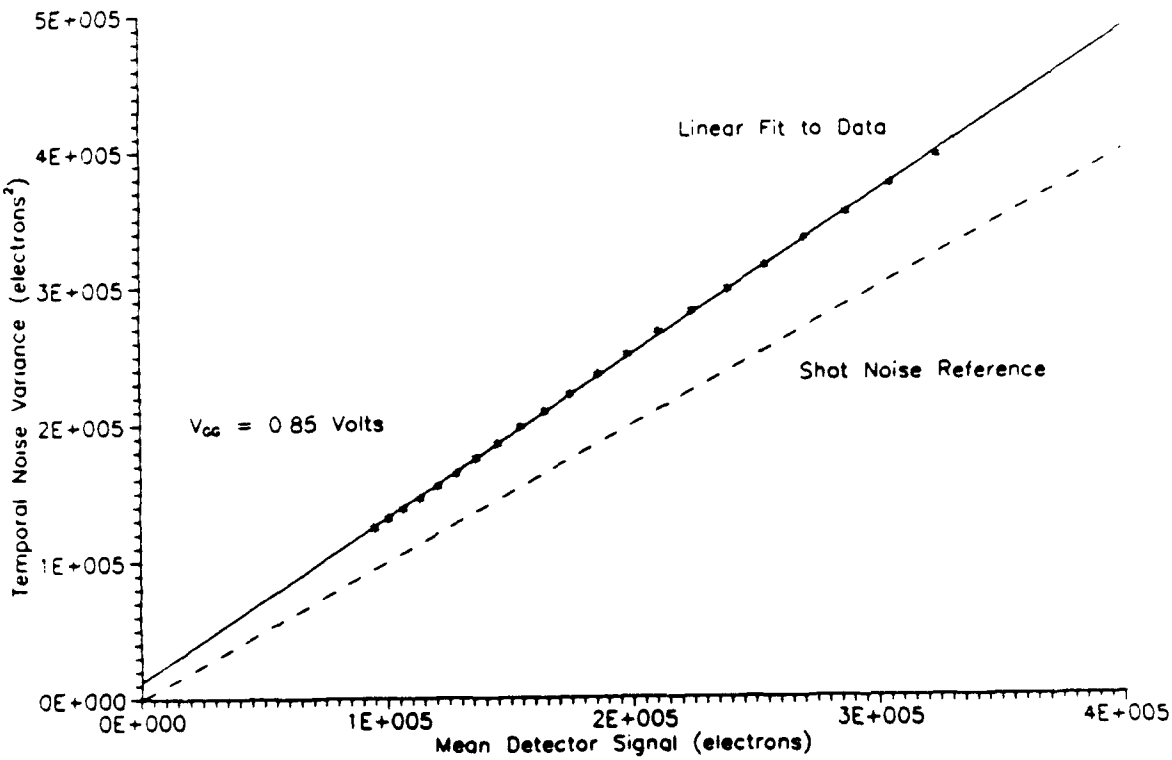

Figure 3.13
3.4–4.9um Temporal Noise Versus Mean Detector Signal

of noise at the imager output. Gates (Gates, 1988) reported between 500 and 640 microvolts under these conditions.

This type of plot was first described in detail by Mortara and Fowler (Mortara and Fowler, 1981). It is generally referred to as a mean-variance plot.

In this type of plot, the y intercept of the noise profile is referred to as the read noise. In this figure, the read noise is seen to be about 85 rms electrons. This value was obtained by applying a least-squares fit to the data below about 175,000 electrons, where excellent linearity is displayed by the data points.

The read noise in this system can be accounted for by considering the kTC noise associated with resetting the detectors, and the noise of the video signal conditioning electronics.

A full description of reset noise is given by Beynon and Lamb (Beynon and Lamb, 1980). The rms reset noise associated with a capacitor of value C, operating at an absolute temperature T, is as shown. This result is expressed in rms electrons. The term k is Boltzman's constant, and q is the electronic charge.

$$\text{RMS Reset Noise} = (k\,T\,C)^{\frac{1}{2}} / q \tag{3.17}$$

For the device under test, recall that the zero-signal effective capacitance is 0.089 picofarads, and the operating temperature is 79°K. Using these values in the equation, the reset noise is seen to be about 60 electrons.

Early tests of the video signal conditioning electronics revealed a noise level of about 0.55 rms ADUs. Using Eq. (3.16), this corresponds to abut 85 rms electrons of noise.

The R.S.S. combination of these noise sources is 105 electrons, quite close to the measured read noise of 85 electrons.

Notice that the slope of the noise data exceeds that of the shot-noise reference line provided on the plot. Ideally, one would prefer a noise profile which runs parallel to this line, offset vertically by the read noise. An idealized device would have the following variance behavior. The variance, mean and read noise are in electron units.

$$\text{Ideal Case:} \quad \text{Variance} = (\text{Mean Signal}) \times 1.0 + \text{Read}^2 \tag{3.18}$$

The mean-variance test mentioned earlier assumes this relationship is valid, allowing one to determine the conversion gain from the slope of the plot.

Figure 3.13, however, suggests the presence of an unwanted, anomalous noise process in the device. For this reason, the mean-variance method is not appropriate for determining the conversion gain of the CRC-365.

To further investigate this effect, the bandwidth of the readout was increased by raising V_{GG}. Figure 3.14 shows the noise profile for a V_{GG} setting of 0.95 Volts. Ignoring the behavior near the high end of the scale, note that the read noise and slope of the noise plot have increased slightly in comparison to the data for V_{GG} = 0.85 Volt. Using the least-squares method, a line was again fitted to data in the 0 to 175,000 electron range.

The linear equations expressing the measured noise variance for the two cases are shown below.

$$V_{GG} = 0.85\ \text{V:} \quad \text{Variance} = (\text{Mean Signal}) \times 1.2350 + 85^2 \tag{3.19}$$

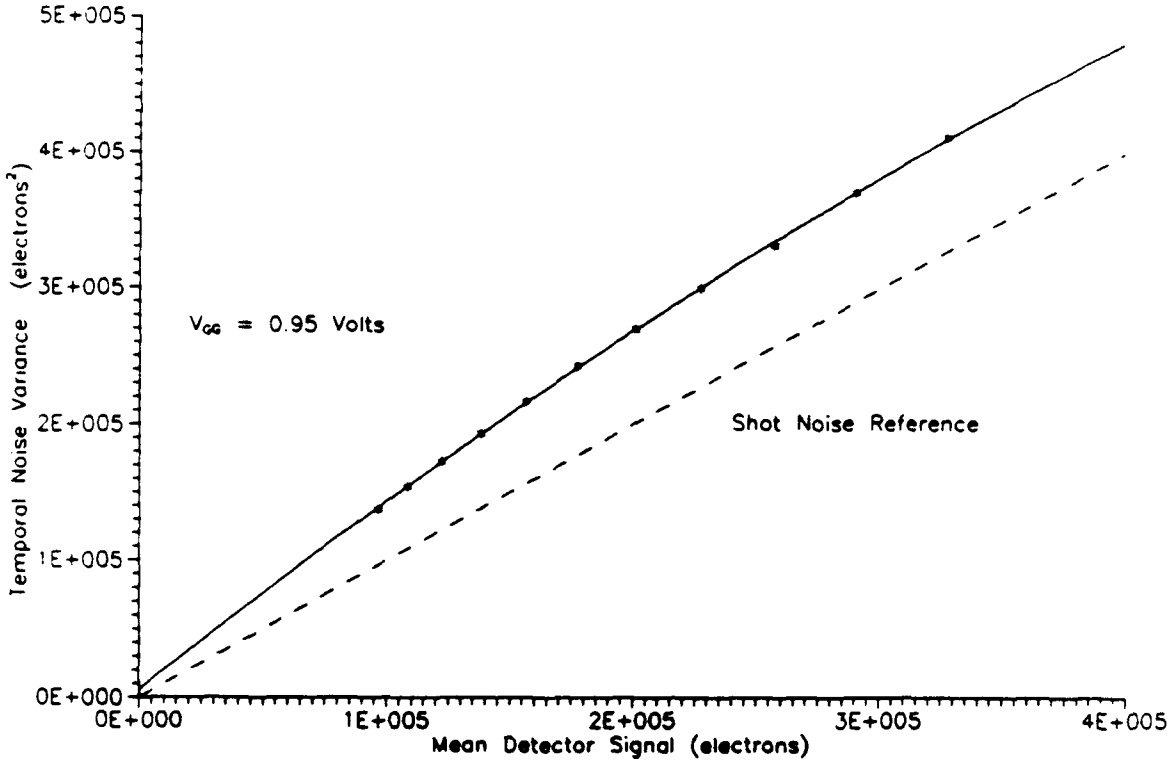

Figure 3.14
3.4–4.9um Temporal Noise Versus Mean Detector Signal

$$V_{GG} = 0.95\ V: \quad \text{Variance} = (\text{Mean Signal}) \times 1.2987 + 115^2 \tag{3.20}$$

Considering only the anomalous noise source, the following expressions are obtained.

$$V_{GG} = 0.85\ V: \quad \text{Excess Noise (Variance)} = (\text{Mean Signal}) \times 0.23 \tag{3.21}$$

$$V_{GG} = 0.95\ V: \quad \text{Excess Noise (Variance)} = (\text{Mean Signal}) \times 0.30 \tag{3.22}$$

The ratio of the excess noise variance between the two cases is 1.27. It is reasonable to compare this figure to the bandwidth ratio corresponding to the two V_{GG} settings.

For a source-follower, the dominant pole and hence low-pass cut-off frequency is largely controlled by the transconductance, g_m. The bandwidth increases linearly with the transconductance. Recall that in Chapter 2, Eq. (2.71) showed that the transconductance is related to the square root of the column bias current, I_{BIAS}. For the two V_{GG} cases under consideration, the ratio of the corresponding I_{BIAS} values is 1.58, indicating a bandwidth increase of $(1.58)^{1/2}$ or 1.26, as V_{GG} is raised from 0.85 Volts to 0.95 Volts.

In the electronic amplification of noise, the noise variance at the output of an amplifier is scaled in linear proportion to the bandwidth. In this system, for data in the range 0 to 175,000 electrons, a 1.26 increase in the bandwidth results in a 1.27 increase in the excess noise variance. This indicates that the excess noise source indeed originates from a point preceding the detector source-follower circuit.

It is not clear what this noise source physically corresponds to. Because this noise increases linearly with the mean, it may be related to shot noise across the Al/Si Schottky

contact used to connect the anode of the detector array. This effect does not degrade the overall noise performance drastically, but deserves further investigation.

Overall signal-to-noise ratio for infrared systems is usually expressed by the NETD. This will be discussed in the following section.

Noise-Equivalent Temperature Difference (NETD). The Noise-Equivalent Temperature Difference was briefly discussed in Chapter 2. It is a fairly useful measure of infrared camera performance, insofar as the temporal noise is concerned. Recall that it is the ratio of the temporal noise to the signal contrast, each expressed in similar units.

The system NETD was determined from measured data as a function of background temperature, using Figures 3.9, 3.10 and 3.13. Recall that Figure 3.13 gives the temporal noise for V_{GG} = 0.85 Volts. These results are plotted in Figure 3.15. As an example of how the NETD is calculated, consider the 3.4 - 4.9 μm bandpass, at a background temperature of around 27°C. At this background temperature, Figure 3.9 shows a total signal of about 135,000 electrons. At this signal level, Figure 3.13 indicates a variance of around 176,000 (electrons)^2, corresponding to an rms value of slightly less than 420 electrons. Dividing this by a contrast of 4200 electrons per degree Centigrade, from Figure 3.10, the NETD is about 0.099°C.

Using a slightly greater optical bandwidth, Gates (Gates, 1988) observed NETD's in the range 0.08°C to 0.10°C, for a 27°C background.

The added effect of the anomalous noise source discussed in the previous section is not great. If it were not present, the system NETD would be 0.090, an improvement of only 9 percent. If the read noise were also zero, the NETD of the device and system would be 0.087, representing only a 12 percent improvement over measured performance. The temporal noise properties of the device do not significantly limit system performance.

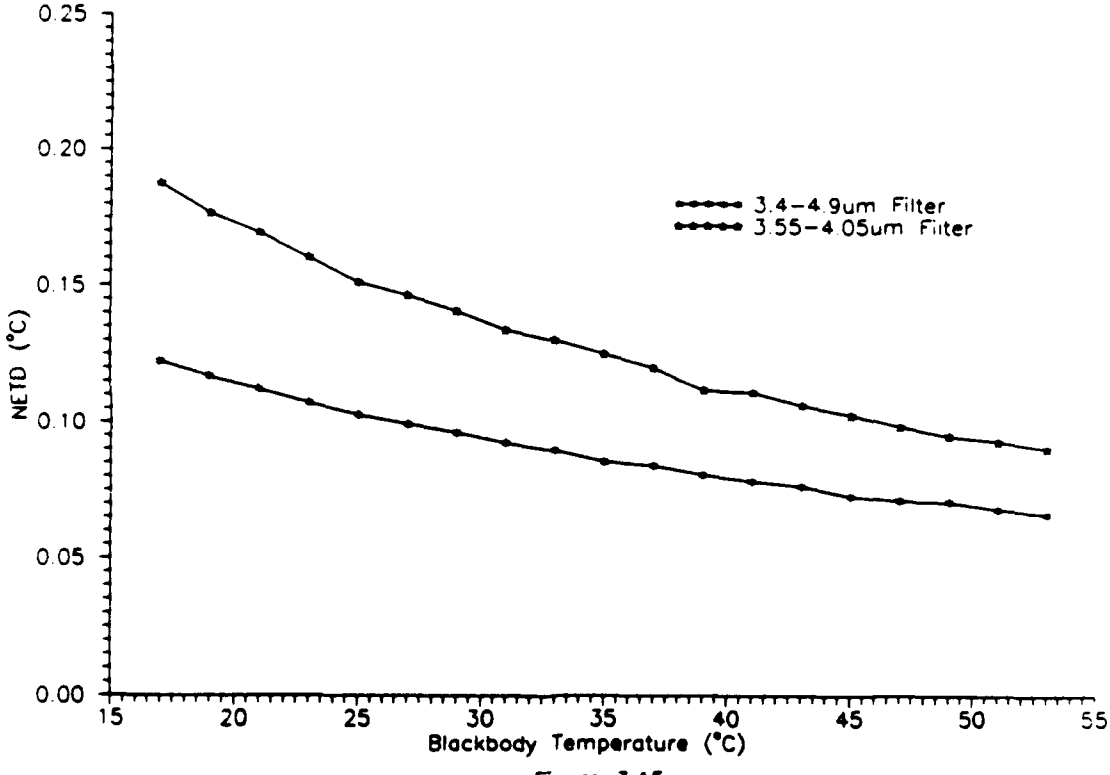

Figure 3.15
Measured Noise–Equivalent Temperature Difference Versus Background Temperature

If lower NETDs were required of an infrared system of this type, one would operate at full optical bandwidth, at lower F-numbers, and with optimum optical transmission.

To realize further improvements, the Schottky quantum yield of the CRC-365 would have to be higher, or perhaps one could gain marginal barrier height advantages by increasing the detector bias. This topic is addressed in the next section.

Detector Bias Effects. To this point, the effects of detector bias on the photoresponse have not been mentioned. Recall that the detector bias level affects the Schottky barrier height, quantum yield, and thermal barrier height. To quantify the effects of detector bias, the contrast and noise were observed at a background temperature of 26°C.

The detector array was operated at reset voltages in the range 1.25 Volts to 3.75 Volts. Contrast and noise data were taken at 0.5-Volt intervals across this range. Recall that the nominal setting used for all other tests in this section is 3.75 Volts.

The relative contrast at each bias setting was measured by capturing 21°C and 31°C data frames from the nonuniformity corrector. The spatial average of their difference was recorded, and later scaled to appropriate units. This method of determining the contrast tends to produce slightly optimistic results when compared to estimates made over a smaller temperature range. The 10°C degree range was used in these tests to secure adequate numerical precision for subsequent studies of the NETD versus bias. The noise was measured at 26°C, using the frame differencing method described earlier.

The results of these tests are shown in Figures 3.16 and 3.17. The contrast in both spectral bands suffers greatly as the bias is reduced. Reductions of about 30 percent are seen as the bias is dropped to its minimum value. Notice, however, that the temporal noise also decreases rapidly.

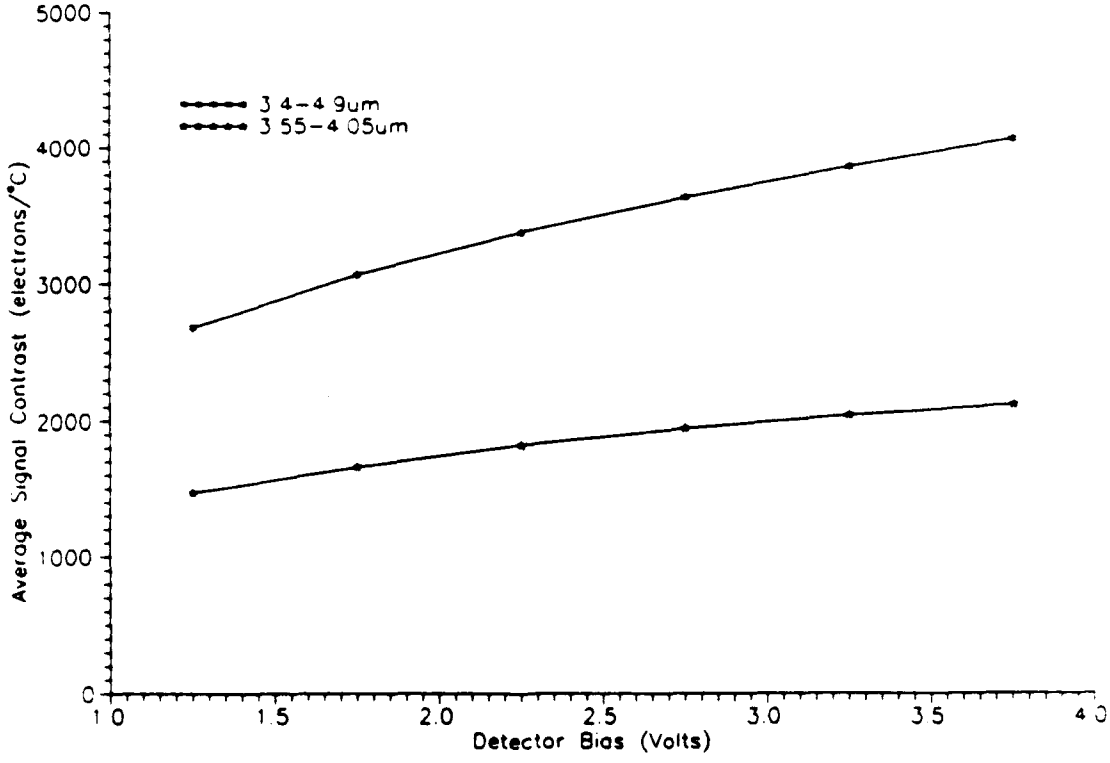

Figure 3.16
Signal Contrast Versus Detector Bias For 26°C Background

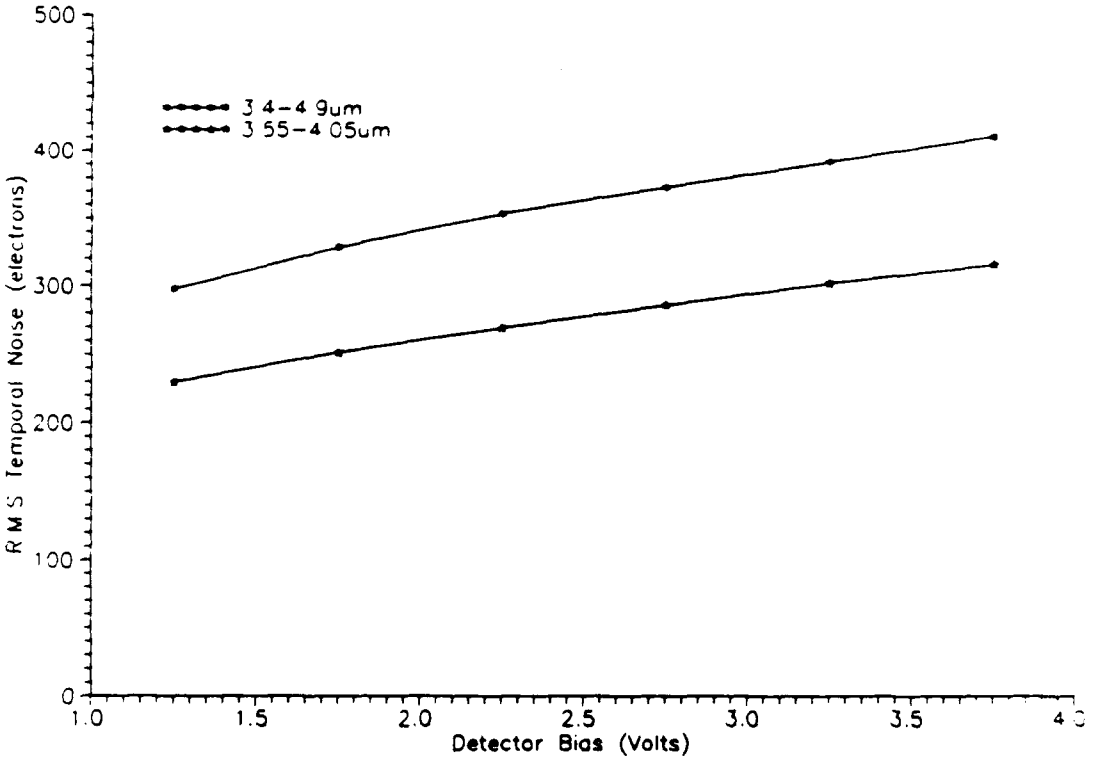

Figure 3.17
Temporal Noise Versus Detector Bias For 26°C Background

To determine the impact of these changes, the NETD was calculated from these figures. This result is shown in Figure 3.18. A very interesting effect appears in these plots. Examining the 3.55 - 4.05 μm curve, notice that the system NETD actually goes through a minimum, or optimal, point at around 2.75 Volts of detector bias.

It is significant that an optimal bias value has been identified for these PtSi photodiodes. To date, this type of behavior has not been reported.

This optimal point is probably unique to PtSi photodiodes used in Hughes Aircraft Company high fill factor detector arrays. These photodiodes feature a novel self-guarding architecture (Shepherd, 1985) which eliminates conventional detector guard rings. This self-guarding architecture results in extremely high fill factors, at the expense of a rather soft reverse breakdown characteristic. It is this early breakdown that is most likely a key factor in the observed NETD profile.

At the optimal point, the Schottky barrier height and quantum yield have improved considerably over their low bias values, resulting in better overall photoresponse and NETD. The dark current has not yet increased enough to seriously undermine these gains. As the bias is increased still further, the dark current is believed to become more dominant as the detector gradually approaches breakdown, which raises the NETD above its optimal value.

Notice that although a minimum does not clearly exist for the 3.4 - 4.9 μm band, the slope of the NETD curve is quite shallow at 3.75 Volts, indicating that further increases in bias are not warranted.

This concludes a discussion of the thermal response of the CRC-365. It has been shown that the tested device behaves quite adequately, with the exception of a small anomalous effect in the temporal noise. Further evidence was given for an apparent bandwidth limitation in the device.

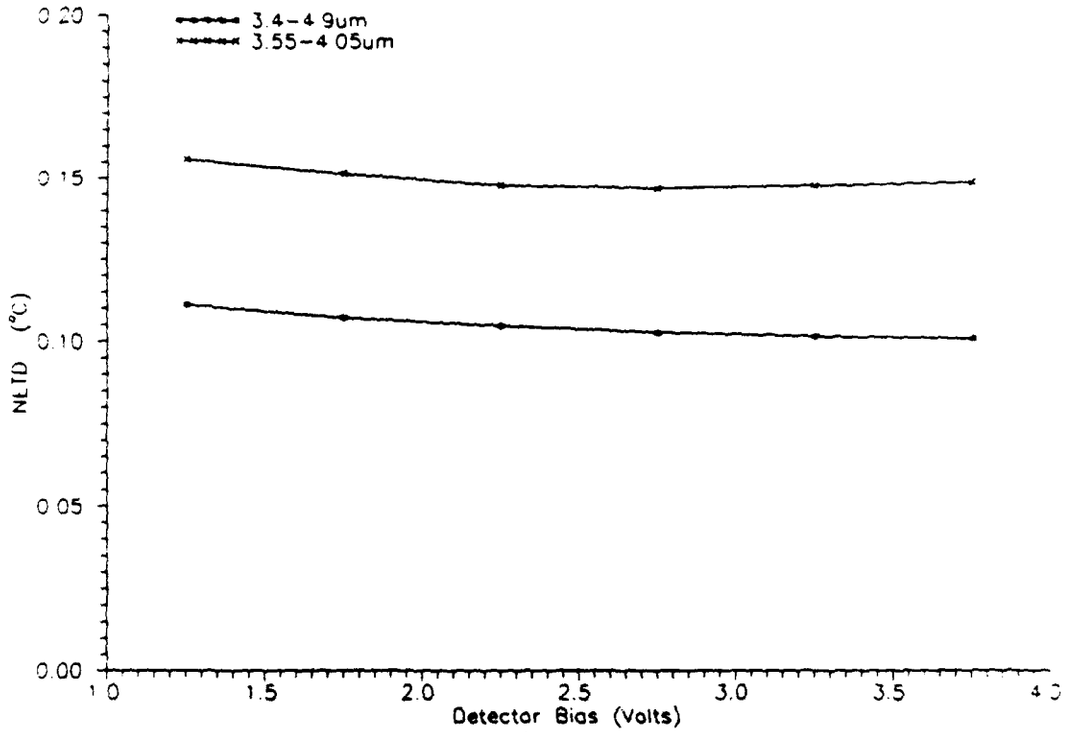

Figure 3.18
Noise–Equivalent Temperature Difference Versus Detector Bias For 26°C Background

Measurement of Response Nonuniformity

Response nonuniformity was measured as a function of background temperature, both with and without nonuniformity correction. In all cases, the Electro Optical Industries blackbody was used to provide uniform illumination of the imager. All data collected from the nonuniformity corrector was obtained by using its temporal frame averaging option. The results of these nonuniformity tests are reported for the central region of the detector array, in rms analog-to-digital units. Recall that the analysis of Chapter 2 requires output voltage or analog-to-digital units for further interpretation of the nonuniformity.

As in the dark current nonuniformity measurement, a special method was used to collect data from the device. In this method, the mean and variance are recorded for the entire central subarray, as well as for sister pixels in that region. This approach allows one to take periodic variations in the readout electronics into account during subsequent calculations of nonuniformity.

These sister pixels occupy the same relative position within 4 x 2 pixel arrays stacked within the central 136 x 136 subarray. Each of the eight sister pixel groups contain 2312 pixels. Recall that pixels are numbered up, and to the left, from a (1,1) position in the lower right corner of monitor photographs.

As an example, pixel (61,61) lies in the lower right corner of the central subarray. Moving to the left 4 pixels, the first sister pixel in the x direction is (65,61). Moving upward from (61,61) by two pixels, the first sister pixel in the y direction is (61,63). The x direction corresponds to the fast readout axis.

The 4 x 2 pattern was found by inspecting mean and variance calculations on sister pixels defined by an 8 x 8 array. The 4 x 2 repetition sequence was easily identified on this basis.

Overall results of these tests were excellent, with the exception of bandwidth-related effects noted in previous sections. Complete interpretation of these results is provided in Chapter 4.

Uncorrected Spatial Noise. The uncorrected camera output was observed over a background temperature range of 20°C - 40°C. The appearance of the video monitor during these tests is as shown in Figure 3.19.

All of the defects noted in the dark current tests are also present in this picture. Unlike the dark current photograph of Figure 3.2, the corners of the array are darker than the center. During fabrication, the anti-reflection coating was omitted from these areas. The detectors in these regions do not respond as strongly at those in the remainder of the array.

The uncorrected nonuniformity was found to be largely independent of the background. Results are plotted in Figure 3.20, for the best and worst sister pixel groups, as well as for the entire test region.

Spatial Noise Under One-Point Correction. Recall that the nonuniformity corrector box is capable of calculating and displaying one-point corrected images from the camera. Typical monitor displays under one-point correction are shown in Figures 3.21 and 3.22. Figure 3.21 corresponds to a 26°C background corrected by a 26°C average frame. Compare the extremely smooth texture of this output to that of the uncorrected camera, shown earlier in Figure 3.19. No spatial noise is seen, with the exception of a few poorly corrected pixels in the diagonal defect on the right.

Figure 3.22 features a 30°C frame corrected by a 26°C reference frame. Note that this output closely resembles the uncorrected output, even though the background temperature has changed only 4 °C. This illustrates the idea of residual spatial noise. Even

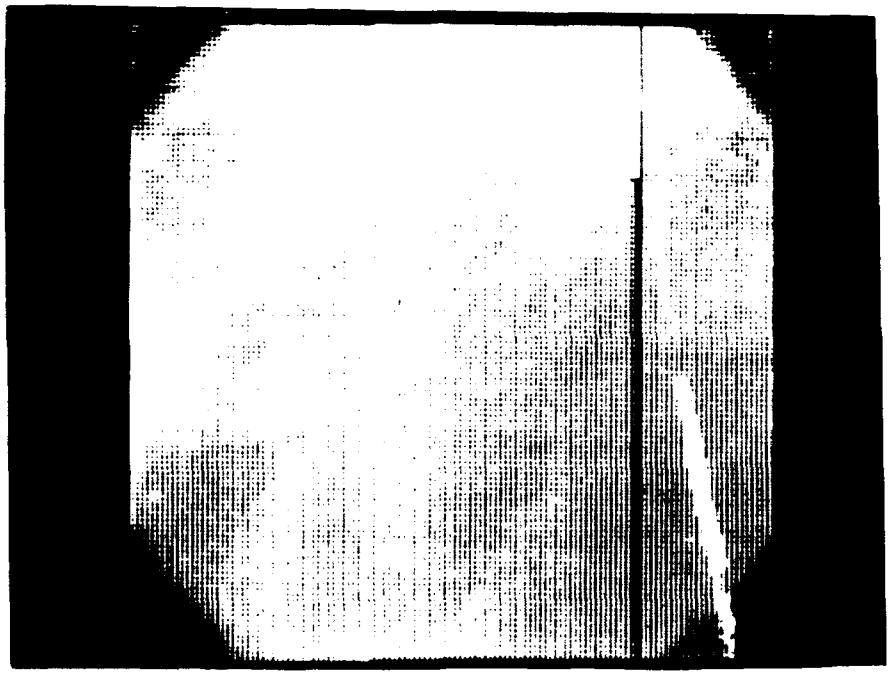

Figure 3.19 Uncorrected camera output at 26°C background

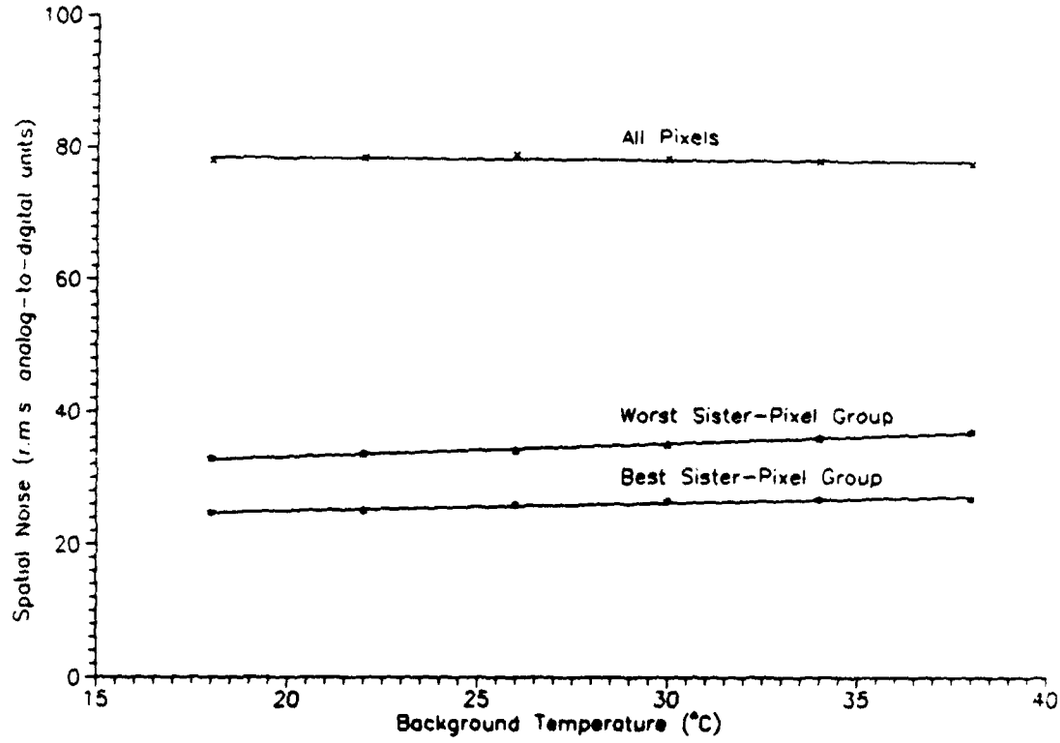

Figure 3.20
Uncorrected Spatial Noise Versus Background Temperature

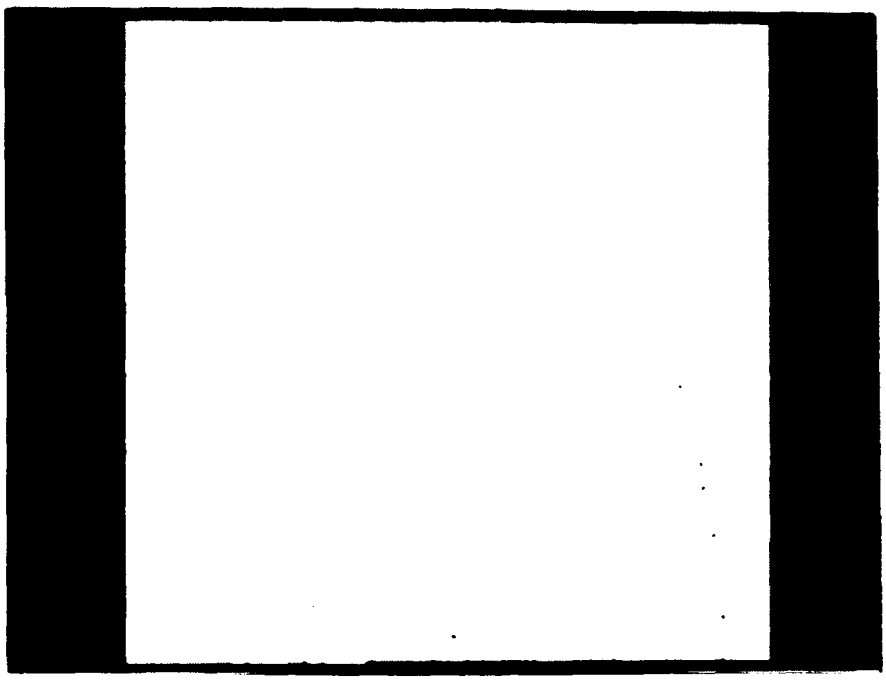

Figure 3.21 26°C response, one-point-corrected by 26°C reference frame

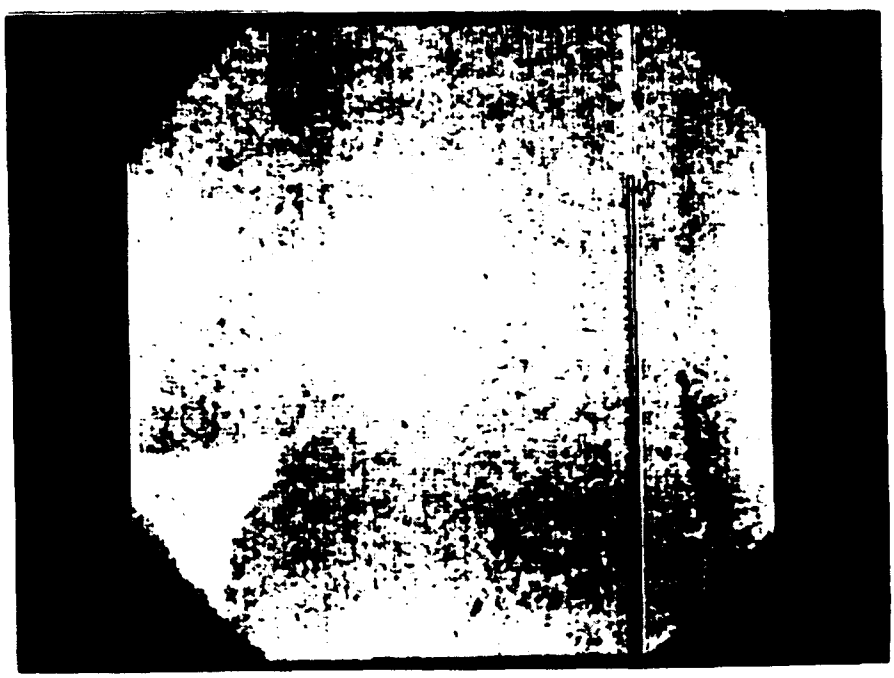

Figure 3.22 30°C response, one-point-corrected by 26°C reference frame

though the spatial noise appears to be quite bad in this photograph, the camera is still fairly well corrected. The display controls have been set to emphasize the changes which occur in the corrected image as the background temperature moves away from the calibration point.

Before attempting to fully quantify the spatial noise properties of the device, an optimization procedure was used to establish the best setting for bias potential V_{GG}. This was done by capturing average frames at 21°C and 31°C. The spatial noise of their difference was calculated and recorded. This procedure was repeated for a number of V_{GG} values spaced at 25-millivolt intervals. These results are plotted in Figure 3.23.

Note that the residual spatial noise, as a fraction of the net change in signal, drops to as low as 1.1 percent as V_{GG} is increased. A setting of 0.85 Volts was found to yield satisfactory one point-corrected imaging at a reasonable level of device power dissipation.. Recall that this value was used almost exclusively in the tests of previous sections.

To fully quantify the residual spatial noise, a temporally averaged 17°C reference frame was obtained from the nonuniformity corrector. This frame was stored in memory, and used throughout the remainder of the test. The blackbody was then stepped through the 15°C - 55°C range, capturing average frames at two-degree intervals.

These frames were one-point corrected by the 17°C reference frame stored in memory. Statistics were then recorded for these difference frames.

After removal of quantization noise, the results are as shown in Figures 3.24 and 3.25. Quick examination of the 55°C data reveals an array-wide nonuniformity of just over 1 percent, the same as previously found during optimization.

Spatial Noise Under Two-Point Correction. Unlike one-point-corrected images, two-point-corrected images must exclusively be formed off-line, using software

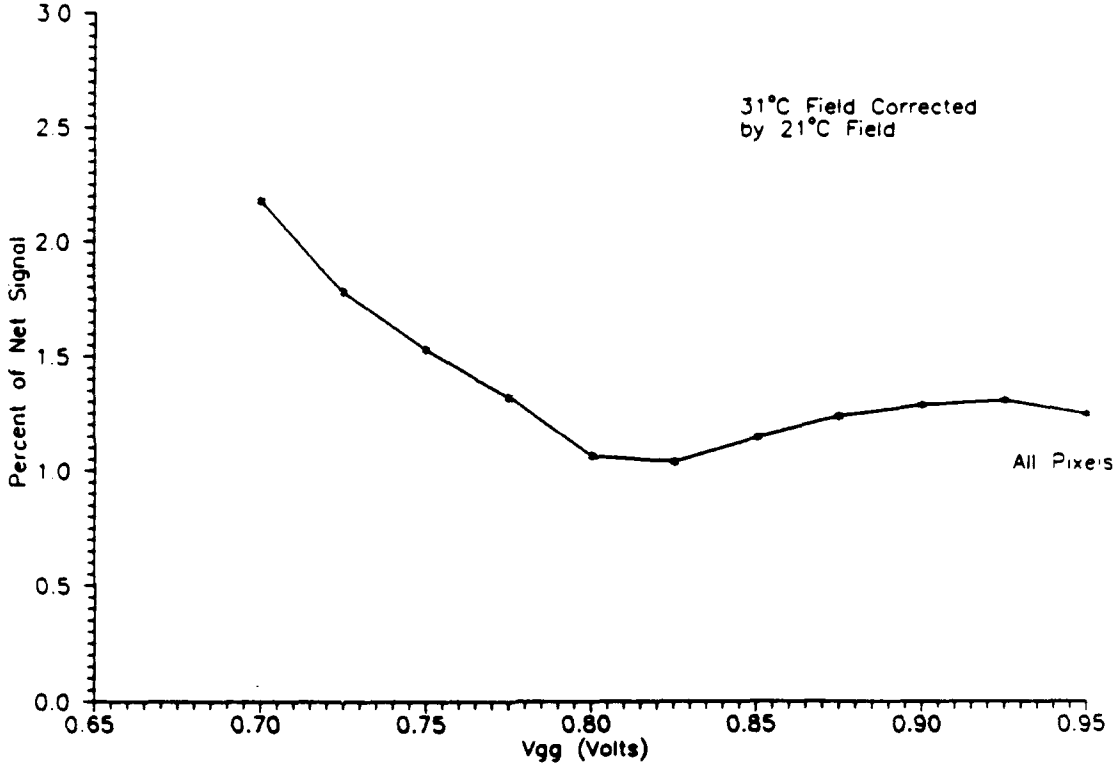

Figure 3.23
R.M.S. Spatial Noise Versus V_{gg} Under One-Point Correction

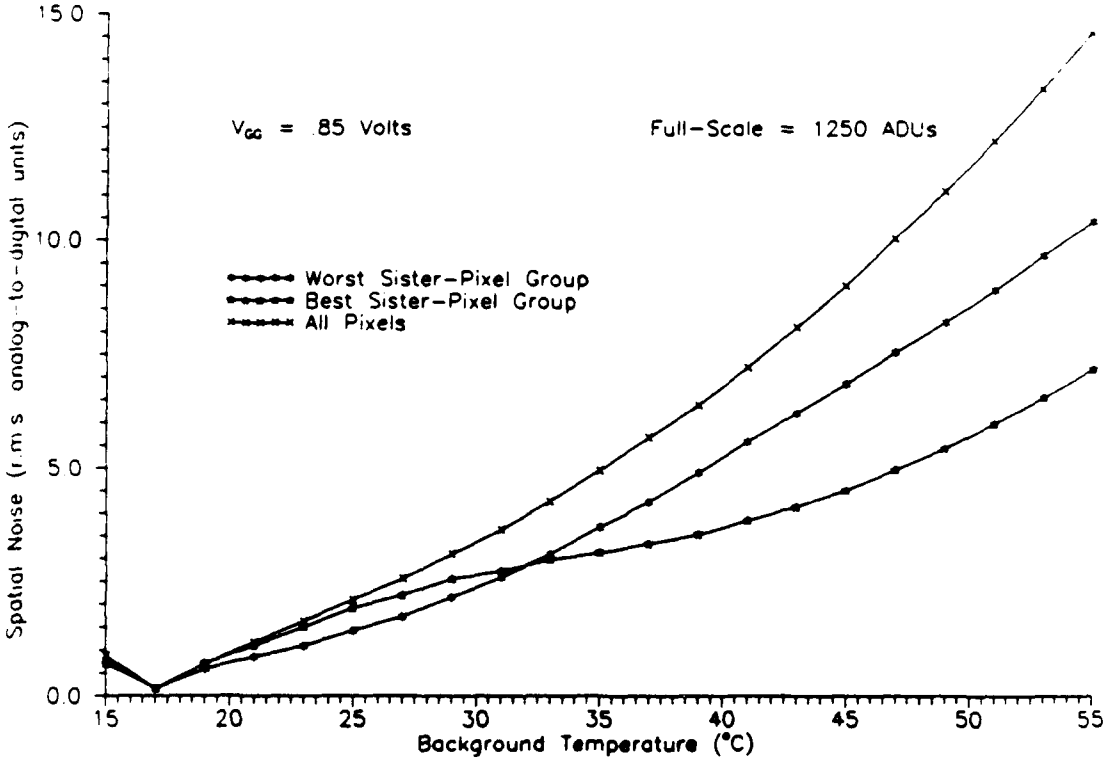

Figure 3.24
Residual Spatial Noise Under One-Point Correction

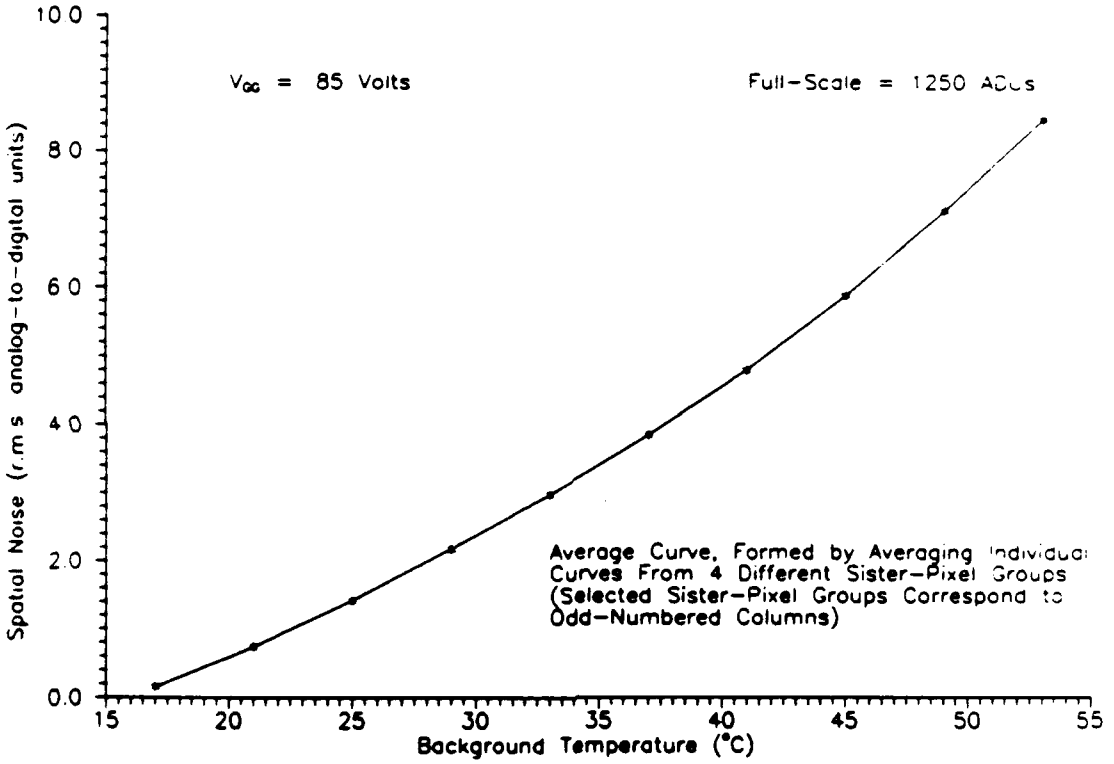

Figure 3.25
Typical Residual Spatial Noise Under One-Point Correction

routines available in the data-acquisition system. These calculations make use of stored reference frames taken near the extremes of the operating temperature range.

In these tests, averaged reference frames were formed at 17°C and 53°C. Data frames were taken at two-degree intervals throughout this range. As each frame was captured, the two-point correction for that frame was calculated. Statistics were recorded for the corrected frame before moving to the next temperature of interest.

As in the one-point tests, the effect of bias potential V_{GG} was investigated before attempting to record full sets of data. In this optimization, V_{GG} was again adjusted in 50-millivolt steps. At each new setting, the residual spatial noise was recorded. The reference frames were formed at 17°C and 53°C, whereas the post-correction residual noise was evaluated at 35°C. Recall that the post-correction noise is the greatest near mid-scale. These results are shown in Figure 3.26.

This figure reveals very important information about the CRC-365. Note that for the best group of pixels, the residual spatial noise curve has a very shallow slope as V_{GG} is increased to around 0.95 Volts. The two-point correction is good to at least 1 part in 2000 for these pixels. Actually, four of the eight sister-pixel groups exhibited this high level of performance. These four groups were found to correspond to the odd columns of the readout device.

Unfortunately, the even columns, and hence the total noise profile, show no limiting behavior as V_{GG} is increased to its maximum allowable value. This is the third instance in which evidence of a bandwidth limitation in the CRC-365 has been cited. The best performance seen in the even columns is about half that of the odd columns. This is an undesirable effect which limits the overall performance of the device.

Since corrections can only be formed in the computer, no monitor photographs are available. Limited display capability available from the software package indicated,

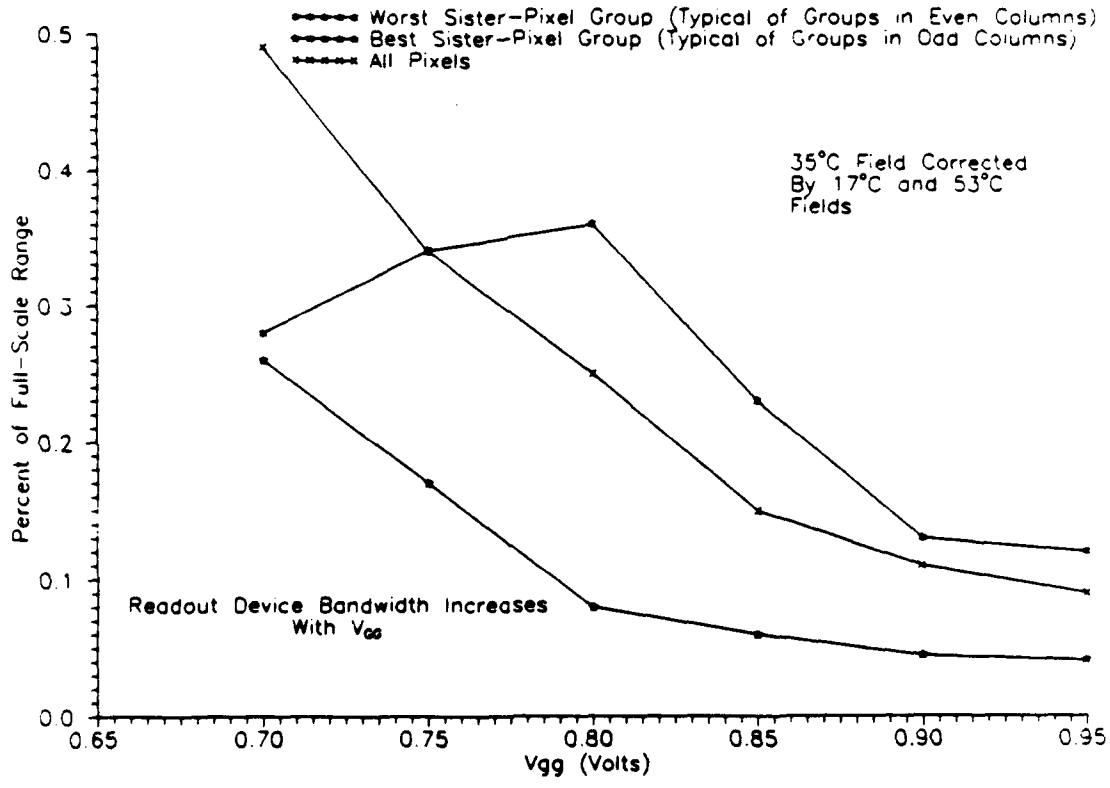

Figure 3.26
R.M.S Spatial Noise Versus V_{gg} Under Two-Point Correction

however, that the two-point images are quite similar to Figure 3.21. Only slight spatial structure was visible along even-numbered vertical columns of the array.

Using a V_{GG} setting of 0.95 Volts, data for the entire operating range were collected. These results are shown in Figure 3.27. Note that quantization noise and residual temporal noise were removed from the data before plotting. The plots do not go completely to zero at the reference temperatures due to drift effects and limited numerical precision in the multiplier coefficients. The noise levels at 35°C are the same as those shown in Figure 3.26.

Even including the anomalous behavior of the even columns, these preliminary indications of performance appear to be quite good. At the worst point in the test range, the spatial noise never exceeds the temporal noise.

Minimum Resolvable Temperature Difference (MRTD)

The Minimum Resolvable Temperature Difference test, or MRTD, is a highly standardized test procedure used to compare infrared imaging systems. This test was performed under the guidelines published by Lloyd (Lloyd, 1975).

This test involves human observations of the video output of the system. A special thermal target, consisting of four bars, is viewed by the infrared camera. The goal is to determine the differential bar temperature at which the observer can just resolve the bars in the image.

This test is repeated at a number of spatial frequencies. In the testing reported here, this was accomplished by using bar patterns of different sizes, and by physically moving the target to different positions relative to the camera. The Electro Optical Industries blackbody was used for this test.

Theoretical predication of the MRTD is still an area of active research. Many fairly accurate models have been developed for use with scanning imaging systems. MRTD

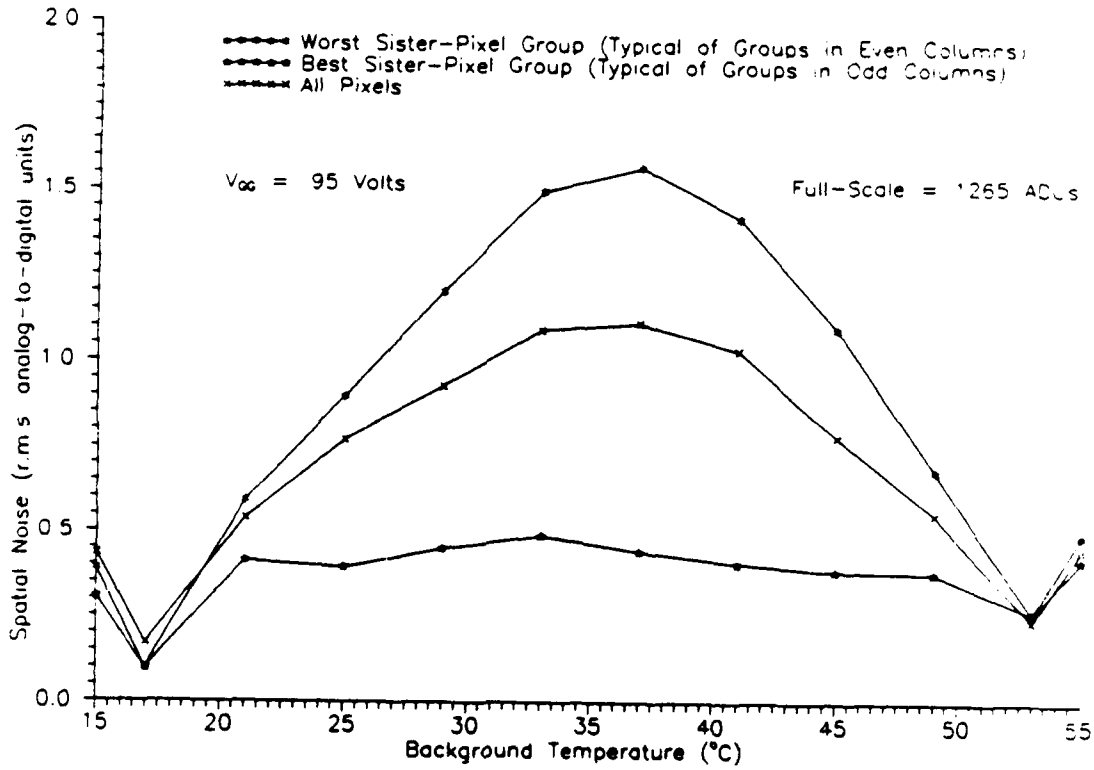

Figure 3.27
Residual Spatial Noise Under Two-Point Correction

models for focal plane based systems are less mature, where the effects of uncorrected spatial noise must be accounted for.

A compact expression has been developed by Mooney (Mooney, 1991) for use with either fully or partially corrected staring imaging systems. His result for the MRTD is as shown.

$$MRTD = NETD \times \left(SNR_{th} / k(a)^{\frac{1}{2}}\right) \times \left(\sigma_{acc} / \sigma_{tmp}\right) \times \left(\zeta / \zeta_N\right) \tag{3.23}$$

The SNR_{th} term is the threshold signal-to-noise ratio required by the observer to resolve the target. The k term is the ratio of the eye integration time to the frame time. The (a) term is the aspect ratio of the pixel, or detector.

The term ζ/ζ_N is the spatial frequency of the target, written as a fraction of the Nyquist frequency. One cycle of a bar image at the Nyquist frequency occupies two pixels.

The σ_{tmp} term is the temporal noise at the camera output. The σ_{acc} term is the accumulated noise, taking into account all temporal and spatial noise sources. The sources are combined as follows, where $\sigma_{spatial}$ represents the spatial noise (Mooney, 1991).

$$\sigma_{acc}^2 = k\,\sigma_{tmp}^2 + k^2\,\sigma_{spatial}^2 \tag{3.24}$$

The MRTD testing presented in this section was done with complete correction of the spatial noise. For this case, $\sigma_{spatial}$ is zero. Mooney's expression then becomes the following.

$$MRTD = NETD \times \left(SNR_{th} / (ka)^{\frac{1}{2}}\right) \times \left(\zeta / \zeta_N\right) \tag{3.25}$$

The appearance of the monitor before removal of spatial noise is shown for reference in Figure 3.28. This photograph is identical to Figure 1.1, in which a differential bar temperature of 3°C is just visible above the spatial noise.

Figure 3.29 shows the appearance of the monitor during the actual test. The bars shown in this picture are at a differential temperature of 0.15°K, which is slightly above the MRTD. Notice the smooth texture of the surrounding region. In fact, the spatial noise has been completely eliminated. This was achieved by using the one-point correction mode provided by the nonuniformity corrector. It was used for all MRTD measurements, recalibrating as needed as the target was repositioned.

Figure 3.30 shows the MRTD plot obtained by averaging the responses of several observers. Notice the excellent linearity of the averaged responses shown in the plot. This plot was obtained using the 3.4 - 4.9 μm filter. The measured NETD with the infrared lens in place was 0.114°K. The NETD was somewhat higher than reported earlier, due to transmittance losses in the lens.

Notice that at low spatial frequencies, an average observer can resolve a differential temperature of around 0.01°K. Recall that the theoretical study of spatial noise presented in Chapter 2 used a figure of 0.015°K as a performance goal in corrected imaging.

Using Eq. (3.25), with a threshold signal-to-noise ratio of 2.5, an eye integration time of 0.1 seconds, a frame time of 1/60 second, an aspect ratio of 1.0, and an NETD of 0.114°K, one would expect an MRTD of 0.116°K at the Nyquist frequency. This theoretical MRTD is shown for reference in Figure 3.30.

The measured MRTD at the Nyquist limit was 0.126. This is within 9 percent of the theoretically predicted value. Note, also, that the theoretically predicted MRTD line touches 8 of 10 of the vertical error bars associated with the measured data. The agreement

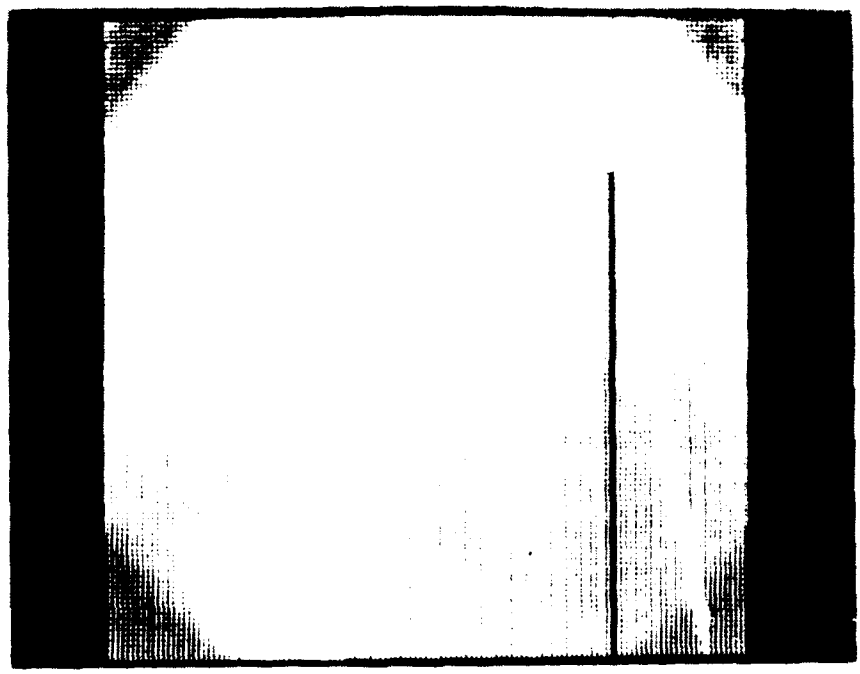

Figure 3.28 MRTD test with uncorrected spatial noise and 3°C differential bar temperature

Figure 3.29 MRTD test with zero spatial noise and 0.15°C differential bar temperature

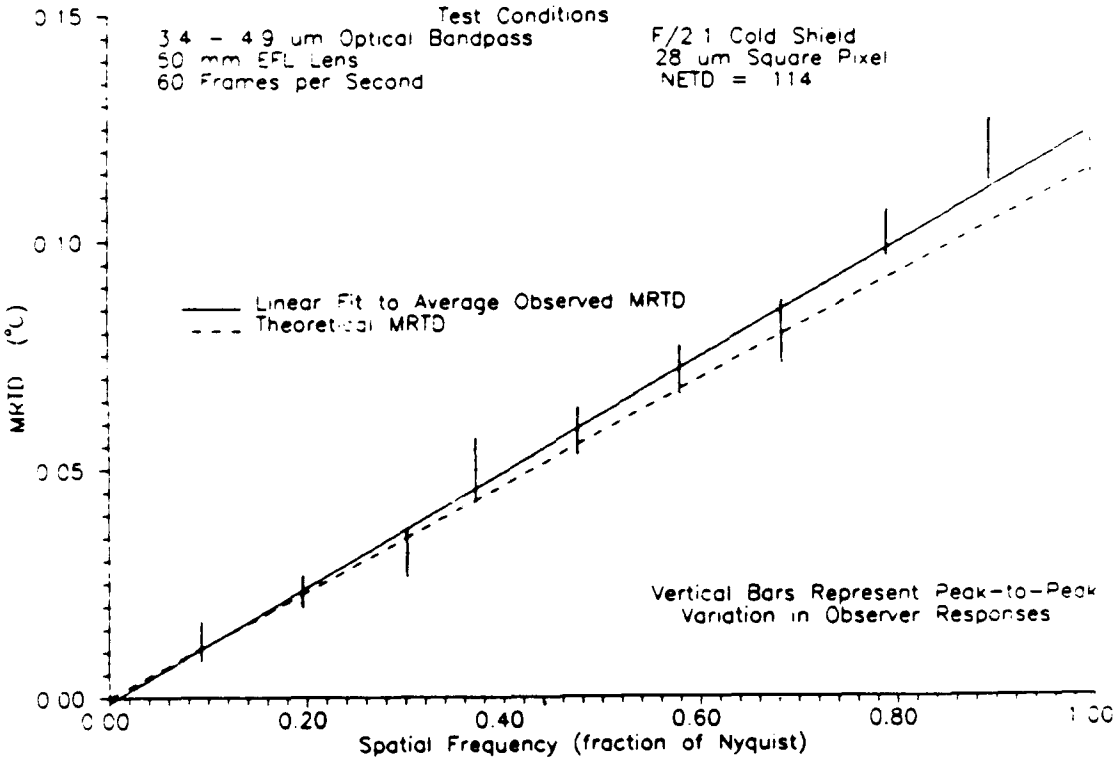

Figure 3.30
Averaged Minimum Resolvable Temperature Difference

between the predicted and measured data is excellent, strongly supporting Mooney's theory.

Clearly, the camera is very sensitive when operated with full nonuniformity correction. The observations of this section support the arguments of Chapter 2 that call for residual spatial noise levels well below the NETD.

Measurement of Temporal Stability

Allowing time for warm-up, an ideal infrared camera would produce the same output on a pixel-by-pixel basis, independent of time. Under nonuniformity correction, the correction terms would remain valid indefinitely. Perfect nonuniformity correction would be seen at the calibration points at all times following calibration.

The overall stability of a real infrared camera is determined by the properties of the imaging device as well as by the stability of the drive electronics and data acquisition system.

In the design of this camera system, many steps were taken to ensure good temporal stability. As mentioned earlier, the imaging device is temperature-controlled to better than 0.04°K peak-to-peak. The JFET preamplifiers internal to the dewar are temperature-controlled to the same level. External electronics were optimized to minimize drift. Having taken these precautions, it was assumed that measured stability would be limited only by the properties of the CRC-365.

Stability was tested under both illuminated and non-illuminated conditions, using the Electro-Optical Industries blackbody and a cooled dark slide, respectively. Data were taken by first forming a one-point correction in the nonuniformity corrector. Immediately thereafter, corrected data frames were read into the data acquisition system. Data frames were collected on a logarithmic time schedule. The mean and spatial variance were calculated upon receipt of each frame.

Both the mean and variance were plotted versus time. The variance readings were corrected for both quantization and temporal noise.

The results shown in Figures 3.31 and 3.32 represent typical performance, in the absence of illumination. To obtain these plots, the basic experiment was run several times. An ensemble average was formed across the individual runs. The average drift in the mean is plotted in Figure 3.31. This drift was essentially zero, for all observation times in the 2000 second interval shown.

The rms spatial noise increased slightly during the beginning of the observation period, and then leveled out near the end. This drift effect is shown in Figure 3.32. Comparing the data points at 1 and 2000 seconds, an R.S.S. increase of about 25 electrons is seen. In thermal imaging terms, this would correspond to an equivalent source nonuniformity of about 0.006°C. This equivalence assumes operation in the 3.4 - 4.9 μm band, near room temperature.

This type of plot was first reported by Scribner (Scribner, 1988). His method was designed to reveal 1/f noise in infrared detectors. The drift effects seen here are quite small, and are probably associated with the readout electronics, rather than the PtSi detectors themselves. This conclusion is supported by the appearance of the monitor at the end of the observation period. A very faint pattern of vertical stripes occasionally appeared in the picture, corresponding to the odd and even columns of the readout.

The tests performed under illumination yielded additional information. During these tests, the camera output was observed for an eight hour period following power-on. To investigate the warm-up process, a one-point correction was formed 15 minutes after application of power to the camera. This correction was used throughout the remainder of the test.

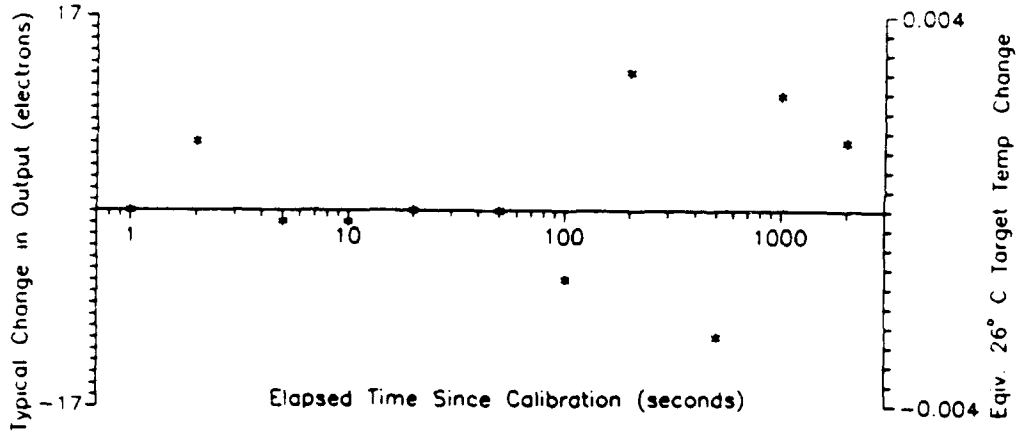

Figure 3.31
Temporal Stability of Mean Camera Output

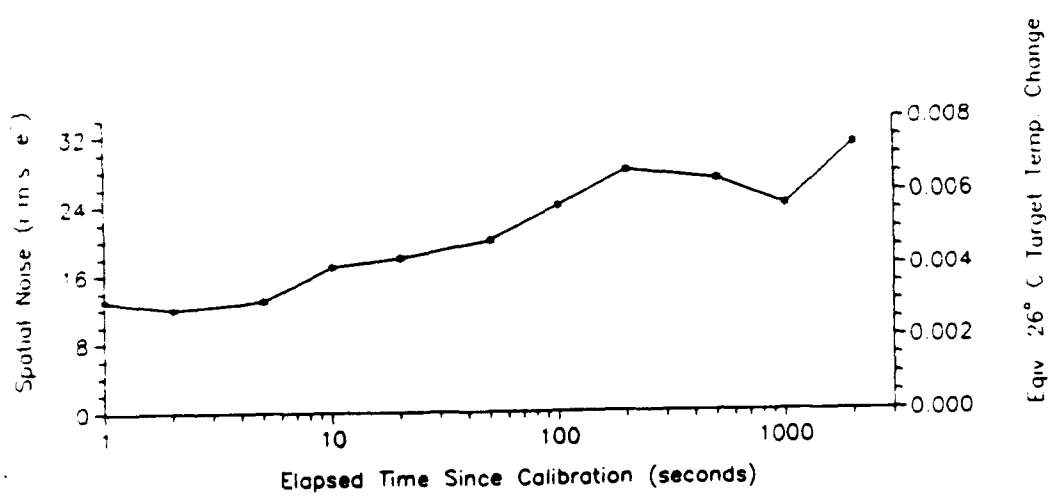

Figure 3.32
Temporal Stability of One-Point-Corrected Spatial Noise

After a period of one and one-half hours, the warm-up process was judged to be complete. During warm-up, the mean output changed by about 2 analog-to-digital units. During the remaining six and one-half hours, the mean output drifted only +0.70 analog-to-digital units. This corresponds to about 120 electrons, or an equivalent source temperature change of around 0.03°C, for the 3.4 - 4.9 μm band.

This small change in output might be entirely attributable to changes in the ambient radiation component that reflects off of the blackbody source plate. Recall that its emissivity is quoted at 99 percent, which indicates a reflectance of 1 percent. As the room temperature rises, the camera sees a slightly larger reflected radiation component from the room. A change of only 3°C in the room temperature could account for the observed drift. This type of problem makes long-term studies of camera stability difficult.

The net spatial noise that accrued during the complete warm-up period, i.e., from 15 minutes through one and one-half hours, was only 0.024°C, in equivalent source temperature units. No further increase was noted whatsoever during the following six and one-half hours.

In conclusion, these tests demonstrate that the camera requires a warm-up period of around one and one-half hours. When fully warmed up, small increases in spatial noise occur over roughly a five minute period following calibration. The tested device showed an increase in spatial noise of 0.006°C during this period, after which no appreciable change occured. These encouraging results show that the CRC-365 can maintain long periods of high sensitivity, without requiring recalibration.

Crosstalk Effects

During initial testing, an anomalous crosstalk effect was noted. The effect was first seen while viewing a high contrast bar target. The bar spatial frequency was around 5

percent of the Nyquist frequency, and the differential temperature was around 10°C to 15°C.

The appearance of the video monitor was similar to Figure 3.29, discussed in the section on MRTD. In addition to the bar images, dark stripes of equal width appeared above and below each bar, extending to the edges of the picture. These stripes run parallel to the slow axis of the readout device.

The mean value of the stripes was around 3 percent of the bar images, making them easily visible to the eye. The effect is most noticeable for regular geometric shapes, such as the bar target, that are superimposed on a uniform background. It is annoying to view on the monitor, and represents a potentially serious degradation to any computations performed on the image. No combination of bias settings could be found that lessen this effect.

This effect also was noted by personnel at the National Optical Astronomy Observatories. Britt and Fowler (Britt and Fowler, 1990) conducted an extensive test program to isolate the source of this problem. Their research revealed that several steps may be taken to lessen the amount of crosstalk seen in the CRC-365.

Several device problems were identified. Solid electrical bonding of the device to the package well, and to the associated leadless chip carrier contacts, was important. Additionally, the wire bond made to the common anode of the detector array must have low resistance. The physical origin of the effect is unknown. Shepherd has suggested that there may be a carrier-trapping process associated with the vertical columns of the readout device (Shepherd, 1991).

Improved devices were largely free of this troublesome defect. In these devices, better grounding to the imager and certain changes in the operating potentials reduce the crosstalk to an acceptable level.

Measurement of Device Saturation Limit

An estimate of the saturation limit was made during the transfer function measurements. This test revealed the output signal range over which the CRC-365 can be operated. The test was performed by focussing a high temperature blackbody signal on the device. The video output was viewed at the output of the JFET source-followers.

While observing the video waveform, the temperature of the blackbody was gradually increased. At a certain temperature, typically around 120°C, the output reached saturation. Beyond this point, no further changes in the video output were seen. No anomalous effects were noted, other than the crosstalk effect discussed in the previous section. These measurements, like those described in the transfer function section, were done with a V_{GG} setting of 0.75 Volts. Slightly different results may be obtained for higher V_{GG} values.

The output voltage was measured with respect to a reference level, established by blocking the dewar with aluminum foil. With the dewar blocked, the average signal was 38,700 electrons. When viewing the blackbody, the saturated output was 1.5 Volts below this dark reference level.

A conservative estimate of the saturation charge may be made by neglecting the de-biasing effects associated with the sense node capacitance. Using the zero-signal value of 0.089 picofarads, and an average gain value obtained from Eqs. (3.4) and (3.5), the blackbody signal is 1.17×10^6 electrons. Adding this to the reference level, the saturation charge is 1.21×10^6 electrons. Gates (Gates, 1988) reported values in the range 1.1 to 1.6 $\times 10^6$.

Measurement of Device Power Dissipation

Power dissipation is an important consideration when non-cryogenic cooling schemes are used. The power consumption of the CRC-365 was measured by observing the heater output of the Lakeshore Cryotronics temperature controller.

Before applying power to the camera, the temperature of the device was stabilized near 79°K. The heater power under these conditions was 26.6 milliwatts. After applying power to the imager, the heater power decreased to 8 milliwatts. It was assumed that all power dissipated by the device flows through the heated cold finger. This implies a device dissipation of 18.6 milliwatts.

This measurement was done for a V_{GG} setting of 0.75 Volts. Power dissipation increases in proportion to this control setting. By observing the DC current supplied to V_{DD}, the power dissipation was calculated for other V_{GG} values. The dissipation is 21.4 and 24.6 milliwatts for V_{GG} values of 0.85 Volts and 0.95 Volts, respectively.

Summary of Test Results

The highlights of these tests are presented in Table 3.3. Residual nonuniformity under two-point correction is low, and temporal stability is excellent. Three anomalous effects were noted, in the bandwidth, temporal noise, and crosstalk properties of the device. Final analysis of the nonuniformity tests follows in Chapter 4.

Table 3.3

Summary of Test Results

Test Conditions

Biasing as shown in Table 3.1	3.4 - 4.9 μm bandpass
F/2.1 Cold Stop	Optical Transmission = 0.85
Device Temperature = 79°K	Blackbody Emissivity = 0.99

Test Results

Gain from detector to output	0.75
Offset from detector to output	-1.6 Volts
Dark charge per detector	20,000 e^-/cycle
Thermal barrier height	0.20 eV
Dark charge nonuniformity	4% rms
Intrinsic Schottky barrier height	0.250 eV
Schottky barrier under bias	0.236 eV
300 Kelvin signal response	116,000 e^-
300 Kelvin contrast	4200 e^-/°K
300 Kelvin NETD	0.10°K
Schottky quantum yield under bias	0.19 eV^{-1}
Sense node capacitance	0.09 pF
"Slope" nonuniformity, all pixels	1.1% rms
MRTD at Nyquist frequency	0.13°K
Saturation charge	1.2 x 10^6 e^-
Power dissipation	20 mW
Anomalous behavior noted	Bandwidth
	Temporal Noise
	Crosstalk

CHAPTER 4

INTERPRETATION OF NONUNIFORMITY TEST RESULTS

The initial test results of Chapter 3 suggest that overall nonuniformity performance of the CRC-365 is very good. To further investigate the nonuniformity performance, the results of Chapter 3 will be examined in the context of the material developed in Chapter 2.

Using the uncorrected test results, it will be shown that uncorrected nonuniformity is almost entirely attributable to the readout device. The results obtained under one-point correction demonstrate that the levels of slope-type nonuniformities and spectral nonuniformity are low. Analysis of the two-point-corrected results indicates that the basic technology used in the CRC-365 is capable of producing excellent performance, but that its bandwidth limitations prevent it from achieving the fundamental performance limits investigated in Chapter 2. Recall that these bandwidth limitations were highlighted earlier in Figure 3.26. An architectural defect in the design of the device further limits the two-point-corrected performance observed in its even-numbered columns.

Discussion of Uncorrected Spatial Noise

Recall that Figures 3.19 and 3.20 illustrate the uncorrected spatial noise of the device. The most striking feature of the noise is that it appears to be nearly independent of the background temperature.

At a background temperature of 27°C, a typical group of pixels exhibits slightly less than 35 rms ADUs of spatial noise. Using contrast and conversion gain values of 4200 electrons per degree and 165 electrons per ADU, respectively, this noise level has a temperature equivalent of about 1.3°C. This is 100 times worse than the performance goals discussed for corrected imaging.

Recall that Figures 1.1 and 3.28 illustrate an uncorrected image of a bar pattern that is just visible above the spatial noise. The differential temperature used for these photographs was 3°C. The pattern cannot be resolved below about 1°C.

Using a least-squares method, the mean value curve for each group of pixels (not shown) was extrapolated back to the zero-signal intercept. By examining the mean values for each of the eight groups of pixels, it was observed that the device exhibits a large DC offset between adjacent rows. The row-to-row offset is 160 ADUs for the odd columns, and 150 ADUs for the even columns. This corresponds to about 45 millivolts, referred to the source-follower inputs. The origin of this effect is unknown. It is possible that periodic nonuniformity effects such as this are traceable to physical misalignments of the step-and-repeat hardware used in the fabrication of the readout device.

This offset is entirely responsible for the total noise curve shown in Figure 3.20, and explains the alternating dark and light horizontal line pattern seen in the monitor photographs. The total noise is about 80 ADUs, corresponding to an equivalent source nonuniformity of 3°C. This periodic type of spatial noise was an unexpected result, and was not featured in the analysis of Chapter 2.

Again using a least-squares method, the noise curves of Figure 3.20 were extrapolated back to the dark charge level. Within typical pixel groups, the rms variation in output is about 31 ADUs. Recall that the nominal dark charge is 20,000 electrons, with an rms nonuniformity of about 850 electrons. After scaling, this dark charge nonuniformity corresponds to 5 ADUs. Clearly, dark charge nonuniformity is much less than the additive nonuniformity effects attributable to the readout device. Offset variations in the readout device dominate the uncorrected spatial noise.

Referred to the amplifier inputs, this variation in offset corresponds to about 9 millivolts rms. Equation (2.67) shows that these variations may be explained by small fluctuations in various amplifier material and fabrication parameters.

The results of Table 2.21 may be used to estimate upper bounds for several sources of amplifier nonuniformity. Recall that the most undesirable amplifier nonuniformity terms are the threshold voltage, gate oxide thickness, and impurity concentration. Simple calculations indicate rms variations of no worse than 1.5 percent for the threshold voltage and oxide thickness, and no worse than 6 percent for the impurity concentration. By this estimate, the readout device essentially meets three of the six most important tolerance limits derived in Chapter 2.

It has been shown that offset variations in the readout device dominate the uncorrected spatial noise, making the total output noise virtually independent of background temperature. Offset variations within sister-pixel groups are small, in the context of the amplifier analysis of Chapter 2. This indicates exceedingly good control of material and processing parameters during fabrication of the readout device. An unexpected periodic nonuniformity effect was identified, consisting of a large row-to-row offset.

Discussion of Spatial Noise Under One-Point Correction

Recall that Figures 3.21 through 3.25 document the spatial noise measured under one-point correction. The general appearance of these curves is consistent with the material of Chapter 2. The overall post-correction nonuniformity is around 1 percent of the mean, again suggesting that tight manufacturing tolerances were maintained during device fabrication.

In this section, the measured performance of Figure 3.25 will be used to establish the amount of various types of nonuniformity present. These estimates are used in the next

section to predict the worst-case theoretical performance limit of the tested device, under two-point correction.

These nonuniformity estimates were made by comparing the test results to various simulations of nonuniformity effects. The iterative software routines of Chapter 2 were used again for these simulations. Recall that these routines were used to generate Tables 2.11 and 2.14. For present purposes, the measured device parameters of Table 3.3 were substituted for the hypothetical values used in Chapter 2. In this way, the simulation program closely approximates the actual performance of the tested device.

To obtain a reasonable match between the observed and simulated camera outputs, two other changes were required. To account for the difference between measured and theoretical sense node capacitance values, the amplifier input capacitance, C_{gate}, was increased from 0.06 to 0.077 picofarads.

To account for an offset difference between the program and the measured output, it was necessary to add about 7600 electrons to the simulated output. With these changes in place, the simulation and actual camera output differ by less than 0.25 percent rms, when compared on a photocharge basis. Sample program outputs and actual data are provided in Table 4.1.

Five sources of output nonuniformity were estimated, including the initial quantum yield, detector active area, intrinsic barrier height, amplifier input capacitance, and amplifier gain. Recall that spatial nonuniformities in these quantities, exclusive of the amplifier gain, were previously identified as the most important contributors to residual spatial noise under two-point correction.

For each source of nonuniformity, the quantity under investigation was perturbed by 2 percent, with the exception of the barrier height, which was perturbed by 0.25 percent.. The perturbed outputs were then one-point corrected by the nominal simulated

Table 4.1

Results of Camera Simulation

Background Temp. in °C	Actual Output in Electrons	Simulated Output in Electrons
17	100,556	100,573
21	113,289	113,558
25	128,015	128,433
29	144,847	145,404
33	164,069	164,690
37	186,038	186,522
41	210,753	211,142
45	238,756	238,804
49	270,214	269,772
53	305,147	304,317

output. These results are shown in Figures 4.1 through 4.3. Note that the final output of the simulation program of Chapter 2 is in volts; the results shown in these figures were scaled to analog-to-digital units by multiplying by the system gain.

Figure 4.1 shows the effect of 2 percent variations in the quantum yield and detector active area. At full scale, a 2 percent variation in the quantum yield produces a 1.9 percent output nonuniformity. The impact of active area variations is somewhat less. Changes in the active area of the detector are partially compensated by attendant changes in its capacitance.

Figure 4.2 shows the effect of 2 percent variations in the amplifier gain and input capacitance. For the amplifier gain, a given amount of nonuniformity produces the same amount of output nonuniformity. The impact of nonuniformity in the amplifier input capacitance is moderated by the fixed detector capacitance appearing in parallel with it. In this case, a 2 percent nonuniformity produces about 1.5 percent of output nonuniformity.

Figure 4.3 illustrates the effect of 0.25 percent variations in the barrier height. At full scale, this level of nonuniformity produces about 2 percent output nonuniformity.

Each of the curves shown in Figures 4.1 through 4.3 were compared to the measured nonuniformity of Figure 3.25. The measured data was divided by the simulation data, at 4°C intervals. The average ratio between the curves under comparison then was multiplied by the nonuniformity level represented by the simulated curve. This result is the upper bound on the amount of nonuniformity present in the tested device.

Table 4.2 summarizes these results. Recall that the analysis of Chapter 2 concluded that 1 percent manufacturing tolerances are required for the quantum yield, active area, and input capacitance. The estimated nonuniformity in each of these quantities is within this tolerance limit. In the case of the barrier height, a nonuniformity level of 0.05 percent was

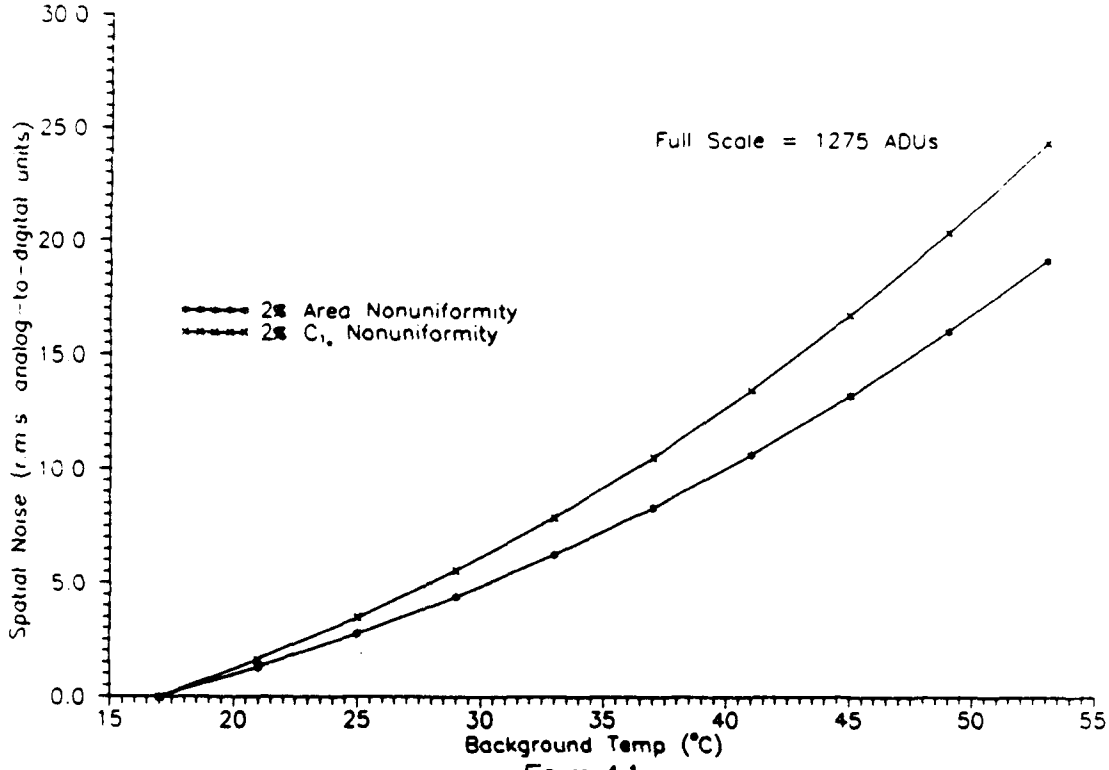

Figure 4.1
Simulated Spatial Noise Under One-Point Correction For
2 Percent Active Area or Quantum Yield Nonuniformity

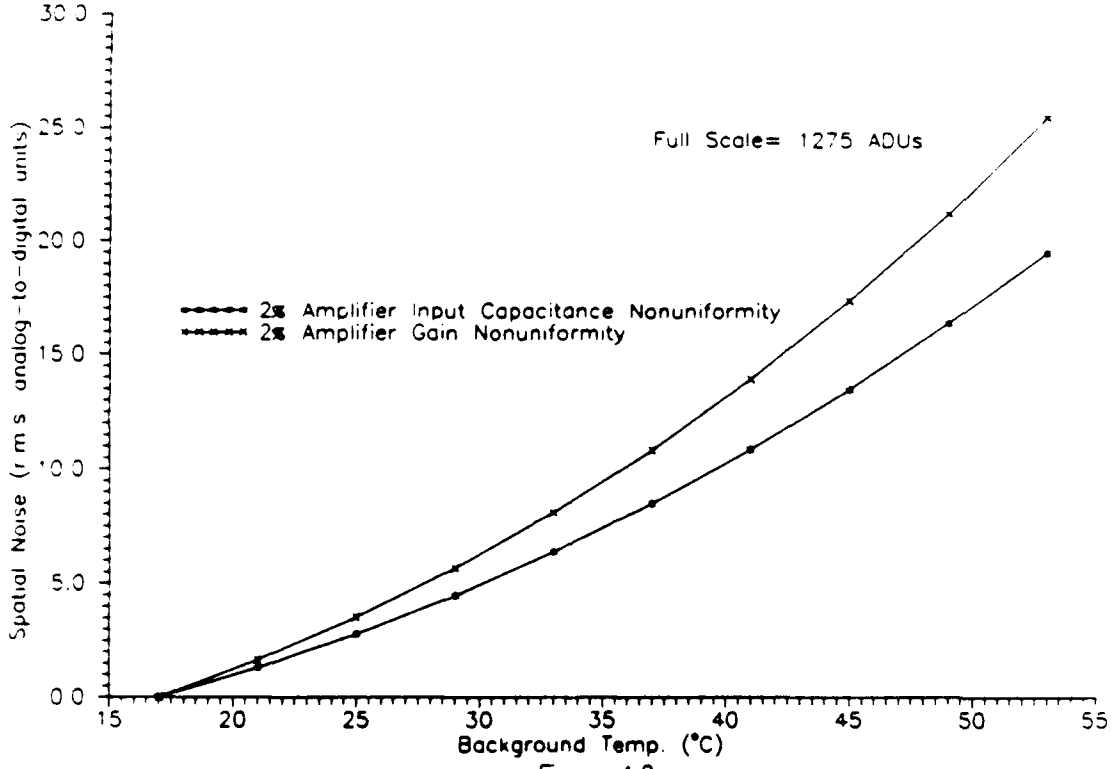

Figure 4.2
Simulated Spatial Noise Under One-Point Correction For 2 Percent Amplifier Gain or Input Capacitance Nonuniformity

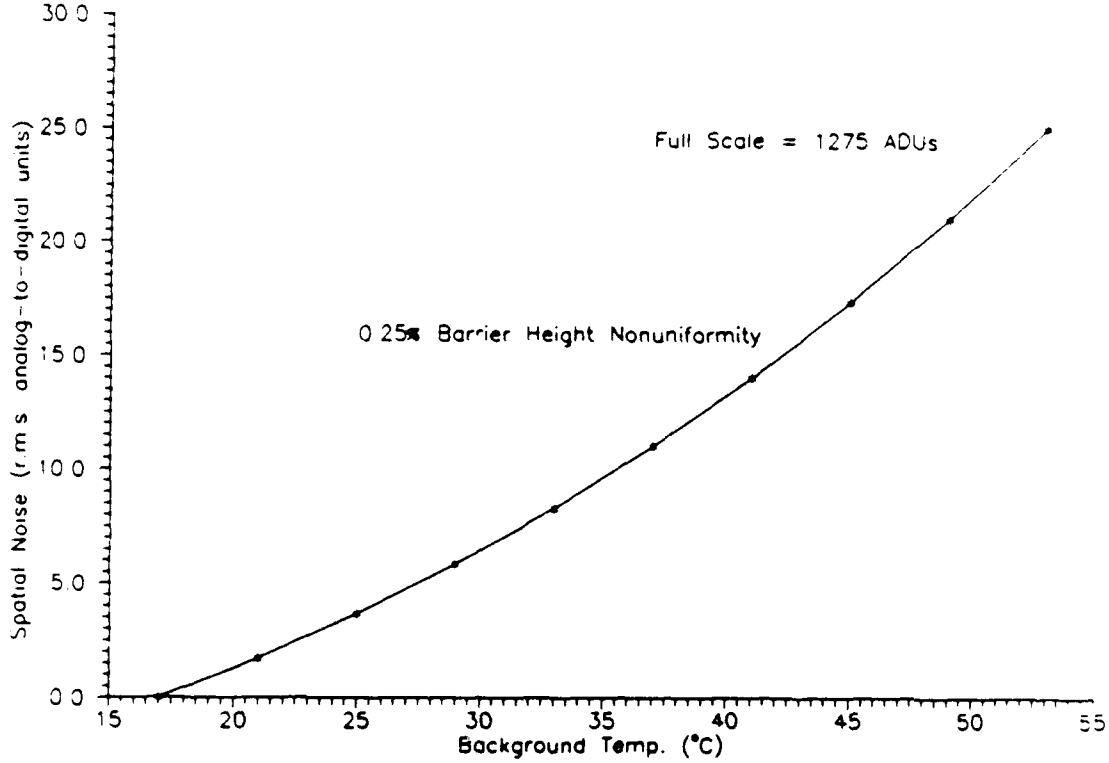

Figure 4.3
Simulated Spatial Noise Under One-Point Correction
For 0.25% Barrier Height Nonuniformity

Table 4.2

Estimated Detector and Readout Nonuniformity

Quantity	Estimated RMS Nonuniformity (Upper Bound, Within Sister-Pixel Groups)
Intrinsic barrier height, ψ_o	0.08%
Amplifier gain, A_v	0.65%
Initial quantum yield, C_{lo}	0.70%
Amplifier input capacitance, C_{gate}	0.85%
Detector active area, A	0.85%

quoted as a fabrication goal. Bearing in mind that the 0.08 percent estimated value is an upper bound, the barrier height also may be within tolerance limits.

It is important to remember that the results of Table 4.2 apply to typical sister-pixel groups. When considering the nonuniformity across all pixels, periodic variations in the readout electronics further degrade the spatial noise. Figure 3.24 shows that the total spatial noise exceeds that of the individual groups.

In the discussion of uncorrected nonuniformity, it was shown that a periodic offset variation in the readout device dominates the total spatial noise. Under one-point correction, these offset differences are entirely removed, but small periodic gain differences persist across sister-pixel groups. This was discovered by examining the mean values associated with the eight sister-pixel groups. These periodic gain differences explain why the total noise of Figure 3.24 exceeds that of individual sister-pixel groups.

Table 4.2 shows that within sister-pixel groups, the amplifier gain nonuniformity is controlled to better than 0.65 percent. The variation in gain across sister-pixel groups, however, is about 1.1 percent. Note that the monitor photograph of Figure 3.22 has a regular geometric pattern associated with this periodic spatial noise.

In this discussion of the spatial noise under one-point correction, it has been shown that the levels of nonuniformity associated with the detector array and the amplifier input circuit are quite low, meeting the manufacturing goals developed in Chapter 2. The presence of periodic gain differences in the readout electronics somewhat degrade the overall spatial noise, and produce a pronounced grid pattern on the monitor output at higher signal levels. This was an unexpected result which was not featured in the analysis of Chapter 2

Discussion of Spatial Noise Under Two-Point Correction

The spatial noise under two-point correction has been used throughout this work as a measure of imaging device performance. In this section, the nonlinear simulation results of the previous section will be used to predict the theoretical performance limit of the tested device, when operating under two-point correction. The actual corrected spatial noise of the device will be compared to this theoretical goal.

In the previous section, simulations and test data were used to estimate the relative amounts of nonuniformity in five spatial variables. According to the nonlinear theory of Chapter 2, only the amplifier gain variations are totally removed by two-point correction.

Consider the remaining four sources of nonuniformity. Under two-point correction, equal spatial variations in active area, quantum yield or amplifier gate capacitance produce essentially the same amount of residual spatial noise. The same level of barrier height nonuniformity produces much larger residual errors.

To obtain a theoretical prediction of the impact of these two classes of nonuniformity on the tested device, the active area and barrier height simulations of the previous section were re-examined. Recall that in the previous section the nominal program variables were perturbed by 2 percent and 0.25 percent, respectively. The resulting output versus background curves then were one-point corrected by the nominal program output.

For present purposes, these same output versus background curves were two-point corrected, the results of which are shown in Figure 4.4. These curves represent the predicted two-point corrected spatial noise that would be produced by the specific device under test, if the hypothetical amounts of nonuniformity shown were present.

Before continuing, it is reasonable to compare these predictions to those of Chapter 2. In the hypothetical device of Chapter 2, a 50°C operating range was considered. At

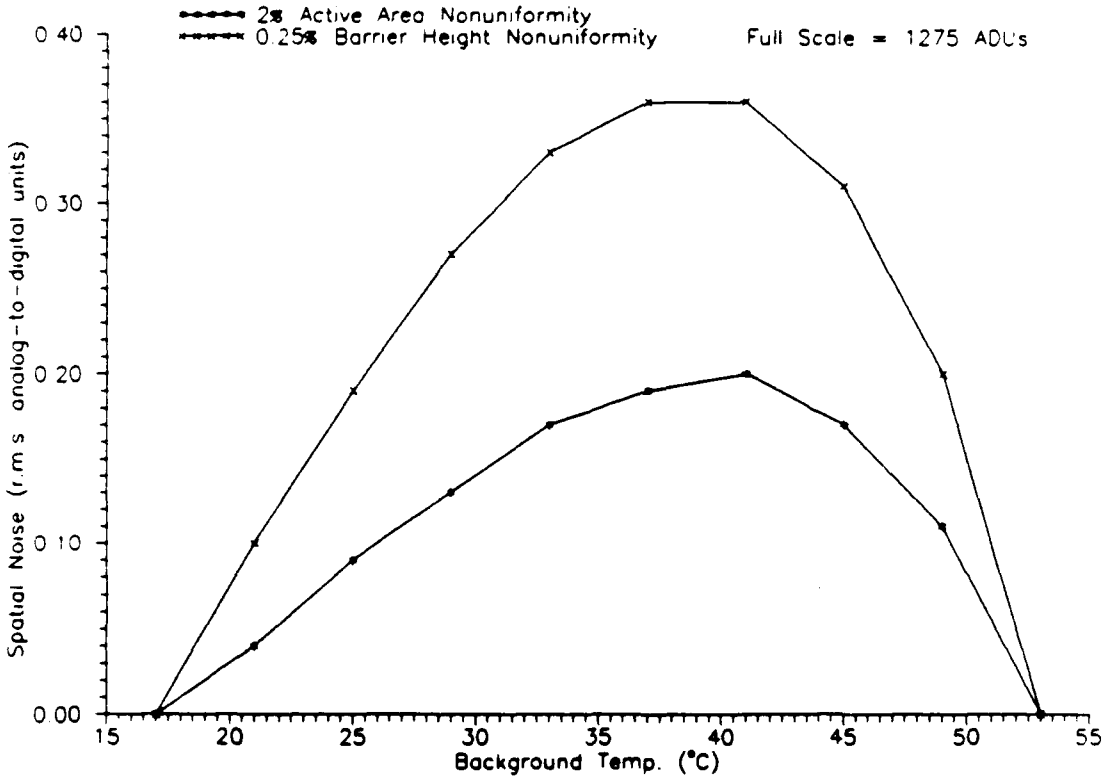

Figure 4.4
Simulated Spatial Noise Under Two-Point Correction For
2% Active Area or 0.25% Barrier Height Nonuniformity

mid-scale, residual spatial noise for active area and barrier height nonuniformities was 0.013°C and 0.029°C rms, respectively.

For comparison, the results of Figure 4.4 may be scaled to temperature units by noting that the contrast and conversion gain at mid-scale are 5100 electrons per degree, and 162 electrons per ADU. The residual spatial noise values at mid-scale are thus about 0.005°C and 0.010°C rms.

These values are considerably smaller than those predicted in Chapter 2. The differences are due to a smaller operating temperature range, and a measured photoresponse that is weaker than the hypothetical device. In essence, the detectors of the hypothetical device of Chapter 2 are operated over a larger voltage range, with correspondingly greater nonlinearity effects.

To determine the worst-case theoretical performance limit for the tested device, the results shown in Table 4.2 were used. For each entry in this table, the results of Figure 4.4 were linearly scaled to predict new residual spatial noise curves. This was done as if only the particular nonuniformity source in question were present.

Not surprisingly, if barrier height variations were responsible for all of the measured output nonuniformity under one-point correction, then the post-correction spatial noise under two-point correction would be maximized. This residual noise curve is plotted in Figure 4.5, and represents the worst-case theoretical performance limit of the tested device. Note, also, that the best observed performance, shown previously in Figure 3.27, is provided for direct comparison. Recall that this curve corresponds to the odd columns of the array.

Examining the theoretical curve first, note that after scaling, the residual spatial noise at 33°C corresponds to only 0.0035°C rms, an exceedingly low amount of residual noise.

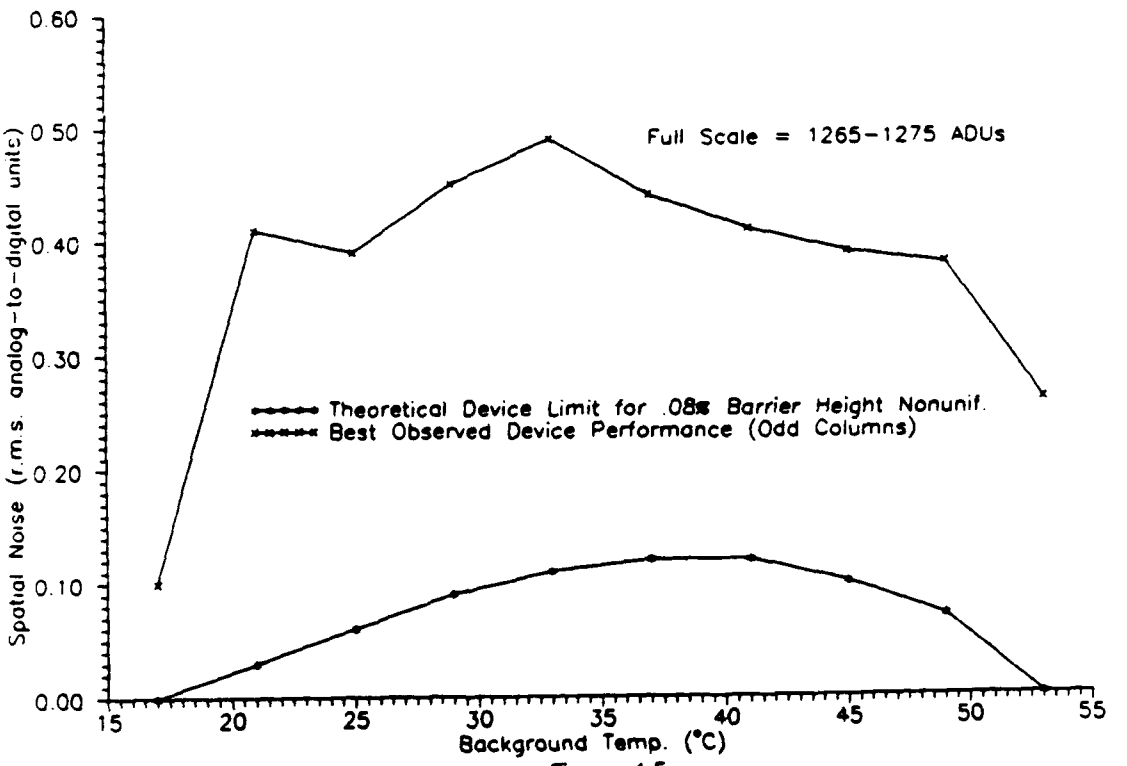

Figure 4.5
Measured and Simulated Spatial Noise Under Two-Point Correction

If we acknowledge that some drift always will be present, then this figure is a bit optimistic. Based on the test results of Chapter 3, one might allow a spatial noise increase as high as 0.005°C rms to account for temporal instability. In this case, the total spatial noise over time might be as high as 0.006°C rms.

Now examining the measured performance at 33°C, note that the spatial noise is about 0.5 ADUs rms, corresponding to an equivalent source nonuniformity of 0.015°C. The observed performance is about three times worse than the estimated theoretical performance limit.

The most likely cause for this discrepancy is the same problem that limits the performance of the even columns. Recall that the even columns appear to suffer from bandwidth limitations. No matter how high the column bias current is set, pixels from the even-numbered columns never approach the performance seen in the odd pixels. This was illustrated previously in Figures 3.26 and 3.27. It is highly likely that layout-related effects are responsible for higher distributed capacitances along the even columns.

Upon close examination of the data used to plot Figure 3.26, the odd, or best-performing, outputs never really stop improving either, as the bandwidth is increased. As noted in Chapter 2, newer versions of the CRC-365 have included extra drive transistors at the end of each column of the readout. Testing of these devices, under similar conditions, would reveal the extent to which these bandwidth problems have been remedied.

To view the performance from another perspective, the entire data set of Figure 3.27 was scaled to source-equivalent units, using appropriate contrast and conversion gain constants at each data point. These scaled results are shown in Figure 4.6, with the noise-equivalent temperature difference.

From this point of view, the measured performance looks very good. Consider first the performance of the odd columns. At no point in the 40°C operating range does the

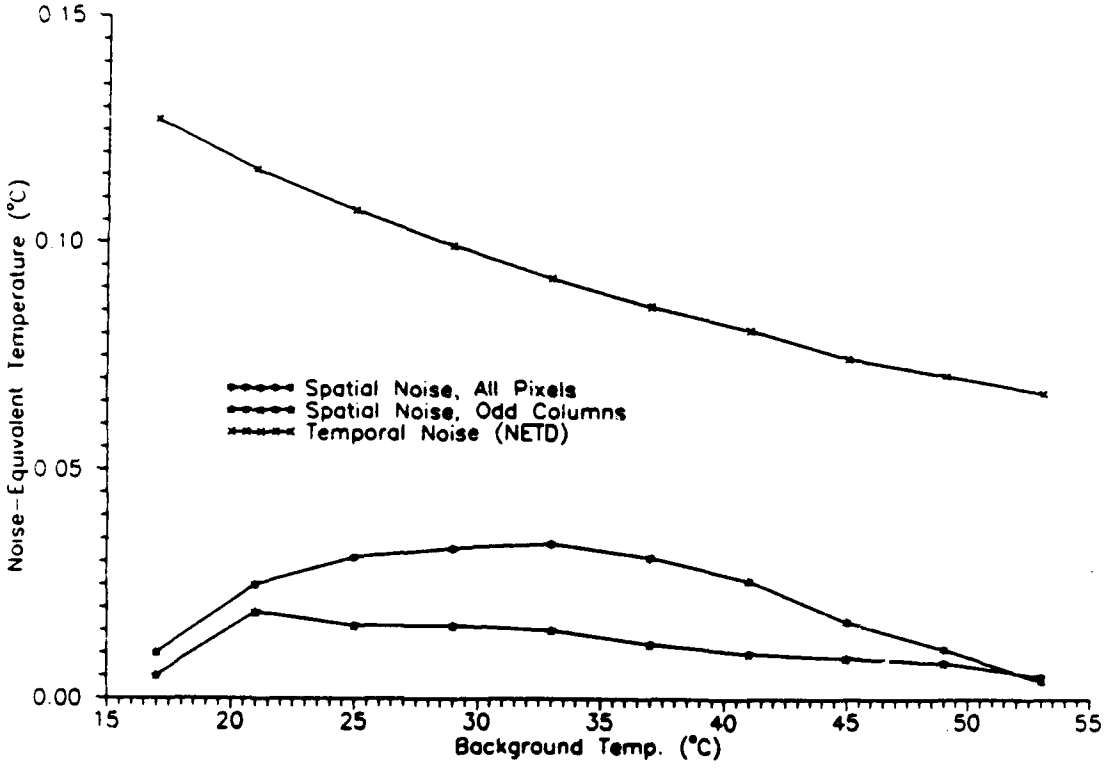

Figure 4.6
Measured Spatial Noise Under Two-Point Correction and NETD

spatial noise exceed 0.020°C rms. Expressed as a percentage of the NETD, the spatial noise never exceeds 16 percent. If one considers all pixels, including those of the even columns, the residual spatial noise never exceeds about 0.035°C, and 37 percent of the NETD.

The figures and discussion of this section show that the basic technology used in the CRC-365 is at a high level of maturity. Ignoring a column-to-column architectural flaw specific to the CRC-365 itself, it may be concluded that the general approach of hybridizing PtSi detectors to an array of source-follower transistors is very sound. In its best performance (pixels in odd columns), the tested device comes within a factor of three of meeting the fundamental limitations on spatial noise predicted by the nonlinear theory of Chapter 2.

Summary of Nonuniformity Results

Summarizing the findings of this chapter, it has been shown that the CRC-365 has been fabricated carefully, exhibiting very low spatial spread in various manufacturing variables. Periodic nonuniformity effects were discovered in the uncorrected and one-point corrected output, representing an unexpected feature not considered in the theoretical analysis of Chapter 2. Under the two-point correction, it comes close to theoretically calculated performance limits, at least in the outputs from its odd columns. Rather than being limited by nonlinearity brought about through de-biasing, the CRC-365 is limited by bandwidth effects, which presumably have been, or will be, corrected in later generation devices. Only in improved devices will nonlinearity and drift issues become dominating factors in the post-correction spatial noise. Nonlinearity will only be an issue when the operating temperature range and thermal response are large.

CHAPTER 5

DETECTOR ARRAY FIGURES OF MERIT

In previous chapters, the impact of nonuniformity in PtSi imaging devices was examined in detail. In this final chapter, a more general analysis of nonuniformity effects will be considered.

To simplify the analysis and design of detection systems, there have been many efforts to create compact figures of merit that adequately describe the detectors themselves. The most widely used figure is the specific detectivity, or D*. This figure-of-merit is used for single-detector systems, in which spatial nonuniformity is not an issue. At present, there is no universally accepted equivalent for two-dimensional detector arrays.

In the following material, the standard D* figure-of-merit will be modified for focal plane array use. A theoretical representation of this focal plane array test will be developed. This result will be used to derive a system figure-of-merit, called the contrast signal-to-noise ratio.

Derivation of 2-D*

In this section, a new figure-of-merit called 2-D* will be developed, for use in focal plane array characterization. This is not offered so much as a working figure-of-merit, but more as a conceptual link between single-detector and focal plane based systems. This work was motivated by a discussion of Contrast Signal-to-Noise Ratio that appeared in an article by Mooney (Mooney, 1989). Some of his concepts and notations appear in the following material.

To begin this discussion, the standard D* measurement will be introduced. Then it will be rewritten for photon units and the inclusion of spatial noise. A simple model

describing focal plane array operation will be introduced. This model will be used to derive a theoretical estimate of the 2-D* expected in actual testing. These calculations reveal several interesting features and limitations of focal plane array performance.

Specific detectivity, or D* was first introduced by Jones (Jones, 1959). An appropriate D* expression for this analysis is given by Dereniak (Dereniak, 1984). Note that D* may be thought of as the signal-to-nose ratio obtained in a one Hertz bandwidth, when one watt of optical power is placed on a detector of unit area.

$$D^* = \frac{SNR}{\Phi_e^s}\sqrt{A\Delta f} \tag{5.1}$$

In this expression, A is the active area in square centimeters, Δf is the noise-equivalent bandwidth, and Φ_e^s is the optical power of a monochromatic test signal. The units for D* are cm $Hz^{1/2}$ $Watt^{-1}$. Higher D* values indicate better performance.

This relationship is used to calculate the D* of an actual detector under test. During the measurement, the signal response, rms temporal noise, noise bandwidth, and detector active area must be recorded. The optical power applied to the detector must be known, either through separate measurements or calculations.

The data values are substituted into Eq. (5.1) to solve for the D*. The background irradiance and chopping frequency must also be reported with the calculated D* value.

For focal plane array analysis, it is convenient to work in photon units rather than watts. To express the optical signal in photons per second, the following conversion factor is used.

$$\Phi_e^s = \Phi_p^s\left(\frac{hc}{\lambda}\right) \tag{5.2}$$

Recall that h is Planck's constant and c is the speed to light. The wavelength of the optical signal is λ. The term Φ_p^s is the signal flux in photons per second.

The D* expression was originally conceived for detectors operating on a continuous current basis. To account for the fact that most focal plane arrays employ integrating detectors, Δf is replaced by the noise-equivalent bandwidth of a gated integrator. The term t_{int} is the optical integration time.

$$\Delta f = \frac{1}{2t_{int}} \tag{5.3}$$

After substituting Eqs. (5.2) and (5.3) into Eq. (5.1), the following equivalent D* expression is obtained.

$$D^* = \frac{SNR\,\lambda}{\Phi_p^s\, hc}\left(\frac{A}{2t_{int}}\right)^{\frac{1}{2}} \tag{5.4}$$

To use this expression for a focal plane array, the signal-to-noise ratio must include both temporal and spatial noise. To illustrate why, consider a typical system problem in which a point source is to be detected. In this hypothetical problem, the point source must be detected in a single frame of data.

The presence of the point source is detected when it is observed that a particular detector's output exceeds that of its neighbors by a specified amount. Even in the absence of the point source, the output of each detector differs slightly. Assuming a perfectly uniform background, these variations are due to detector nonuniformity. To be detected, the signal from the point source must clearly exceed the rms value of this spatial noise. Let the measured value for this nonuniformity be σ^s.

On a frame-by-frame basis, the various detector outputs also differ due to shot noise and read noise. Let the measured value of this noise be σ^t.

Looking across all of the detector outputs, a frame of data is thus degraded by two independent noise sources. To combine these sources, the R.S.S. approach is appropriate. Let the total measured noise be represented by σ^{tot}.

$$\sigma^{tot} = \left[(\sigma^s)^2 + (\sigma^t)^2\right]^{\frac{1}{2}} \tag{5.5}$$

To detect weak sources, the total noise must be kept to an absolute minimum.

Referring again to Eq. (5.4), and letting the measured signal response be S, the D* may be calculated from test data as shown. The expression is now referred to as 2-D*, to distinguish it from the single-detector figure-of-merit.

$$2\text{-}D^* = \frac{S\,\lambda}{\Phi_p^s\, hc\, \sigma^{tot}} \left(\frac{A}{2t_{int}}\right)^{\frac{1}{2}} \tag{5.6}$$

Consider now the 2-D* which is predicted by theory. To calculate the 2-D*, a simple model for focal plane array operation must be developed.

Each detector in the focal plane array shall be characterized by a spectrally flat quantum efficiency, η_{ij} and an active area A_{ij}. At the end of an integration period of length t_{int}, N_{ij} electrons appear across the detector.

$$N_{ij} = \bar{E}_p^b\, \eta_{ij}\, A_{ij}\, t_{int} \tag{5.7}$$

Note that dark charge is not featured in this expression, under the assumption of proper device cooling. The term $\widetilde{E}_p^b$ represents a spatially uniform background irradiance present at the detector. The irradiance is calculated as shown.

$$\widetilde{E}_p = \widetilde{L}_p^b \, \Omega \, \tau_{eff} \tag{5.8}$$

The term $\widetilde{L}_p^b$ is the radiance of the background. The projected solid angle subtended by the detector, as seen from the exit pupil, is represented by Ω. The effective optical transmission is τ_{eff}.

Due to the uncertainty associated with the emission process, the time-averaged value of $\widetilde{E}_p^b$ varies from one integration period to the next. The mean value of the irradiance over many integration cycles shall be represented by E_p^b. Considering all detectors in the focal plane array, the spatial and temporal average output is as shown.

$$N = E_p^b \, \eta \, A \, t_{int} \tag{5.9}$$

Note that the subscripts on η_{ij} and A_{ij} have been dropped, indicating spatially averaged values.

By assuming Poisson statistics and referring the read noise, σ_R, to the detector, the rms fluctuation in output, σ_N^i, is as follows.

$$\sigma_N^i = \left(E_p^b \, \eta \, A \, t_{int} + \sigma_R^2\right)^{\frac{1}{2}} \tag{5.10}$$

These temporal noise terms combine in R.S.S. fashion by assumption of statistical independence.

The spatial nonuniformity in the output is related to the individual levels of nonuniformity in η_{ij} and A_{ij}. The output nonuniformity shall be expressed as a fraction of the average photoresponse. Letting σ_N^s represent the spatial noise in electrons, the nonuniformity, U, is given by the following.

$$U = \frac{\sigma^s}{E_p^b \eta A t_{int}} \tag{5.11}$$

Rearranging terms, the following expression will be used in subsequent calculations involving the spatial noise.

$$\sigma_N^s = U E_p^b \eta A t_{int} \tag{5.12}$$

Equations (5.7) through (5.12) constitute the camera model used throughout the remainder of this discussion.

By taking the average point-source response to be $\Phi_p^s \eta t_{int}$, and combining Eqs. (5.10) and (5.12) as shown in Eq. (5.5), the measured signal-to-noise ratio may be estimated.

$$SNR = \frac{\Phi_p^s \eta t_{int}}{\left[E_p^b \eta A t_{int} + \sigma_R^2 + U^2 \left(E_p^b \eta A t_{int}\right)^2\right]^{\frac{1}{2}}} \tag{5.13}$$

This signal-to-noise ratio is a valuable result in itself, and shall be re-examined later. Upon substituting this expression into Eq. (5.6), a theoretical prediction of the actual 2-D* is obtained.

$$2\text{-}D^* = \frac{\lambda}{hc}\left[\frac{\eta}{2\left(E_p^b + \frac{\sigma_R^2}{\eta A t_{int}} + U^2 (E_p^b)^2 \eta A t_{int}\right)}\right]^{\frac{1}{2}} \tag{5.14}$$

A quick look at this result shows that it is not entirely independent of the detector area or bandwidth, as was desired. This indicates that these quantities also must be reported if one performs a 2-D* test.

Commercial manufacturers of detectors have adopted the practice of specifying D* for a 300°K background and hemispherical cold shield angle, plotting the D* as a function of wavelength. If the detector is tested with less than a hemispherical cold shield angle, the F/# used at test time is specified. To understand how a plot of 2-D* differs from a normal D* plot, consider a simple example.

A hypothetical focal plane array is to be operated with a lossless F/2 optical system. The bandpass is defined by a 3.5 to 5.5 μm filter. The detectors have an average quantum efficiency and active area of 0.2 percent and $(28\ \mu m)^2$, respectively. The detectors operate with a 1/60 second integration time and suffer a read noise of 100 electrons rms.

When viewing a 300°K background, the irradiance at the detectors is about 1.5×10^{15} photons per square centimeter per second. Making the required substitutions into Eq. (5.14), the curves shown in Figure 5.1 are obtained. In this figure, several different levels of nonuniformity are featured. Recall that Eq. (5.7) shows that this output nonuniformity is due to spatial variations in the quantum efficiency and active area.

The uppermost curve represents a perfectly uniform focal plane array. No spatial noise is present across the output, and the temporal noise is dominated by the shot noise associated with the background. This is referred to as background-limited photodetection. This is the only curve typically used to specify the performance of a single detector.

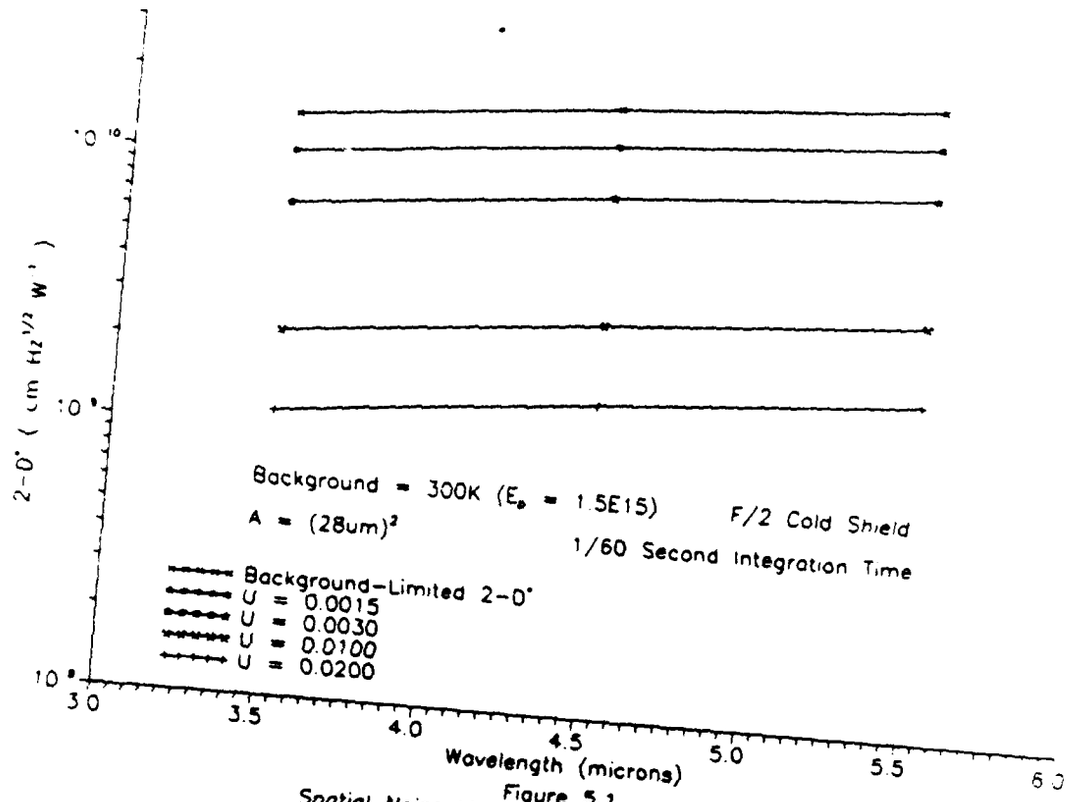

Figure 5.1
Spatial Noise Limited 2-D* Versus Wavelength

The remaining curves represent increasing levels of nonuniformity, to a maximum of 2 percent. At the 2 percent level, the sensitivity of the camera has been reduced by almost a factor of ten below the background-limited case. At the 0.15 percent level, the 2-D* is reduced by c.ly a factor of $(1/2)^{1/2}$. This is the level at which spatial-noise limited operation begins.

By plotting the 2-D* as a function of background irradiance, further information may be obtained. This plot is shown in Figure 5.2, for a nonuniformity level of 0.1 percent. By using log-log axes, it may be seen that the focal plane array has three distinct regions of operation. The existence of these three regions is consistent with the findings of a number of other researchers (Cantella, 1982; Blouke and Janesick, 1987; Mooney and Shepherd, 1989a).

The 2-D* expression of Eq. (5.14) indicates that the read noise becomes dominant under low-background conditions. The approximate background level at which read noise limited behavior begins is given by the following.

$$E_p^b < \frac{\sigma_R^2}{\eta A t_{int}} \tag{5.15}$$

Operation in this region is further described by the read noise limited 2-D* and signal-to-noise ratio.

$$2\text{-}D^* \approx \frac{\lambda \eta}{hc \sigma_R} \sqrt{\frac{A t_{int}}{2}} \tag{5.16}$$

$$SNR \approx \frac{\Phi_p^s \eta t_{int}}{\sigma_R} \tag{5.17}$$

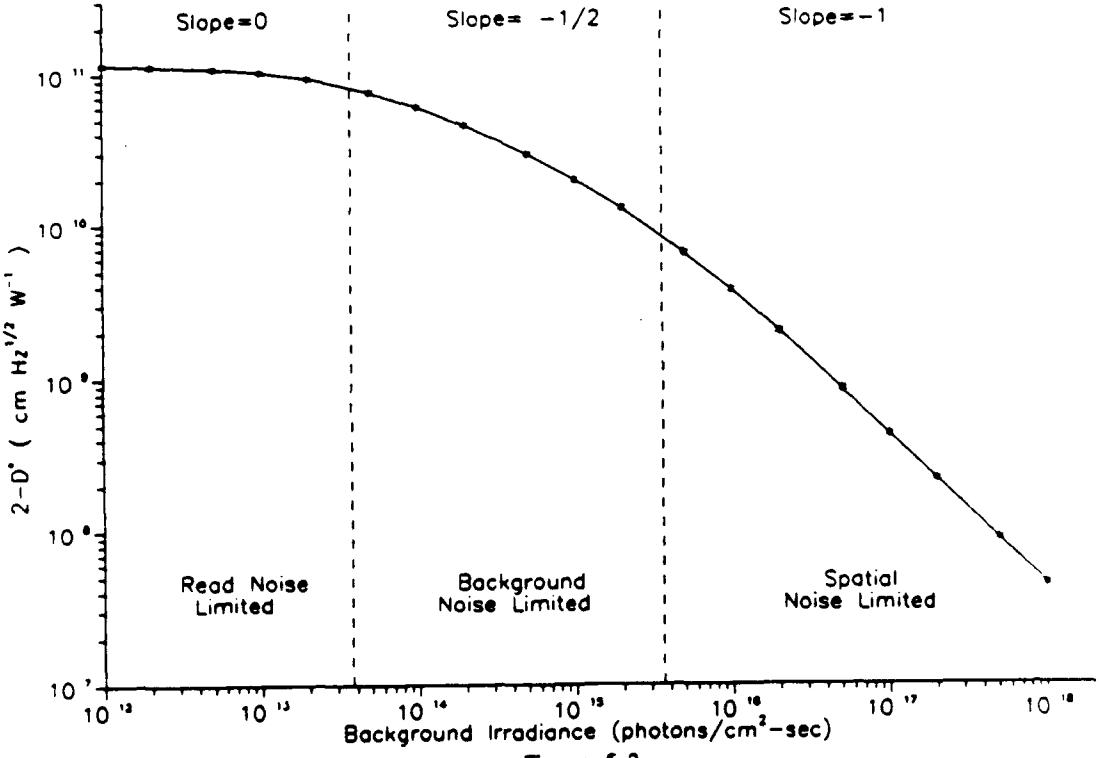

Figure 5.2
2−D* Versus Background Irradiance At 4.5um With 0.1% Nonuniformity

For systems in which the integration time is fixed, the background level at which read noise limited behavior begins is inversely proportional to the quantum efficiency, and directly proportional to square of the read noise. Under this restriction of a fixed integration time, detectors with higher quantum efficiency and lower read noise become read-noise limited at lower background levels. When operating in this region, these detectors also produce the highest signal-to-noise ratio.

If the integration time is a free system variable, then the same signal-to-noise ratio may be obtained by detectors with radically different read noise and quantum efficiency. This is typical of astronomical applications, where time is perhaps only important in relation to the gradual build-up of a dark charge, and in avoiding random cosmic ray events that periodically saturate detector outputs.

The 2-D* expression shows that background noise limited operation may be achieved over a limited range of irradiance levels.

$$\frac{\sigma_R^2}{\eta A t_{int}} < E_p^b < \frac{1}{U^2 \eta A t_{int}} \tag{5.18}$$

$$\frac{E_p^b \text{(upper limit)}}{E_p^b \text{(lower limit)}} = \frac{1}{U^2 \sigma_R^2} \tag{5.19}$$

In this region, the background-limited 2-D* and signal-to-noise ratio are as shown.

$$2\text{-}D^* = \frac{\lambda}{hc}\sqrt{\frac{\eta}{2 E_p^b}} \tag{5.20}$$

$$SNR \approx \frac{\Phi_p^s (\eta\, t_{int})^{\frac{1}{2}}}{\Phi_p^b} \tag{5.21}$$

Equation (5.19) shows that the irradiance range over which background noise limited performance is achieved is determined only by the read noise and the nonuniformity. A reasonable goal for background-noise limited behavior is perhaps three decades in irradiance. Note that an ideal focal plane array would be background noise limited at all irradiance levels.

Equation (5.2) or (5.21) shows that for systems in which the integration time is predetermined, detectors with higher quantum efficiency will produce higher signal-to-noise ratios.

If the system designer is free to choose the integration time, then detectors of vastly different quantum efficiency can achieve identical signal-to-noise ratios. This is typical of terrestrial thermal imaging problems, where the integration time has an upper bound of around 1/30 second, based on television display requirements. In this application, the system designer sets the integration time to prevent saturation of the detector. For detectors of similar charge-handling capability, on a per unit area basis, identical signal-to-noise ratios are obtained.

Above the background noise limited region, the 2-D* relationship shows that spatial noise dominates performance. This operation begins at irradiance levels given by the following expression.

$$E_p^b > \frac{1}{U^2 \eta\, A\, t_{int}} \tag{5.22}$$

The spatial noise limited 2-D* and signal-to-noise ratio further describe operation in this region.

$$2\text{-}D^* \approx \frac{\lambda}{hc\, U\, E_p^b} \sqrt{\frac{1}{2\, A\, t_{int}}} \tag{5.23}$$

$$SNR \approx \frac{\Phi_p^s}{U\, \Phi_p^b} \tag{5.24}$$

Remarkably, in this region, the signal-to-noise ratio is limited only by the nonuniformity of the imaging device.

It might appear that high quantum efficiency detectors enter spatial noise limited operation earlier (at lower E_p^b values) than those of low quantum efficiency. To investigate this idea, it is reasonable to define the integration time in terms of the maximum irradiance expected, and the charge-handling limit of the device.

If E_p^b (max) is the maximum background irradiance expected at the detector, and Q_{max} is the maximum number of electrons per pixel that the device can handle, then the integration time must be set as shown.

$$t_{int} = \frac{Q_{max}}{\eta\, E_p^b(max)\, A} \tag{5.25}$$

By substituting this into Eq. (5.22), the irradiance at the spatial noise limit may be determined.

$$E_p^b > \left[\frac{E_p^b(max)}{U^2\, Q_{max}} \right] \tag{5.26}$$

This result shows that the spatial noise limit is defined only by the uniformity and charge handling capability of the device. Among competing focal plane arrays of similar charge handling capability, the spatial noise limit occurs in inverse proportion to the square of the uniformity. Focal plane arrays with better uniformity are favored.

In summary of these results, the 2-D* relationship illustrates that focal plane arrays may obtain background limited performance only over a limited range. This range is limited to perhaps three or four decades of background irradiance, depending on the read noise and nonuniformity present. The spatial noise limit defines the upper end of the background-limited region. This limit depends on the maximum background irradiance expected at the detector, and on the uniformity and charge handling properties of the imaging device. Surprisingly, the quantum efficiency plays a smaller role than one would expect. In many applications, quantum efficiency differences can be offset by adjustment of the optical integration time.

Throughout this discussion, the topic of nonuniformity compensation has been avoided, in the interest of keeping the mathematical relationships simple. The low nonuniformity values used throughout these arguments, however, are representative of the values achievable under compensation.

As a working measurement of device performance, 2-D* is somewhat cumbersome, requiring that the background irradiance, detector area, and integration time all be reported with the 2-D* value itself. These complications are tied to the fact that D* originally was created for use with continuous current detectors. In these detectors, normalization by the bandwidth affects only the noise; where, in the case of integrating detectors, both the signal and noise are affected by this normalization. In conclusion, 2-D* offers historical continuity, and can be a useful tool in system analysis and design, but is of perhaps limited usefulness in focal plane array characterization.

Derivation of Contrast Signal-to-Noise Ratio

In this section, the derived 2-D* relationship of the previous section will be used to obtain a system figure-of-merit called the Contrast Signal-to-Noise Ratio, or CSNR. The 2-D* expression originally was created with this goal in mind. In this analysis, the CSNR will be shown to be a more general case of an NETD expression commonly used for scanning detection systems.

The starting point for this derivation is the NETD expression given by Lloyd (Lloyd, 1975). There are many such expressions for the NETD. Lloyd's was chosen for its simplicity.

$$NETD = \frac{\pi \sqrt{A\,\Delta f}}{\alpha\beta\, A_o\, \tau_{eff}\, D^*(\lambda_p) \dfrac{\Delta M}{\Delta T}} \tag{5.27}$$

$$\frac{\Delta M}{\Delta T} \equiv \int_{\lambda_1}^{\lambda_2} \frac{\partial M_e^b(\lambda)}{\partial T} \frac{D^*(\lambda)}{D^*(\lambda_p)}\, d\lambda \tag{5.28}$$

Several new terms must be identified. The product ($\alpha\beta\, A_o\, \tau_{eff}$) is the throughput of the optical system. The term $D^*(\lambda_p)$ is the conventional D*, evaluated at the cutoff wavelength of the detector. The radiant spectral exitance of the background is represented by $M_e^b(\lambda)$. The background temperature is T. The optical bandpass of the system is defined by λ_1 and λ_2.

Equation (5.28) may be rewritten for photon units through use of the following.

$$D^*(\lambda) = \left(\frac{\lambda}{\lambda_p}\right) D^*(\lambda_p) \tag{5.29}$$

$$\frac{\partial L_p^b(\lambda)}{\partial T} = \left(\frac{1}{\pi}\right)\left(\frac{\lambda}{hc}\right)\frac{\partial M_e^b(\lambda)}{\partial T} \tag{5.30}$$

Use of these relationships yields the desired result. Note that the integral notation has been dropped in favor of total photon radiance contrast.

$$\frac{\Delta M}{\Delta T} = D^*(\lambda_p)\left(\frac{\pi hc}{\lambda_p}\right)\left(\frac{\partial L_p^b}{\partial T}\right) \tag{5.31}$$

Use of Eq. (5.31) in the NETD expression yields the following equivalent NETD relationship, now in photon units. Note that Δf has been replaced by $1/2\ t_{int}$.

$$NETD = \frac{\left(\frac{A}{2\ t_{int}}\right)^{\frac{1}{2}}}{\left(\alpha\beta\ A_o\ \tau_{eff}\right) D^*(\lambda_p)\left(\frac{hc}{\lambda_p}\right)\left(\frac{\partial L_p^b}{\partial T}\right)} \tag{5.32}$$

This result may be further simplified by noting that the product of the source radiance contrast and the throughput is equivalent to the product of the irradiance contrast at the detector and the detector area.

$$\left(\alpha\beta\ A_o\ \tau_{eff}\right)\frac{\partial L_p^b}{\partial T} = \frac{\partial E_p^b}{\partial T}A \tag{5.33}$$

Making this substitution into Eq. (5.32), and now expressing the reciprocal of the NETD, the following is obtained.

$$NETD^{-1} = \left(\frac{hc}{\lambda_p}\right)\left(D^*(\lambda_p)\right)\left(\frac{\partial E_p^b}{\partial T}\right)(2\, t_{int}\, A)^{\frac{1}{2}} \tag{5.34}$$

Rather than using the D* for a single detector, the 2-D* expression from the previous section will be used. After rearranging terms slightly, the desired result is obtained.

$$NETD^{-1}\left(2\text{-}D^*(\lambda_p)\right) = \frac{\left(\frac{\partial E_p^b}{\partial T}\right)(\eta\, A\, t_{int})}{\left[\, E_p^b\, \eta\, A\, t_{int} + \sigma_R^2 + U^2 \left(E_p^b\, \eta\, A\, t_{int}\right)^2 \,\right]^{\frac{1}{2}}} \tag{5.35}$$

At this point an interesting comparison may be made. In the previous section, the signal-to-noise ratio was defined for a monochromatic test source. This signal-to-noise ratio was given by Eq. (5.13). Comparing it to Eq. (5.35), the new $NETD^{-1}$ expression differs only in the definition of the signal. The NETD is really a noise-to-signal ratio. For thermal imaging, the signal is the differential change in background with respect to temperature, or contrast.

In comparison to a conventional NETD expression, Eq. (5.35) includes the effect of temporal and spatial noise. This is the Contrast Signal-to-Noise ratio.

$$NETD^{-1}\,(2\text{-}D^*) = CSNR \tag{5.36}$$

Note that the CSNR and NETD are reciprocal quantities when the spatial noise is zero.

Making us of Eq. (5.9), the CSNR may be written in terms of N, the average photoresponse.

$$CSNR = \frac{\frac{\partial N}{\partial T}}{\left[N + \sigma_R^2 + U^2 N^2 \right]^{\frac{1}{2}}} \qquad (5.37)$$

This is essentially equal to the CSNR defined by Mooney (Mooney, 1989). Laboratory measurements of the CSNR include all sources of temporal noise, and the post-correction spatial noise. A CSNR curve for the two-point-corrected data of Chapters 3 and 4 is shown in Figure 5.3. The NETD is provided for reference. As one would expect, the NETD and CSNR are in fact equal at the 17°C and 53°C calibration points. The worst deviation in the CSNR from the NETD occurs at around 35°C. This is due to the peak in the two-point-corrected spatial noise curve, last shown in Figure 4.6.

The CSNR is a useful figure-of-merit for infrared imaging systems, showing the extent to which nonuniformity degrades the NETD potential of the camera. This measure of performance may be calculated conveniently from laboratory data. Since it is defined as a signal-to-noise ratio, rather than a noise-to-signal ratio, bigger CSNRs indicate better performance.

In summary, it has been shown that one may define a two-dimensional equivalent to D*. When used in conventional expressions for the NETD, normally applicable to scanning infrared systems, the result includes the effects of spatial noise. This result is the Contrast Signal-to-Noise Ratio , which is a convenient figure-of-merit for focal plane array based systems.

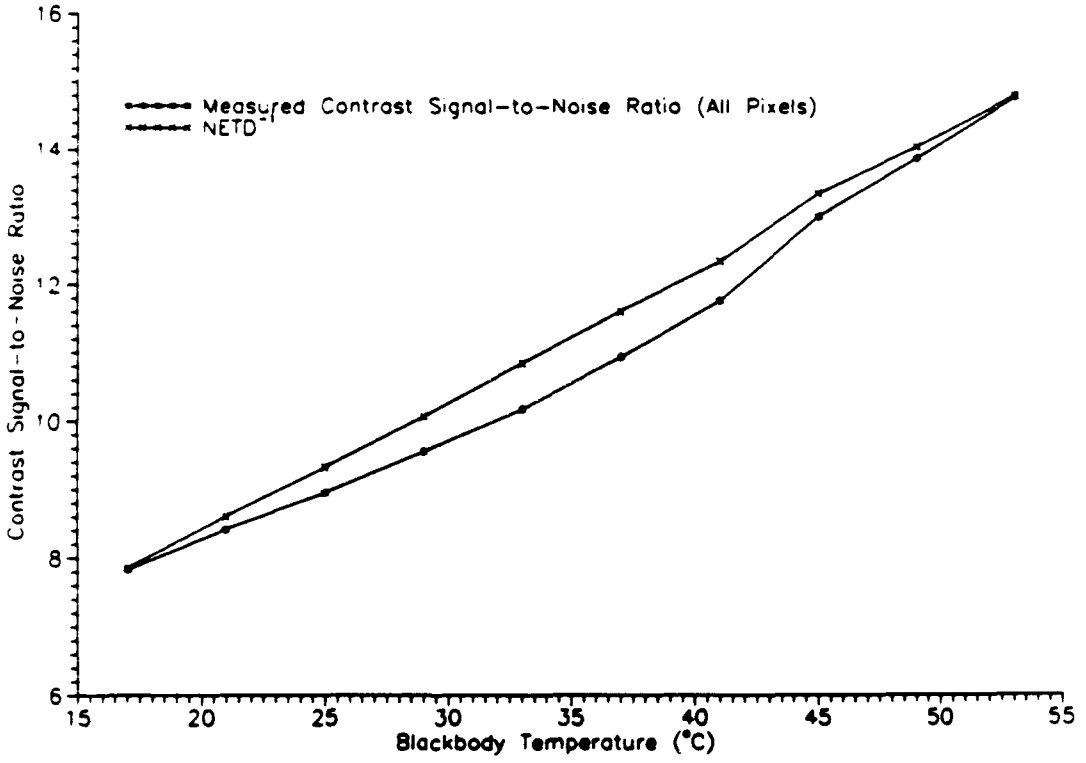

Figure 5.3
Measured Contrast Signal-to-Noise Ratio Under Two-Point Correction and $NETD^{-1}$

CHAPTER 6

CONCLUSIONS AND RECOMMENDATIONS

In this final chapter, the results achieved in this research project will be reviewed. Several specific recommendations are made, and expected future developments are discussed.

Summary of Nonuniformity Research Results

A number of significant results were obtained in this research. In Chapter 2, Mooney's linear theory of nonuniformity was extended to include the specific properties of platinum silicide detectors. In addition to quantifying uncorrected imaging performance, a complete mathematical description of camera operation under one-point and two-point correction was developed.

Following this general, linear analysis of platinum silicide imaging, nonlinear behavior specific to the Hughes CRC-365 device was analyzed. This problem was approached by first considering the detector array and readout separately, and then considering their behavior as a whole.

Nonlinearity in the detector array was shown to be associated with voltage-dependent changes in the quantum efficiency and sense node capacitance. Nonlinearity in the readout is related to its body-effect coefficient. It was shown that nonlinearity in either component makes the problems of nonuniformity compensation more difficult. For representative choices of manufacturing variables, this analysis showed that when considering the imager as a whole, the nonlinear effects of the detector array are dominant.

An actual CRC-365 supplied by Hughes Aircraft and the Rome Laboratory was extensively tested. Both standardized detector tests and detailed nonuniformity tests were conducted.

In general testing of the device, many aspects of imaging performance were measured. It was found that the CRC-365 behaved well, with the exception of anomalous bandwidth, temporal noise and crosstalk effects. Nonuniformity measurements were found to be heavily dependent on device bandwidth. Optimal bias settings were found for the tested device, based on nonuniformity and NETD considerations.

In detailed tests of the nonuniformity, it was discovered that the CRC-365 suffers from periodic spatial noise, which originates in the readout device. This degrades one-point corrected imaging slightly. Under two-point correction, the imager was close to the theoretical limitations imposed by nonlinearity, at least in its odd-numbered outputs. The theoretical limit was not reached due to device bandwidth problems and temporal drift.

Under two-point correction, over a 40°C background temperature range, the odd-numbered outputs displayed a residual spatial noise level that never exceeded 20 percent of the NETD. This is perhaps the largest temperature range over which background-limited performance has been achieved at the sensor level, using a hybrid focal plane array (Shepherd, 1991).

Examining nonuniformity from a more general point of view, a new figure-of-merit called 2-D* was introduced. This figure-of-merit was used to show that nonuniformity and read noise ultimately limit the useful working range of infrared imaging devices. This range covers no more than three or four decades of background irradiance. An accepted system figure-of-merit called the Contrast Signal-to-Noise Ratio was derived using 2-D*.

Expected Future Developments

Nonuniformity problems are among the more troublesome aspects of imaging device design, fabrication, and use. Even though PtSi imaging devices exhibit the best nonuniformity performance offered by any infrared focal plane, there is room for further improvement. It is expected that many of the problem areas identified in this research will be addressed in the near future.

The state-of-the-art in VLSI circuitry is advancing at a phenomenal pace. Among the many research areas in VLSI design is that of sub-micron lithography. As technology evolves to produce smaller integrated feature sizes, the ability to control the larger feature sizes and other processes required for infrared detector arrays and their electronic readout devices also will improve. This will greatly lessen the amount of uncorrected output nonuniformity.

As the ability to fabricate smaller electronic devices progresses, it soon will be possible to add considerably more circuit complexity within unit cells of a given size. This opens the door for curing the de-biasing nonlinearity problem explored in this research.

A longer-range possibility includes integration in the "Z" direction. This technique features stacked layers of active circuitry fabricated on ultrathin insulating films. Work is currently in progress at the Hughes microelectronic facility to perfect this type of process. Using the added circuit density offered by this technique, the possibility of on-focal-plane nonuniformity compensation becomes possible.

An additional payoff of increased circuit density is that more sophisticated data sampling techniques can be introduced to remove some of the 1/f drift and KTC noise before the signal leaves the imaging device.

As shown in this project, even detector arrays that suffer from de-biasing may be adequately corrected over a large temperature range by using simple slope and offset correction. As advances are made in the required external electronics, this type of corrector

will become less expensive, smaller, and will consume less power, making it possible to produce exceptionally compact corrected PtSi cameras.

With advances in computing, higher order, on-line correction schemes will become practical. With even a quadratic correction scheme or piecewise linear approach, corrected nonuniformity would be excellent, provided precision-limiting drift effects can be reduced. Additional research on the effects of 1/f noise on nonuniformity correction is needed.

Some drift is associated with temperature changes at the detector. One future possibility would be to build active temperature control into the device itself. Even simpler, the introduction of a laser-trimmed platinum resistance thermometry device or a blind Schottky diode onto the detector array periphery would greatly simplify the job of temperature control. These devices simply could be wired to unused package leads for connection to an external temperature controller.

Overall, present-day performance in PtSi imaging devices has been shown to be very respectable, and the infrared future appears to be bright.

LIST OF REFERENCES

Aguilera, R., "256 x 256 Hybrid Schottky Focal Plane Arrays," Proc. of SPIE, vol. 782, pp. 108-113 (1987).

Alwardi, M., "Design and Characterization of Integrating Silicon Junction Field-Effect Transistor Amplifiers for Operation in the Temperature Range 40-77 K," Doctoral Dissertation, University of Arizona, Department of Electrical Engineering, 1989.

Beynon, J.E., and Lamb, D.L., *Charge Coupled Devices and Their Applications*, McGraw-Hill Book Co. (UK) Limited, 1980.

Blouke, M., Janesick, J., Elliot, T., Hall, J., Cowens, M., May, P., "Current Status of the 800 x 800 Charge-Coupled-Device Image Sensor," Optical Engineering, vol. 26, no. 9, pp. 864-874 (September 1987).

Britt, P., and Fowler, A., National Optical Astronomy Observatories, Tucson, Arizona, personal communication, 1990.

Cantella, M., "Infrared Focal Plane Array System Performance Modeling," Proc. of SPIE, vol. 327, pp. 40-58 (1982).

Cohen, J., Vilms, J., and Archer, R.J., "Investigation of Semiconductor Schottky Barriers for Optical Detection and Cathodic Emission," Final Report No. AFCRL-68-0651, Contract No. F19628-68-C-0090, Hewlett-Packard Labs., Palo Alto, California 94304, 1968.

Dereniak, E.L., *Optical Radiation Detectors*, John Wiley and Sons, Inc., New York, 1984.

Edwards, J., Gates, J., Alting-Mees, H., Connelly, W., and Thompson, A., "244 x 400 Element Hybrid Platinum Silicide Schottky Focal Plane Array," Proc. of SPIE, vol. 1308, pp. 99-110 (1990).

Fowler, A., Joyce, R., Gatley, I., Gates, J., and Herring, J., "Evaluation of a 256 x 256 PtSi Array for Infrared Ground-Based Astronomy," Proc. of SPIE, vol. 1107, p. 22 (1989).

Frieden, B.R., *Probability, Statistical Optics, and Data Testing*, Springer-Verlag, New York, 1983.

Gates, J., Hughes Aircraft, Carlsbad, CA, personal communication, 1988.

Grum, F., and Becherer, R., *Optical Radiation Measurements, Volume 1, Radiometry*, Academic Press, Inc., Orlando, 1979.

Jones, R.C., "Phenomenological Description of Response and Detecting Ability of Radiation Detectors," Proc. IRE, vol. 47, no. 9, p. 1495 (Sept. 1959).

LIST OF REFERENCES -- *continued*

Kittel, C., *Introduction to Solid State Physics*, 2nd Edition, John Wiley and Sons, Inc., New York, 1960.

Kosonocky, W.F., "Review of Schottky-Barrier Imager Technology," Proc. of SPIE, vol. 1308, pp. 2-26 (1990).

Lloyd, J.M., *Thermal Imaging Systems*, Plenum Press, New York, 1975.

Macleod, H.A., *Thin Film Optical Filters*, Adam Hilger, London, and MacMillan, New York, 1986.

Millman, J., and Halkias, C.C., *Integrated Electronics: Analog and Digital Circuits and Systems*, McGraw-Hill Book Co., New York, 1972.

Mooney, J.M., "Measurement and Modeling of MRTs in IR Staring Sensors," to be published, Proc. of SPIE, vol. 1540, July 1991.

Mooney, J.M., Shepherd, F.D., Ewing, J.E., Murguia, E., and Silverman, J.E., "Responsivity Nonuniformity Limited Performance of Infrared Staring Cameras," Optical Engineering, vol. 28, no. 11, pp. 1151-1161 (November 1989a).

Mooney, J.M., "The dependence of the Schottky emission coefficient on reverse bias," J. Appl. Phys. **65** (7), 1 April 1989b.

Mooney, J.M., Silverman, J., and Weeks, M., "PtSi Internal Photoemission: Theory and Experiment," Proc. of SPIE, vol. 782, pp. 99-107 (1987).

Mooney, J.M., "A comparison of the performance limit of Schottky barrier and standard infrared focal plane arrays," Proc. of SPIE, vol. 570, pp. 157-162 (1985).

Mortara, L., and Fowler, A., "Evaluations of Charge-Coupled Device (CCD) Performance for Astronomical Use," Proc. of SPIE, vol. 290, pp. 28-33 (1981).

Orias, G., Hoffman, A.W., and Casselman, M.F., "58 x 62 InSb focal plane array for infrared astronomy," Proc. of SPIE, vol. 627, pp. 408-417 (1986).

Pierret, R.F., *Modular Series on Solid State Devices Volume IV--Field Effect Devices*, Addison-Wesley Publishing Co., Inc., Reading, Mass., 1983.

Roden, M.S., *The Student Edition of MICRO-CAP II*, Release 5.0, Addison-Wesley Publishing Co., Inc., Reading, Mass., 1989.

Salcido, M.M., Rockwell International Science Center, personal communication, 1991.

Sato, D.L., Terre, W.A., Ewing, W.S., and Gates, J.L., "High Performances PtSi MWIR Camera," Proc. of SPIE, vol. 1308, pp. 145-156 (1990).

LIST OF REFERENCES -- *continued*

Scribner, D.A., Kruer, M.R., Sarkady, K., and Gridley, J.C., "Spatial Noise in Staring IR Focal Plane Arrays," Proc. of SPIE, vol. 930, pp. 56-63 (1988).

Shepherd, F.D., "Silicide Infrared Staring Cameras," Proc. of SPIE, vol. 930, pp. 2-10 (1988).

Shepherd, F.D., Pellegrini, P.W., Ludington, C.E., and Weeks, M.M., "Self-Guarding Schottky Barrier Infrared Detector Array," U.S. Patent #4,531,055 (1985).

Shepherd, F.D., Rome Laboratory, Hanscom AFB, Mass., personal communication, 1991.

Silverman, J., Pelligrini, P., Comer, J., Golvbovic, A., Weeks, M., Mooney, J., and Fitzgerald, J., "Characterization of thin PtSi/p-Si Schottky diodes," Mat. Res. Soc. Symp. Proc., vol. 54 (1986).

Streetman, B.G., *Solid State Electronic Devices*, 2nd Edition, Prentice Hall, Inc., Englewood Cliffs, New Jersey, 1980.

Sze, S.M., *Physics of Semiconductor Devices*, 2nd Edition, Wiley Interscience Publications, New York, 1981.

Vickers, V.E., "Model of Schottky Barrier Hot-Electron-Mode Photodetection," Applied Optics **10**, p. 2190 (1971).

•U.S. GOVERNMENT PRINTING OFFICE: 1992-612-093-60073